SPbGASU
1832

ARCHITECTURE & ENGINEERING

Volume 6
Issue 2
June, 2021

By Architects. For Architects.
By Engineers. For Engineers.

Architecture
Civil and Structural Engineering
Mechanics of Materials
Building and Construction
Urban Planning and Development
Transportation Issues in Construction
Geotechnical Engineering and Engineering Geology
Designing, Operation and Service
of Construction Site Engines

eISSN: 2500-0055
http://aej.spbgasu.ru/

Architecture and Engineering

Volume 6 Issue 2 (2021)

ISSN: 2500-0055

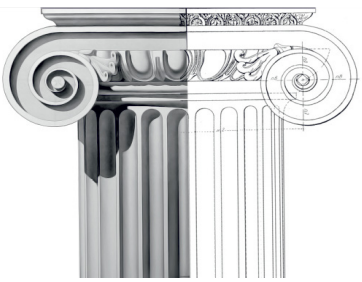

CONTENTS

Architecture and Engineering
peer-reviewed scientific journal
Start date: 2016/03
4 issues per year

Founder, Publisher:
Saint Petersburg State University of Architecture and Civil Engineering

Indexing:
Scopus, EBSCO, Russian Science Citation Index, Directory of Open Access Journals (DOAJ), Google Scholar, Index Copernicus, Ulrich's Periodicals Directory, WorldCat, Bielefeld Academic Search Engine (BASE), Library of University of Cambridge and CyberLeninka.

Corresponding address:
4 Vtoraya Krasnoarmejskaja Str.,
St. Petersburg, 190005, Russia

Website: http://aej.spbgasu.ru/
Phone: +7(812)316-48-49
Email: aejeditorialoffice@gmail.com

Date of issue: 21.06.2021

The Journal was re-registered by the Federal Service for Supervision of Communications, Information Technologies and Mass Communications (Roskomnadzor) on May 31, 2017;
registration certificate of media organization El No. FS77-70026.

DOI: 10.23968/2500-0055-2021-6-2-03-17

EVALUATION OF ENERGY-EFFICIENT RETROFIT POTENTIAL FOR GOVERNMENT OFFICES IN INDIA

Gazal Dandia[1]*, Pratheek Sudhakaran[1], Chaitali Basu[2]

[1]Amity School of Architecture and Planning, Amity University Rajasthan
Jaipur, Rajasthan, India
[2]Department of Building Engineering and Management, School of Planning and Architecture
New Delhi, India

*Corresponding author: ar.gazaldandia@gmail.com

Abstract

Introduction: High energy consumption by buildings is a great threat to the environment and one of the major causes of climate change. With a population of 1.4 billion people and one of the fastest-growing economies in the world, India is extremely vital for the future of global energy markets. The energy demand for construction activities continues to rise and it is responsible for over one-third of global final energy consumption. Currently, buildings in India account for 35% of total energy consumption and the value is growing by 8% annually. Around 11% of total energy consumption are attributed to the commercial sector. Energy-efficient retrofitting of the built environments created in recent decades is a pressing urban challenge. Presently, most energy-efficient retrofit projects focus mainly on the engineering aspects. In this paper, we evaluate various retrofitting options, such as passive architectural interventions, active technological interventions, or a combination of both, to create the optimum result for the selected building. **Methods:** Based on a literature study and case examples, we identified various energy-efficient retrofit measures, and then examined and evaluated those as applied to the case study of Awas Bhawan (Rajasthan Housing Board Headquarters), Jaipur, India. For the evaluation, we developed a simulation model using EQuest for each energy measure and calculated the resultant energy savings. Then, based on the cost of implementation and the cost of energy saved, we calculated the payback period. Finally, an optimum retrofit solution was formulated with account for the payback period and ease of installation. **Results and discussion:** The detailed analysis of various energy-efficient retrofit measures as applied to the case study indicates that the most feasible options for retrofit resulting in optimum energy savings with short payback periods include passive architecture measures and equipment upgrades.

Keywords

Energy efficiency, energy-efficient retrofitting, energy performance evaluation, public buildings in India.

Introduction

Retrofitting or refurbishment is described as work required to upgrade an aged or deteriorated building (Ma et al., 2012). According to USGBC, green retrofit is defined as “any kind of upgrade of an existing building that is wholly or partially occupied to improve its energy efficiency and environmental performance, reduce water use, and improve the comfort and quality of the space in terms of natural light, air quality, and noise, all of which is done in a way that is financially beneficial to the owner”. Amongst other advantages, energy-efficient retrofitting results in reduced energy use, cost savings, and higher worker productivity. According to Benson et al. (2011), the most commonly implemented strategies for energy efficiency include improved heating, ventilation, and cooling systems (HVAC), improved insulation, and lighting.

The gravity of India’s energy crisis is evident from the historic blackouts in July 2012 across the country. Currently, buildings account for 35% of total energy consumption and the value is growing by 8% annually (Bureau of Energy Efficiency, 2021). To address the threat of climate change and energy crisis, apart from focusing on the designs of new buildings, attention must also be paid to existing buildings as they are the major consumers of energy. Even then, their replacement rate by the new-build is only around 1.0–3.0% per annum (Ma et al., 2012). Hence, retrofitting public and private buildings, using more energy-efficient products, technologies, and systems, is considered a viable and cost-effective option to reduce energy consumption and environmental degradation. According to the 2016 PIB report, the commercial sector has the potential to achieve 30% energy savings through technology retrofits.

The government also consumes a major portion of

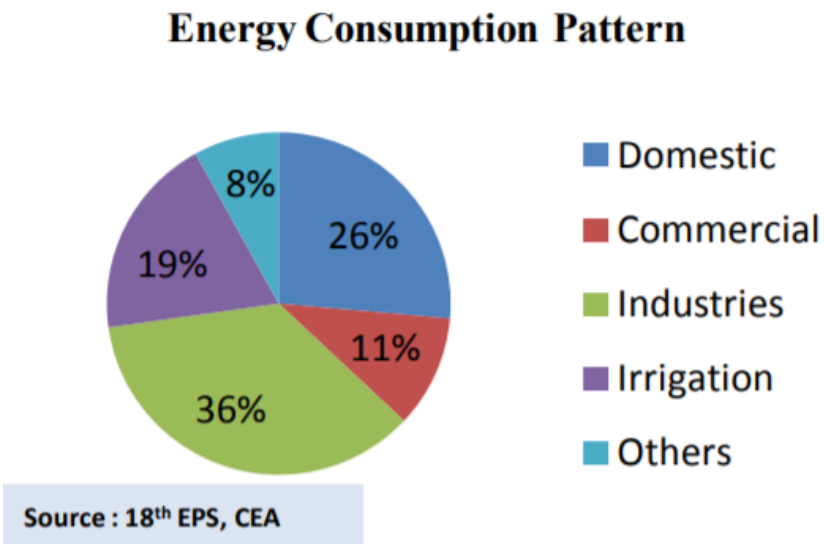

Figure 1. Sector-wise energy consumption pattern in India

energy through its offices, hospitals, railway stations, and other public infrastructure, which have enormous energy-saving potential from proper retrofitting. As can be seen in Fig. 1, commercial buildings account for around 36% of energy consumption in India. Keeping this in mind, BEE (Bureau of Energy Efficiency, Ministry of Power, Government of India) is promoting the implementation of energy efficiency measures in existing buildings through Energy Service Companies (ESCOs), which provide an innovative business model through which the energy-saving potential in an existing building can be captured and the risk faced by the building owner can also be addressed (PIB, 2016). To conserve power, EESL has launched several projects across the country under the BEERP (Buildings Energy Efficiency Retrofit Program). EESL and CPWD have agreed to work on three buildings, namely IP Bhawan, Nirman Bhawan, and Niti Aayog in New Delhi, apart from many other projects across the nation (Energy Division, NITI Aayog, 2015).

Nowadays, there is a great number of building retrofit technologies that are readily available in the market. However, the decision as to which retrofit technology (or measure) should be used for a particular project is a multi-objective optimization problem subject to many constraints and limitations, such as specific building characteristics, total budget available, project target, building services types and efficiency, building fabric, etc. (Ma et al., 2012). The optimal solution is a trade-off among a range of energy-related and non-energy-related factors. A list of possible retrofit options was developed based on a literature study (Dubois et al., 2015; Olander and Siggelsten, 2012; Rey, 2004; Santamouris and Dascalaki, 2002; Upadhyaya et al., 2018), which included both passive and active measures. A detailed analysis of literature (Dascalaki and Santamouris, 2002; Hillebrand et al., 2014; Roper and Pope, 2014; TERI, 2013) and case studies (Abdullah, 2016; NRDC, 2013) helped in developing the methodology for the energy-efficient retrofit study. Each of the retrofit options selected to be implemented in the chosen case study was thoroughly analyzed (Ander, 2016; India Insulation Forum, 2015; Inogate, 2015; Kudarihal and Gupta, 2015; Lunn, 2015; Sudhakaran et al., 2020; TERI, 2021; Walker, 2016). A number of studies were undertaken in the field of energy-efficient retrofit. As per Griego et al. (2015), the use of energy-efficient office equipment and lighting technology and controls can result in over 49% annual energy savings. A case study of Aste and Del Pero (2013) indicated primary energy savings of 40% by improvement of building envelope only, without intervention on HVAC plants, lights or other technical systems. According to Fiaschi et al. (2012), annual energy savings of 4.5% are guaranteed by the installation of PV modules.

To create an efficient scope for retrofit, the unique usage patterns and upgrade opportunities of a project must be examined and evaluated in detail. Energy-efficient design strategies include load reduction, effective use of ambient energy sources, use of efficient equipment and effective control strategies. An integrated design approach is needed to achieve the effective functioning of architectural elements and engineering systems with one another. However, presently, most of the energy-efficient retrofit projects focus mainly on the engineering aspects.

In this paper, we evaluate various retrofitting options, such as passive architectural interventions, active technological interventions, or a combination of both, to create the optimum result for the selected building.

The paper aims to identify and evaluate potential retrofitting measures, in terms of energy savings and payback period, to create an optimum energy-efficient solution for the government office building in Jaipur, India.

Methodology

As depicted in Fig. 2, to begin our study, we need to gain an understanding of energy-efficient retrofit practices based on a literature study and case examples. The inferences from the analysis are then applied to the chosen case study. Our goal was to study and implement retrofit measures at Rajasthan Housing Board Headquarters (Awas Bhawan) in Jaipur. Firstly, we conducted a pre-retrofit survey in order to better understand various features, architectural and operational characteristics, concerns of occupants, and building usage. During the pre-retrofit survey, three methods were used to develop an understanding of the actual usage pattern of the building: design analysis using the drawings and technical information provided, physical observation at the site, and interviews with occupants. Based on the information collected, a base case was developed using EQuest software for energy simulation. The building was modeled in its current state. Then, a list of various retrofit options, derived from the literature study, was developed and analyzed as applied to the chosen case study. The retrofit options included both demand-side and supply-side measures like material alterations in wall and roof insulation or windows, the addition of such

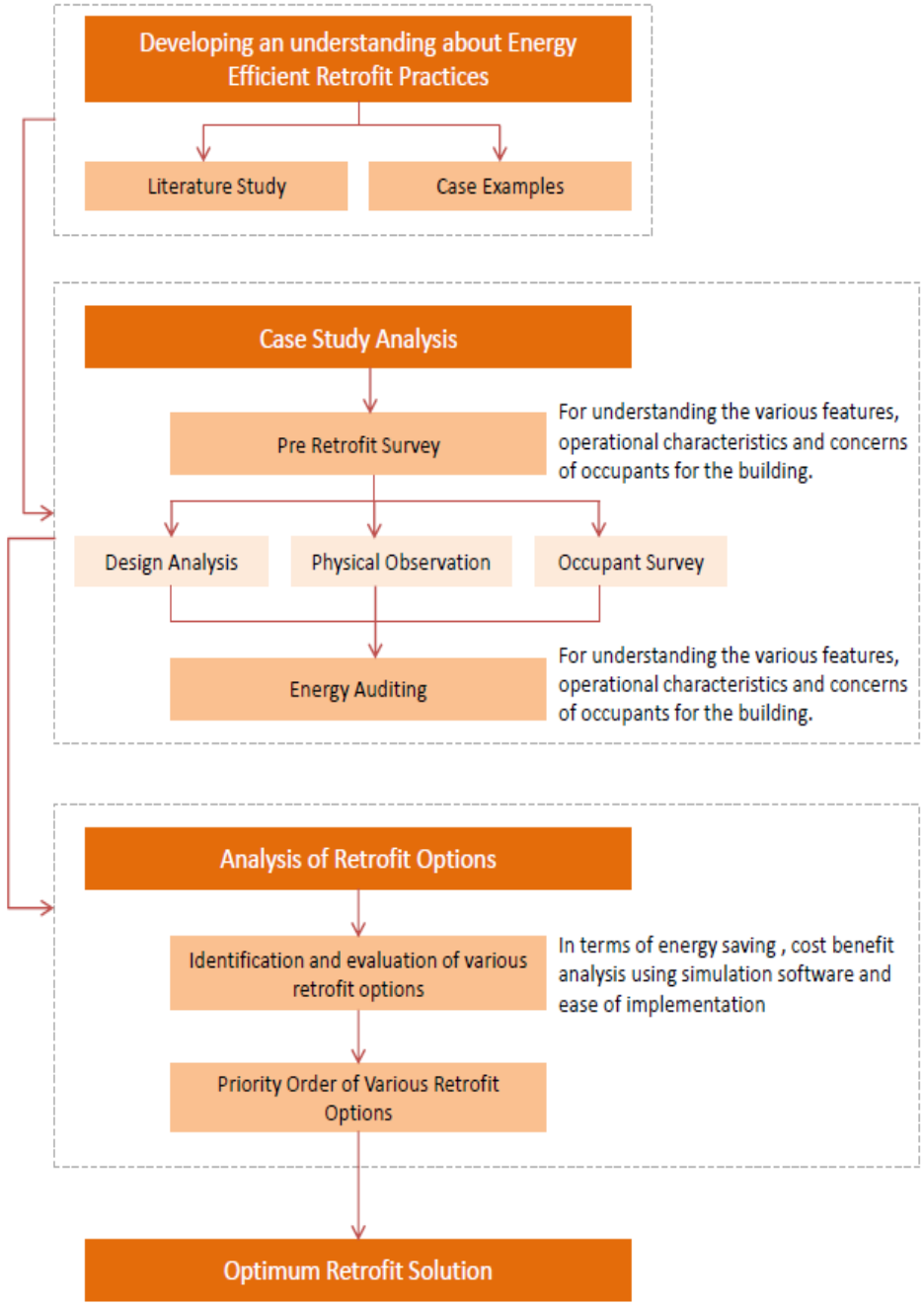

Figure 2. Study methodology

architectural features as sunshades, and equipment upgrade regarding lighting, fans, and solar PVs. All the energy efficiency measures were analyzed in terms of their payback period by comparing the cost of implementation, which was calculated as per a market survey, with the resultant energy savings. Energy savings were determined using the EQuest simulation model for each retrofit option. Based on the payback period and ease of implementation, a priority order was developed for the retrofit options, resulting in the most optimum retrofit solution for the building.

Study and Results

1. Pre-Retrofit Survey

For the analysis, we chose Awas Bhawan (Rajasthan Housing Board Headquarters), Jaipur, Rajasthan, India. The facility has been functional for the last 33 years (since 1984) for 5 days/week, 9 am – 6 pm. It is a four-story structure with an underground basement, an area of 7890 sq. m, and occupancy of around 300 people during working hours. Out of the total area, around 14% are air-conditioned and 65% are centrally air-cooled, thus requiring freshwater.

The average annual energy consumption in the building is 328,250 kWh with the average consumption in summer being 40,000 kWh and in winter — 16,000 kWh. As a result, its Energy Performance Index (EPI) is 42 kWh/sq. m/year.

1.1. Base Case for Energy Simulation

A base model was prepared for "as is" simulation. It has the following characteristics:

1. The building block was made using core and boundary zoning.
2. An evaporative cooling unit of 6750 cfm is provided for each floor, except for the basement and 14% of the area on these floors, which are provided with packaged AC units.
3. The windows are placed with account for the WWR on each face and have sunshades. The windows have the following characteristics: U-Factor — 7.2 W/sq. m·K, SHGC — 0.8, and VLT — 0.76.
4. The walls and the roof have U-factors of 2.01 and 1.376 W/sq. m·K, respectively.
5. The average LPD for the office spaces is 1.1, for the restrooms — 0.9 and for the corridors — 0.5. No dimming devices or sensors are provided with the lighting fixtures.
6. The average equipment power density is 1.25.

Table 1. Base case annual energy consumption

Electric Energy Consumption (kWh)	Jan	Feb	Mar	Apr	May	Jun	Jul	Aug	Sep	Oct	Nov	Dec	Total (kWh)	Consumption,%
Space cooling	3505	5059	11080	15683	20063	20433	17708	18009	16140	13366	8229	4275	153550	14.11%
Ventilation fans	3234	3534	4935	4540	4779	4779	4540	4970	4540	4588	4295	3612	52346	4.81%
Misc. equipment	37869	35735	42441	37936	40917	40714	38139	42441	37936	39393	37665	38140	469326	43.13%
Area lighting	33324	31446	37348	33384	36007	35828	33563	37348	33384	34665	33145	33563	413005	37.95%
Total	77932	75774	95804	91543	101766	101754	93950	102768	92000	92012	83334	79590	1088227	

As per the base case energy simulation results shown in Table 1, the total annual energy consumption in the building is 1,088,227 kWh, where 14.11% are consumed by space cooling, 4.81% — by ventilation fans, 37.95% — by lighting, and 43.13% — by other equipment in the office.

As per the base case simulation, the total electric energy consumption has the following components, as depicted in Fig. 4:

2. Evaluation of Energy Efficiency Measures

2.1. EEM 1 — Wall Insulation

For this case, wall insulation using 50 mm thick XPS (Extruded Polystyrene) boards on the internal face is proposed. The U-Factor for burnt clay brick walls without any insulation is 2.01 W/sq. m·K and the R-Value of XPS insulation is 10.14 BTU. Thus, the resultant U-Factor of the total wall assembly is 0.4303 W/sq. m·K.

As per the energy simulation results shown in Table 2, EEM 1 produces 2.12% energy savings, i.e., 23,027 kWh are saved annually. Better insulation of walls provides energy savings during space cooling and ventilation. The currency used in this paper is the Indian national rupee, denoted as Rs.

The cost calculation for this retrofit measure is as follows:

Area to be insulated = 2204 sq. m. (till the false ceiling) = 23723 sq. ft
Cost of 50 mm XPS insulation = Rs. 50/sq. ft.
Cost for the total area = Rs. 11,86,150
Cost of plaster = Rs. 20/sq. ft
Total cost = 4,74,460
Cost of paint = Rs. 12/sq. ft.
Total cost = 2,84,676

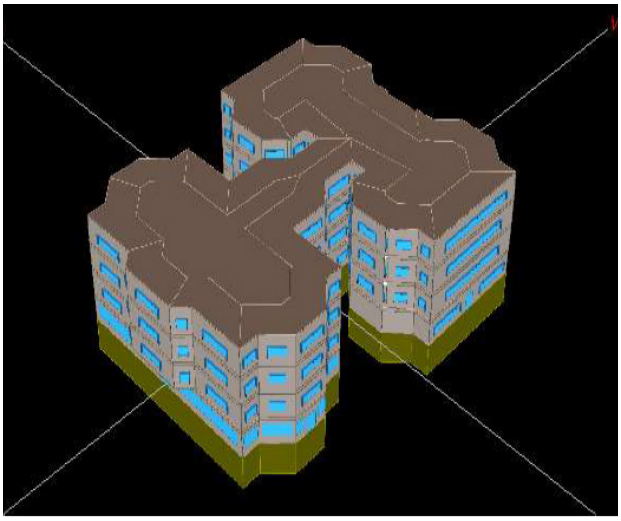

Figure 3. Base case model of Awas Bhawan, Jaipur, India

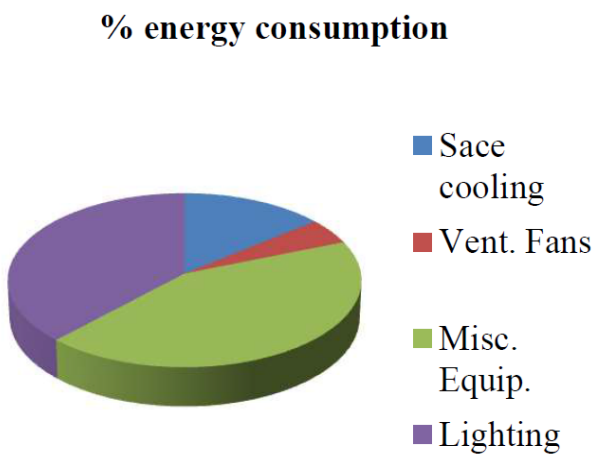

Figure 4. Base case energy consumption breakdown

Table 2. Energy consumption with EEM 1 — 50 mm XPS wall insulation

Electric energy consumption (kWh x 1000)	Jan	Feb	Mar	Apr	May	Jun	Jul	Aug	Sep	Oct	Nov	Dec	Total (kWh x 1000)	Total (kWh)	Savings	Savings, %
Space cooling	3.7	4.9	9.8	13.2	16.4	16.7	14.7	15.3	13.8	11.7	7.5	4.4	132.1	132100	21450	13.97%
Ventilation fans	3.4	3.6	4.7	4.3	4.6	4.6	4.4	4.7	4.3	4.4	4.1	3.7	50.8	50800	1546	2.95%
Misc. equipment	37.9	35.8	42.4	37.9	40.9	40.7	38.1	42.4	37.9	39.4	37.7	38.2	469.3	469300	26	0.01%
Area lighting	33.3	31.5	37.3	33.4	36	35.8	33.6	37.3	33.4	34.7	33.1	33.6	413	413000	5	0%
Total	78.3	75.8	94.2	88.8	97.9	97.8	90.8	99.7	89.4	90.2	82.4	79.9	1065.2	1065200	23027	**2.12%**

Total cost = Rs 19,45,286

Based on Rs. 9/unit cost savings on energy, the payback period for EEM 1 is 9.38 years.

2.2. EEM 2 — Roof Insulation

For this case, roof insulation using 50 mm thick XPS (Extruded Polystyrene) boards is proposed. The U-factor for a normal concrete roof without any insulation is 1.367 W/sq. m·K and the R-Value of XPS insulation is 10.14 BTU. Thus, the resultant U-Factor of the total roof assembly is 0.397 W/sq. m·K.

As per the energy simulation results shown in Table 3, EEM 2 produces 0.39% energy savings, i.e., 4200 kWh are saved annually. Better insulation of the roof provides a very small amount of energy savings during space cooling and ventilation (mainly just in the air-conditioned spaces).

The cost calculation for this retrofit measure is as follows:

Area to be insulated = 5930 sq. ft
Cost of 50 mm XPS insulation = Rs. 50/sq. ft.
Cost for the total area = Rs. 296,500
Cost of roofing = Rs. 60/sq. ft.
(75–100 mm thickness)
Total = Rs. 355,800
Total cost = Rs. 652,300

As per the energy simulation results, the cost of energy saved per year is Rs. 37,800. Thus, the payback period for this retrofit measure is 17.26 years.

2.3. EEM 3.1 — Tinted SGUs in Windows

In this case, windows on all the facades are replaced with normal aluminum frame windows with tinted single glass units (SGUs). Such windows have the following characteristics: U-Factor — 6.7 W/sq. m·K, SHGC — 0.6, and VLT — 0.6.

As per the energy simulation results shown in Table 4, EEM 3.1 produces 0.39% energy savings, i.e., 4100 kWh are saved annually. This results in cost savings of Rs. 36,000 per year. The tinted glass panes reduce heat gain, especially due to direct sunlight.

The cost of replacing all the windows with a total area of 7476 sq. ft at Rs. 350/sq. ft will be Rs. 2,616,600.

Therefore, its payback period is 72.68 years.

Table 3. Energy consumption with EEM 2 — 50 mm XPS roof insulation

Electric energy consumption (kWh x 1000)	Jan	Feb	Mar	Apr	May	Jun	Jul	Aug	Sep	Oct	Nov	Dec	Total (kWh x 1000)	Total (kWh)	Savings	Savings, %
Space cooling	4.2	5	9.3	12.2	15.4	15.8	14.4	15	13.3	11.2	7.3	4.8	127.9	127900	4200	3.18%
Ventilation fans	3.4	3.6	4.7	4.3	4.6	4.6	4.4	4.7	4.3	4.4	4.1	3.7	50.8	50800	0	0%
Misc. equipment	37.9	35.8	42.4	37.9	40.9	40.7	38.1	42.4	37.9	39.4	37.7	38.2	469.3	469300	0	0%
Area lighting	33.3	31.5	37.3	33.4	36	35.8	33.6	37.3	33.4	34.7	33.1	33.6	413	413000	0	0%
Total	78.8	75.9	93.7	87.8	96.9	96.9	90.5	99.4	88.9	89.7	82.2	80.3	1061	1061000	4200	**0.39%**

Table 4. Energy consumption with EEM 3.1 — all windows with normal aluminum frame and tinted SGUs

Electric energy consumption (kWh x 1000)	Jan	Feb	Mar	Apr	May	Jun	Jul	Aug	Sep	Oct	Nov	Dec	Total (kWh x 1000)	Total (kWh)	Savings	Savings, %
Space cooling	3.8	4.7	9	11.9	15.1	15.5	14	14.7	13.1	10.9	7	4.5	124.2	124200	3700	2.89%
Ventilation fans	3.6	3.6	4.6	4.2	4.5	4.5	4.3	4.6	4.2	4.3	4.1	3.9	50.4	50400	400	0.79%
Misc. equipment	37.9	35.8	42.4	37.9	40.9	40.7	38.1	42.4	37.9	39.4	37.7	38.2	469.3	469300	0	0%
Area lighting	33.3	31.5	37.3	33.4	36	35.8	33.6	37.3	33.4	34.7	33.1	33.6	413	413000	0	0%
Total	78.6	75.6	93.3	87.4	96.5	96.5	90	99	88.6	89.3	81.9	80.2	1056.9	1056900	4100	**0.39%**

2.4. EEM 3.2 — DGUs in Windows

In this case, all the existing windows are replaced with normal aluminum frame windows with double glazed units (DGUs). The DGU windows have the following characteristics: U-Factor — 4.65 W/sq. m·K, SHGC — 0.4, and VLT — 0.5.

As per the simulation results shown in Table 5, EEM 3.2 produces 1.12% energy savings, i.e., 11,900 kWh per year resulting in cost savings of Rs. 106,200. The double glass units provide insulation against heat gain.

The cost of simple aluminum frame DGU windows is Rs. 420/sq. ft. The area of the windows to be replaced is 7476 sq. ft, which makes the total cost of replacement equal to Rs. 3,139,920.

This results in a payback period of 29.57 years.

2.5. EEM 3.3 — Thermal Break Frames

In this case, all the existing windows are replaced with windows having thermal break aluminum frames and double glazed panels. Such assemblies have the following characteristics: U-factor — 3.34 W/sq. m·K, SHGC — 0.4, and VLT — 0.5.

While performing simulation, as depicted in Table 6, we obtain annual energy savings of 1.23% (13,000 kWh), leading to cost savings of Rs. 116,100 per year. The thermal break in frames provides additional resistance against heat gain.

The cost of thermal break frame DGU windows is Rs. 1250/sq. ft, resulting in a total cost of Rs. 9,345,000 for 7476 sq. ft.

As a result, the payback period will be 80.49 years.

2.6. EEM 4 — Fins

In this case, four horizontal fins are provided, having 300 mm width and 50 mm thickness, on the south-east, south-west and south façade fenestrations (Fig. 5), which do not have enough shading.

The construction of such fins costs Rs. 175 per running meter and the total length of the fins to be constructed is 240 m. This will result in a total cost of Rs. 42,000 in case of this retrofit measure.

The fins save around 0.60% (6500 kWh) energy and, therefore, Rs. 58,500 annually. Thus, the cost of construction can be repaid in 1.39 years by savings.

2.7. EEM 5 — Energy-Efficient Lighting Fixtures

In this case, all the existing lighting fixtures (mostly tube lights) are to be replaced with energy-efficient lighting, i.e., LEDs. The use of LEDs results in 25% energy savings for lighting, therefore, the LPD

Table 5. Energy consumption with EEM 3.2 — all windows with normal aluminum frame and DGUs

Electric energy consumption (kWh x 1000)	Jan	Feb	Mar	Apr	May	Jun	Jul	Aug	Sep	Oct	Nov	Dec	Total (kWh x 1000)	Total (kWh)	Savings	Savings, %
Space cooling	3.7	4.5	8.4	11.1	14.2	14.6	13.2	13.9	12.3	10.3	6.6	4.3	117.1	117100	10800	8.44%
Ventilation fans	3.5	3.6	4.6	4.2	4.4	4.4	4.2	4.6	4.2	4.2	4	3.8	49.7	49700	1100	2.17%
Misc. equipment	37.9	35.8	42.4	37.9	40.9	40.7	38.1	42.4	37.9	39.4	37.7	38.2	469.3	469300	0	0%
Area lighting	33.3	31.5	37.3	33.4	36	35.8	33.6	37.3	33.4	34.7	33.1	33.6	413	413000	0	0%
Total	78.4	75.4	92.7	86.6	95.5	95.5	89.1	98.2	87.8	88.6	81.4	79.9	1049.1	1049100	11900	**1.12%**

Table 6. Energy consumption with EEM 3.3 — all windows with thermal break aluminum frames and DGUs

Electric energy consumption (kWh x 1000)	Jan	Feb	Mar	Apr	May	Jun	Jul	Aug	Sep	Oct	Nov	Dec	Total (kWh x 1000)	Total (kWh)	Savings	Savings, %
Space cooling	3.8	4.5	8.4	11	13.9	14.3	12.8	13.6	12.2	10.3	6.7	4.5	116	116000	11900	9.30%
Ventilation fans	3.6	3.6	4.6	4.2	4.4	4.4	4.2	4.5	4.2	4.2	4	3.8	49.7	49700	1100	2.17%
Misc. equipment	37.9	35.8	42.4	37.9	40.9	40.7	38.1	42.4	37.9	39.4	37.7	38.2	469.3	469300	0	0.00%
Area lighting	33.3	31.5	37.3	33.4	36	35.8	33.6	37.3	33.4	34.7	33.1	33.6	413	413000	0	0.00%
Total	78.6	75.4	92.7	86.5	95.2	95.2	88.7	97.8	87.7	88.6	81.5	80.1	1048	1048000	13000	**1.23%**

Table 7. Energy consumption with EEM 5 — energy-efficient lighting fixtures

Electric energy consumption (kWh x 1000)	Jan	Feb	Mar	Apr	May	Jun	Jul	Aug	Sep	Oct	Nov	Dec	Total (kWh x 1000)	Total (kWh)	Savings	Savings, %
Space cooling	3.35	4.12	7.8	10.38	13.45	13.83	12.53	13.2	11.71	9.68	6.13	3.97	110.15	110150	5850	5.04%
Ventilation fans	3.4	3.47	4.55	4.17	4.39	4.39	4.17	4.55	4.16	4.21	4	3.73	49.19	49190	510	1.03%
Misc. equipment	37.9	35.8	42.4	37.9	40.9	40.7	38.1	42.4	37.9	39.4	37.7	38.2	469.3	469300	0	0%
Area lighting	24.84	23.44	27.84	24.89	26.84	26.71	25.03	27.85	24.89	25.84	24.71	25.02	307.9	307900	105100	25.45%
Total	69.49	66.83	82.59	77.34	85.58	85.63	79.83	88	78.66	79.13	72.54	70.92	936.54	936540	111460	**10.64%**

for the office spaces becomes equal 0.825, for the restrooms — 0.675 and for the corridors — 0.375.

This modification produces energy savings of 10.64% (111,460 kWh) per year, as depicted in Table 7, resulting in cost savings of Rs. 1,003,140. Apart from savings in terms of direct energy consumption, energy-efficient lighting also provides some savings for cooling and ventilation, as energy-efficient lights dissipate less heat into the environment.

The fixture requirements are determined using

$$N\,(\text{lum}) = E\,(\text{avg}) \times \text{Area} / u \times d \times \alpha$$

where: u = 0.8; d=0.7. α = 100 lux (corridors)
= 300 lux (offices)
= 500 lux (open spaces).

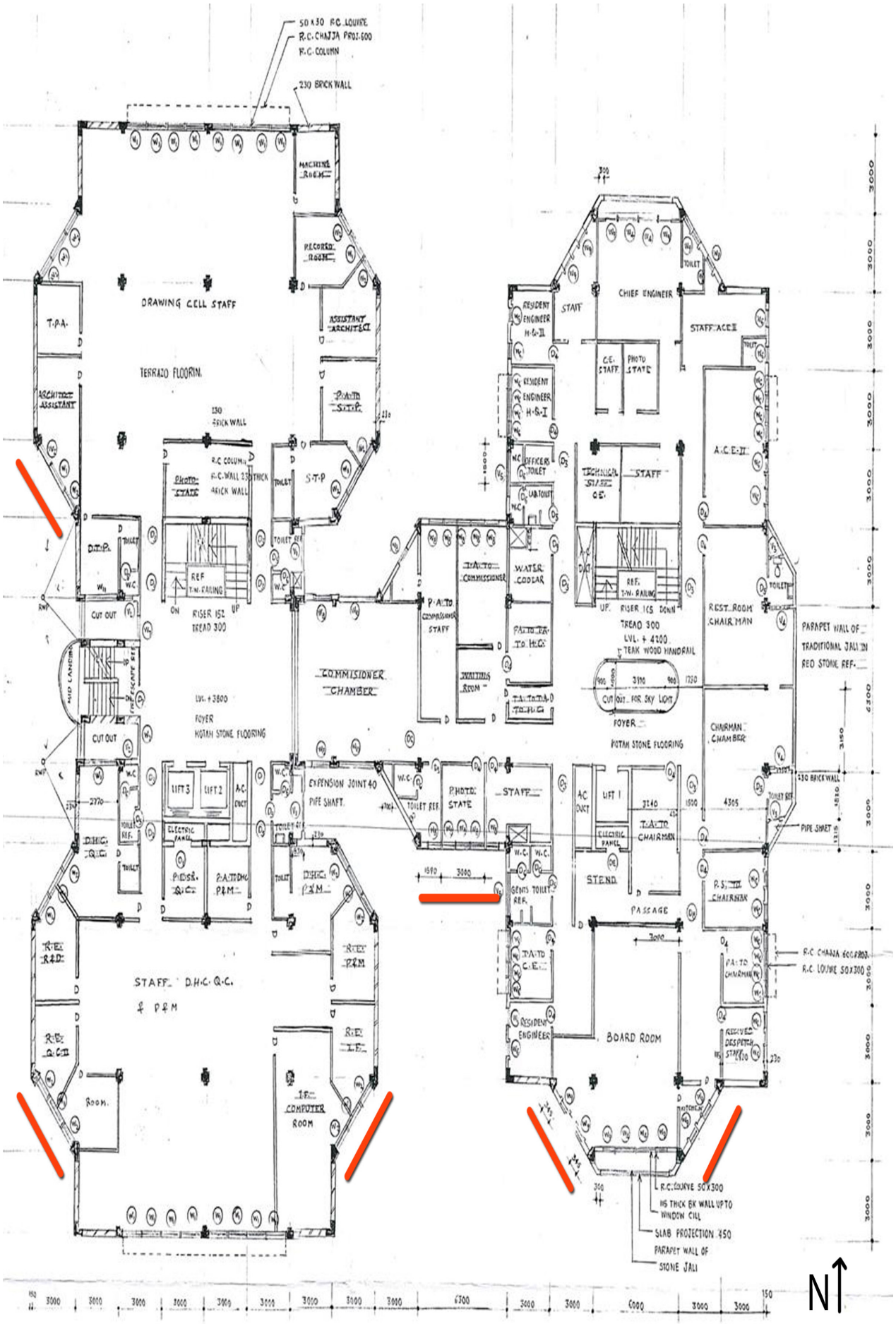
50 x 30 RC LOUVRE
R.C. CHAJJA PROJ. 600
R.C. COLUMN
230 BRICK WALL
DRAWING CELL STAFF
TERRAZO FLOORIN.
T.P.A.
ARCHITECT ASSISTANT
ASSISTANT ARCHITECT
RECORD ROOM
MACHINE ROOM
130 BRICK WALL
R.C. COLUMN
R.C. WALL 230 THICK
BRICK WALL
PHOTO STATE
S.T.P.
D.M.P.
TOILET
W.C.
CUT OUT
REF T.W. RAILING
RISER 152
TREAD 300
UP
DN
MID LANDING
FIRE ESCAPE REF.
LVL. +3800
FOYER
KOTAH STONE FLOORING
COMMISIONER CHAMBER
P.A. TO COMMISSIONER
STAFF
WATER COOLER
WAITING ROOM
P.A. TO TEA TO H.C.S.
RESIDENT ENGINEER H.S.-II
RESIDENT ENGINEER H.S.-I
OFFICERS TOILET
LAB TOILET
CHIEF ENGINEER
STAFF ACE II
C.E. STAFF
PHOTO STATE
TECHNICAL STAFF O.E.
A.C.E.-II
REST ROOM CHAIRMAN
RISER 165 DOWN
TREAD 300
LVL. + 4200
TEAK WOOD HANDRAIL
CUT OUT FOR SKY LIGHT
FOYER
KOTAH STONE FLOORING
CHAIRMAN CHAMBER
PARAPET WALL OF TRADITIONAL JALI IN RED STONE REF.
230 BRICK WALL
PIPE SHAFT
LIFT 3
LIFT 2
A.C. DUCT
ELECTRIC PANEL
EXPENSION JOINT 40
PIPE SHAFT
PHOTO STATE
STAFF
LIFT 1
T.A. TO CHAIRMAN
STENO.
PASSAGE
GENTS TOILET REF.
R.S.T.M. CHAIRMAN
R.C. CHAJJA 600 PROJ.
R.C. LOUVRE 50 X 300
STAFF D.H.C. Q.C. & P&M
R.E. R&D
R.E. P&M
R.E. Q.C.II
R.E. I.E.
Room.
I.E. COMPUTER ROOM
BOARD ROOM
RESIDENT ENGINEER
RECEIVED DESPATCH STAFF
R.C. LOUVRE 50 X 300
115 THICK BK WALL UP TO WINDOW CILL
SLAB PROJECTION 450
PARAPET WALL OF STONE JALI
N

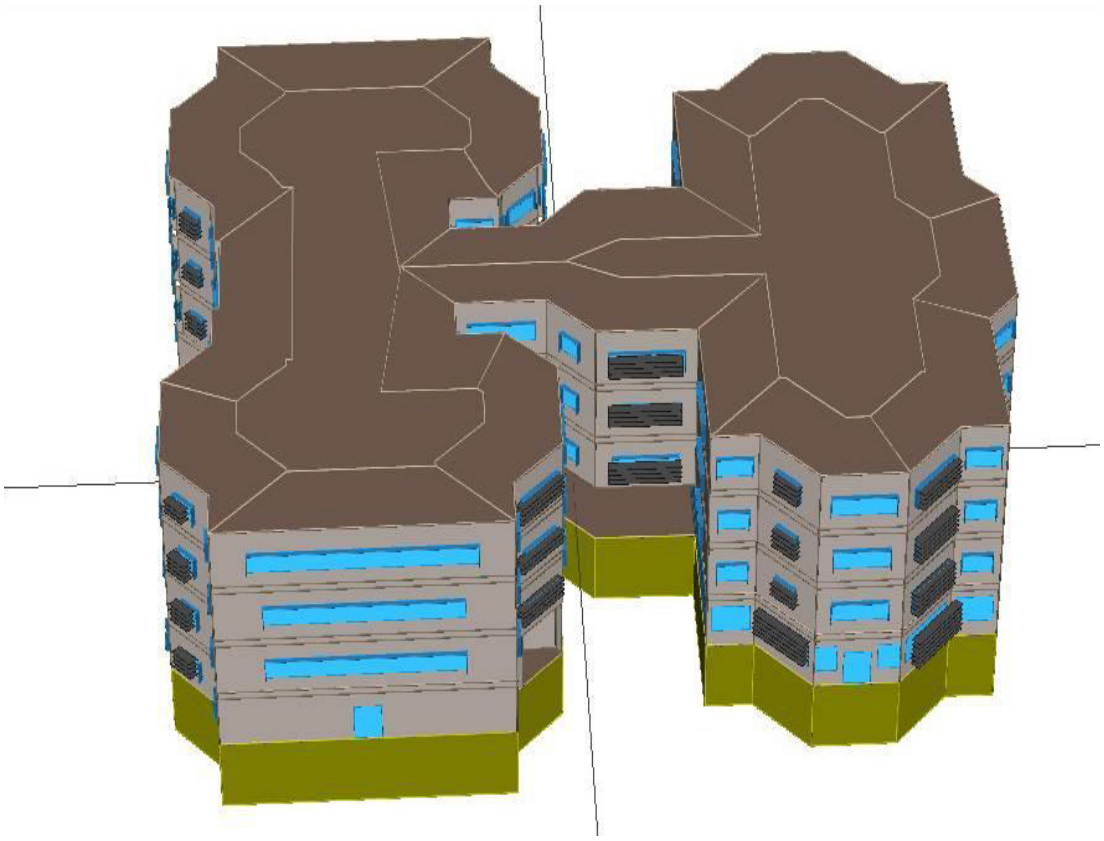

Figure 5. Location of horizontal fins for EEM 4

For cost calculation, 450 pcs. of Philips Sereno (28 W, 3000 lumens) of Rs. 8400 each, 300 pcs. of Power Balance (29.5 W, 3400 lumens) of Rs. 16,000 each and 290 pcs. of Green LED Ultima (10.5 W, 1000 lumens) of Rs. 1500 each are considered. This results in a total cost of Rs. 9,015,000.

Based on these calculations, EEM 5 has a payback period of 8.9 years.

2.8. EEM 6 — Use of Sensors

2.8.1. EEM 6.1 — Use of Daylight Sensors

Generally, the daylit area is 25% of the total area. With the use of daylight sensors, 10% of lighting power consumption can be reduced in those areas. Hence, with daylight sensors, the LPD for the office spaces becomes equal 0.80, for the restrooms — 0.658 and for the corridors — 0.366.

The use of daylight sensors produces total energy savings of 0.85% (8000 kWh), as depicted in Table 8, and cost savings of Rs. 72,000 per year. The reduction in direct energy consumption due to lighting also results in reduced heat load.

2.8.2. EEM 6.2 — Use of Occupancy Sensors

Generally, the area controlled by occupancy

Table 8. Energy consumption with EEM 6.1 — daylight sensors

Electric energy consumption (kWh x 1000)	Jan	Feb	Mar	Apr	May	Jun	Jul	Aug	Sep	Oct	Nov	Dec	Total (kWh x 1000)	Total (kWh)	Savings	Savings, %
Space cooling	3.31	4.08	7.75	10.33	13.42	13.8	12.52	13.16	11.69	9.65	6.09	3.93	109.73	109730	420	0.38%
Ventilation fans	3.37	3.46	4.55	4.17	4.39	4.39	4.17	4.56	4.17	4.21	3.99	3.71	49.14	49140	50	0.10%
Misc. equipment	37.9	35.8	42.4	37.9	40.9	40.7	38.1	42.4	37.9	39.4	37.7	38.2	469.3	469300	0	0%
Area lighting	24.24	22.87	27.16	24.28	26.19	26.05	24.41	27.16	24.28	25.21	24.11	24.41	300.37	300370	7530	2.45%
Total	68.82	66.21	81.86	76.68	84.9	84.94	79.2	87.28	78.04	78.47	71.89	70.25	928.54	928540	8000	**0.85%**

Table 9. Energy consumption with EEM 6.2 — occupancy sensors

Electric energy consumption (kWh x 1000)	Jan	Feb	Mar	Apr	May	Jun	Jul	Aug	Sep	Oct	Nov	Dec	Total (kWh x 1000)	Total (kWh)	Savings	Savings, %
Space cooling	3.24	4.02	7.67	10.25	13.35	13.74	12.44	13.1	11.62	9.57	6.02	3.86	108.88	108880	850	0.77%
Ventilation fans	3.35	3.44	4.54	4.16	4.38	4.38	4.17	4.57	4.16	4.21	3.99	3.69	49.04	49040	100	0.20%
Misc. equipment	37.9	35.8	42.4	37.9	40.9	40.7	38.1	42.4	37.9	39.4	37.7	38.2	469.3	469300	0	0%
Area lighting	23.02	21.73	25.8	23.07	24.88	24.75	23.19	25.8	23.07	23.95	22.9	23.19	285.35	285350	15020	5.00%
Total	67.51	64.99	80.41	75.38	83.51	83.57	77.9	85.87	76.75	77.13	70.61	68.94	912.57	912570	15970	**1.72%**

sensors is 75% of the total area. With the use of occupancy sensors, 10% of lighting power consumption can be reduced in those areas. Hence, with occupancy sensors, the LPD for the office spaces becomes equal 0.763, for the restrooms — 0.624 and for the corridors — 0.347.

The application of occupancy sensors ensures 1.72% (15970 kWh) energy savings, as depicted in Table 9, and Rs. 143,730 cost savings annually. The reduction in lighting load also results in the reduction of heat load thus produced.

The cost of combined daylight and occupancy sensors is Rs. 1500 each. In the building, 325 pcs. of such sensors shall be used, resulting in a total cost of Rs. 487,000.

Based on total energy savings ensured by both

Table 10. Energy consumption with EEM 7 — BEE 5 star rated fans

Electric energy consumption (kWh x 1000)	Jan	Feb	Mar	Apr	May	Jun	Jul	Aug	Sep	Oct	Nov	Dec	Total (kWh x 1000)	Total (kWh)	Savings	Savings, %
Space cooling	2.98	3.79	7.34	9.91	13.08	13.48	12.22	12.83	11.35	9.25	5.73	3.59	105.55	105550	3330	3.06%
Ventilation fans	3.23	3.36	4.52	4.15	4.37	4.37	4.15	4.55	4.15	4.22	3.96	3.59	48.62	48620	420	0.86%
Misc. equipment	33.17	31.3	37.18	33.23	35.84	35.67	33.42	37.18	33.23	34.51	32.99	33.41	411.13	411130	58170	12.40%
Area lighting	23.02	21.73	25.8	23.07	24.88	24.75	23.19	25.8	23.07	23.95	22.9	23.19	285.35	285350	0	0%
Total	62.4	60.18	74.84	70.36	78.17	78.27	72.98	80.36	71.8	71.93	65.58	63.78	850.65	850650	61920	**6.79%**

Table 11. Energy consumption with EEM 8 — VFD in the central evaporative cooler

Electric energy consumption (kWh x 1000)	Jan	Feb	Mar	Apr	May	Jun	Jul	Aug	Sep	Oct	Nov	Dec	Total (kWh x 1000)	Total (kWh)	Savings	Savings, %
Space cooling	2.98	3.69	7.24	9.81	12.98	13.48	12.2	12.83	11.35	9.15	5.73	3.59	105.03	105030	520	0.49%
Ventilation fans	1.93	1.96	2.52	2.35	2.37	2.37	2.35	2.45	2.35	2.3	2.16	2.09	27.2	27200	21420	44.06%
Misc. equipment	33.17	31.3	37.18	33.23	35.84	35.67	33.41	37.18	33.23	34.51	32.99	33.41	411.12	411120	10	0%
Area lighting	23.02	21.73	25.8	23.07	24.88	24.75	23.19	25.8	23.07	23.95	22.9	23.19	285.35	285350	0	0%
Total	61.1	58.68	72.74	68.46	76.07	76.27	71.15	78.26	70	69.91	63.78	62.28	828.7	828700	21950	**2.58%**

daylight and occupancy sensors, the cost of their application can be repaid in 2.26 years.

2.9. EEM 7 — Energy-Efficient Fans

In this case, all the existing fans are replaced with BEE 5 star rated fans. Normal fans operate at 75 W, 0.3 kWh whereas 5 star rated fans operate at 50 W, 0.2 kWh.

This results in annual energy savings of 6.79%, i.e., 61,920 kWh, as depicted in Table 10. Such energy savings reduce the electricity costs by Rs. 557,280.

Each BEE 5 star rated fan costs Rs. 2000, therefore, to install 130 such fans, Rs. 260,000 will be required.

Based on the above calculations, the payback period for energy-efficient fans will be 0.47 years.

2.10. EEM 8 — Variable Frequency Drive

In this case, a variable frequency drive (VFD) is used in the central evaporative cooler. A constant speed drive operates only at 100% load, whereas a VFD can operate at variable speed in case of different power loads, thereby reducing power consumption according to the needs.

The VFD use leads to energy savings of 2.58% (21,950 kWh) per year as shown in Table 11, resulting in a reduction of energy costs by Rs. 197,550.

The VFD cost for nine fans of 3000 cfm, 9 kW is Rs. 60,000. Thus, the initial cost can be repaid in 0.30 years by the savings produced.

2.11. EEM 9 — Solar PVs

In this case, a 50 kW Solar PV system has to be installed for supply-side management. A 50 kW system will require a 500 sq. m area (total roof area — 1500 sq. m) and will generate 66,000 units per year, resulting in cost savings of Rs. 59,400.

The initial installation cost of the system will be Rs. 6,800,000 and the initial maintenance cost will be Rs. 272,000 with an increment of Rs. 13,600/year. Thus, its payback period will be around 11.45 years.

3. Comparative Analysis

To evaluate the different EEMs, we offer a matrix (Table 12), based on which the EEMs are prioritized according to the payback period and ease of installation, where the score of 10 is the most difficult and the score of 1 is the easiest.

The results from the comparative matrix (Table 12) are presented in Fig. 6.

Table 12. Comparative matrix

	EEM	Energy Saved (kWh)	Initial Cost (Rs.)	Annual Savings (Rs.)	Payback Period (yrs)	Ease of Installation	Priority
1	Wall insulation	23,027	1,944,630	207,243	9.38	7	II
2	Roof insulation	4200	652,300	37,800	17.26	7	III
3.1	Normal Al frame windows with tinted SGUs	4100	2,616,600	36,000	72.68	8	-
3.2	Normal Al frame windows with DGUs	11,900	3,139,920	106,200	29.57	8	III
3.3	Windows having Al frames with thermal breaks and DGUs	13,000	9,345,000	116,100	80.49	8	-
4	Additional shading devices	6500	42,000	58,500	1.39	5	I
5	Energy-efficient lighting fixtures	111,460	9,015,000	1,003,140	8.99	3	II
6.1	Daylight sensors	8000	487,000	72,000	2.26	3	I
6.2	Occupancy sensors	15,970		143,730			
7	BEE 5 star rated fans	61,920	260,000	557,280	0.47	2	I
8	VFD in central evaporative coolers	21,950	60,000	197,550	0.30	3	I
9	Solar panels	66,000	6,800,000	594,000	11.45	2	II

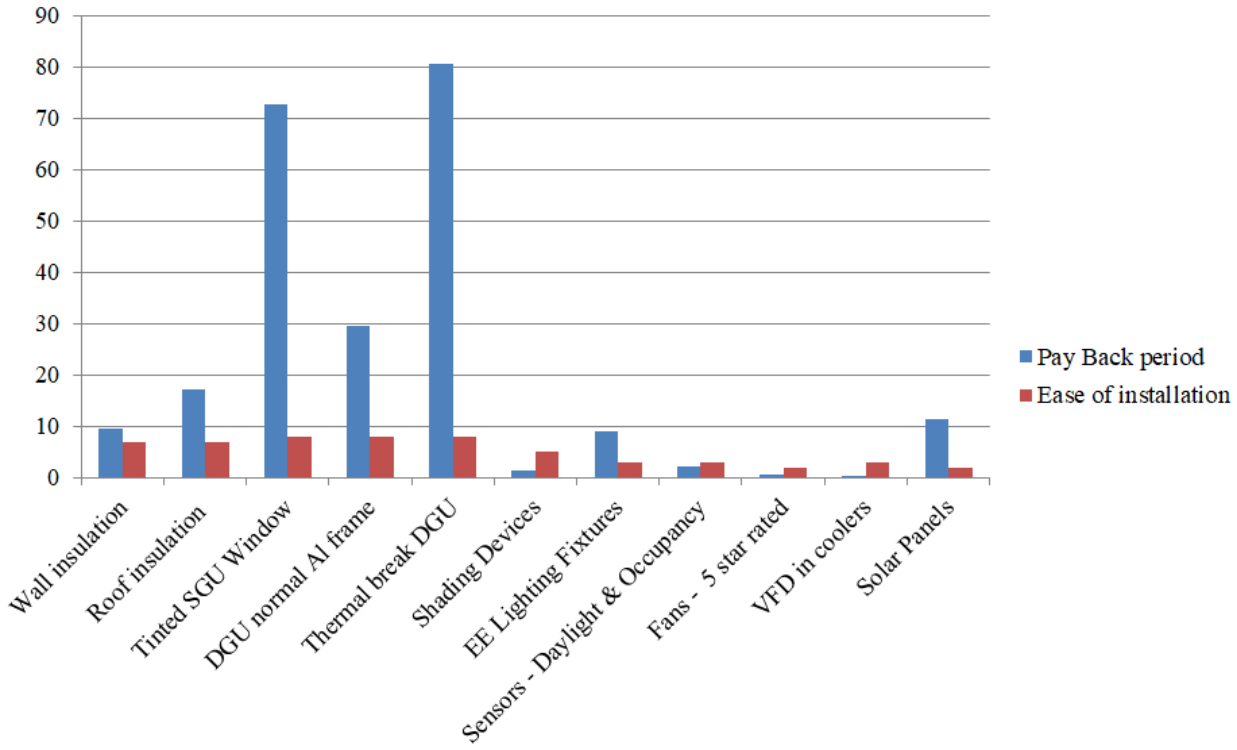

Figure 6. Comparative graph

4. Optimum Retrofit Solution

Using the ESCO route, with 70% given to the ESCO for repayment, the optimum retrofit plan is as shown in Table 13.

Repayment will only be through 70% of cost savings, i.e., Rs. 720,342. Therefore, the payback period will be 1.18 years.

Results

We conducted this detailed survey and analysis of the case study building of Awas Bhawan, Jaipur to identify the target areas and responsive retrofit measures for each of them. Each of the energy efficiency measures was simulated using EQuest to calculate the corresponding amount of energy saved. These measures were further compared and evaluated in terms of their cost, savings generated, and ease of implementation, to develop an optimum retrofit plan for the chosen building, using the ESCO route. In order to do that, 70% savings are used for ESCO repayment, whereas the remaining 30% are kept with the office.

Based on the results, it is observed that energy savings due to wall insulation are around 2% and due to roof insulation — around 0.4%. Approx. 0.4% of energy can be saved when all the window panes are replaced with tinted glass panes, approx. 1.2% of energy can be saved using double glazed panes with aluminum frames instead of the existing windows, and approx. 1.3% of energy can be saved by replacing the existing windows with double glazed

Table 13. Optimum retrofit plan with the ESCO repayment route

No.	EEM	Energy Saved (kWh)	Initial Cost	Annual Savings (Rs. 9/unit)	Payback Period (yrs)
1	Daylight sensors	7970	Rs. 487,000	Rs. 71,730	2.26
2	Occupancy sensors	15,970		Rs. 143,730	
3	5 star rated fans	61,950	Rs. 260,000	Rs. 557,550	0.47
4	VFD in central evaporative coolers	21,950	Rs. 60,000	Rs. 197,550	0.30
5	Shading devices	6500	Rs. 42,000	Rs. 58,500	1.39
	TOTAL	114,340	Rs. 849,000	Rs. 1,029,060	1.18

units with thermal break aluminum frames. The use of fins on the south-west and south-east faces results in energy savings of 0.60%. Replacing the existing lighting fixtures with energy-efficient fixtures can save around 10% of energy. Besides, 0.85% of energy can be saved by using daylight sensors and around 1.7% — by using occupancy sensors. The use of BEE 5 star rated fans can save around 6% of energy. Around 2.5% of energy can be saved by using VFD in central evaporative coolers.

It is seen that though energy-efficient lighting fixtures and solar panels produce the maximum energy savings in terms of the volume and payback period, the most optimum solutions are provided by VFD in central evaporative coolers and BEE 5 star rated fans with the approx. 0.4-year payback period in contrast to the 10-year payback period for lighting and solar panels.

Thus, the choice of EEMs to be undertaken, apart from depending on the amount of energy saved, mainly depends on the availability of financing, payback period, and building characteristics ensuring the ease of installation.

Recommendations

Having analyzed the results of the study, we give the following recommendations for energy-efficient retrofitting**:**

- Low-cost options can also be utilized to get similar results in case of budget constraints (e.g., the use of reflective films on glass panes).

- Government subsidies on energy-efficient lightings, fans and solar PVs can be very helpful in the case of such projects.

- Apart from the implementation of retrofit measures, proper maintenance is also very critical for the proper functioning of the elements according to the design. This can be achieved using BMS.

- Architectural design in terms of the orientation, size and placement of openings as well as the use of spaces is very significant for energy efficiency in buildings. No retrofit measures can fully compensate for that. Hence, prevention is better than cure.

- Presently, most of the energy-efficient products available in the market are intended for new construction, whereas the maximum amount of energy is consumed by existing buildings. Thus, the development of new products given retrofitting is urgently needed.

Conclusion

To develop an optimum energy-efficient retrofit strategy, both active and passive methods need to be considered and evaluated. Though the payback period serves as a great tool to assess the feasibility of various retrofit options, ease of installation, period of disruption in regular activities also need to be kept in mind while taking decisions regarding the optimum solution. The detailed analysis of various energy-efficient retrofit measures regarding the case study indicates that to achieve the best results, it is not necessary to go for difficult and expensive options, which might become unfeasible, keeping in mind the monetary perspective and ease of installation. The study reveals that the most feasible options for retrofit, resulting in optimum energy savings with short payback periods, include passive architecture measures like shading devices, equipment upgrade using energy-efficient fans, daylight and occupancy sensors, VFD in central air cooling, followed by such measures as the use of energy-efficient lighting fixtures and solar panels. The study shows that measures like insulation, window alteration using DGUs and thermal break aluminum frames seem to be lucrative at the first instance but are difficult to undertake since they are characterized by long periods of disruption, high costs, and large payback periods. With a payback period of only 1.18 years and high ease of installation, the optimum retrofit solution with passive façade alteration and selective equipment upgrade turns out to be the most feasible option for government offices in India and can be applied to other such buildings, especially in the composite region.

References

Abdullah, A. (2016). Sustainable and energy-efficient commercial retrofit: Case study of Perkins+Will Atlanta Office. *Perkins+Will Research Journal*, Vol. 08.01, pp. 48–66.

Ander, G. D. (2016). *Daylighting. WBDG Whole Building Design Guide.* [online] Available at: https://www.wbdg.org/resources/daylighting [Date accessed: 25.02.2020].

Aste, N. and Del Pero, C. (2013). Energy retrofit of commercial buildings: case study and applied methodology. *Energy Efficiency,* Vol. 6, Issue 2, pp. 407–423. DOI: 10.1007/s12053–012-9168–4.

Bureau of Energy Efficiency (2021). *Energy benchmarks for commercial buildings.* [online] Available at: https://beeindia.gov.in/sites/default/files/Flyer_22nd%20Jan.pdf [Date accessed: 19.05.2021].

Dascalaki, E. and Santamouris, M. (2002). On the potential of retrofitting scenarios for offices. *Building and Environment,* Vol. 37, Issue 6, pp. 557–567. DOI: 10.1016/S0360–1323(02)00002–1.

Dubois, M.-C., Bisegna, F., Gentile, N., Knoop, M., Matusiak, B., Osterhaus, W. and Tetri, E. (2015). Retrofitting the electric lighting and daylighting systems to reduce energy use in buildings: A literature review. *Energy Research Journal,* Vol. 6, Issue 1, pp. 25–41. DOI: 10.3844/erjsp.2015.25.41.

Energy Division, NITI Aayog (2015). *Energy efficiency interventions at NITI Aayog.* [online] Available at: https://niti.gov.in/sites/default/files/energy/Energy-Efficiency-Interventions-at-NITI.pdf [Date accessed: 02.09.2020].

Fiaschi, D., Bandinelli, R. and Conti, S. (2012). A case study for energy issues of public buildings and utilities in a small municipality: Investigation of possible improvements and integration with renewables. *Applied Energy,* Vol. 97, pp. 101–114. DOI: 10.1016/j.apenergy.2012.03.008.

Griego, D., Krarti, M. and Hernandez-Guerrero, A. (2015). Energy efficiency optimization of new and existing office buildings in Guanajuato, Mexico. *Sustainable Cities and Society,* Vol. 17, p. 132–140. DOI: 10.1016/j.scs.2015.04.008.

Hillebrand, G., Arends, G., Streblow, R., Madlener, R. and Müller, D. (2014). *Evaluation tool and retrofit matrix for office buildings.* E. ON Energy Research Center Series, Vol. 4, Issue 4. Aachen: RWTH Aachen University, 78 p.

India Insulation Forum (2015). *Thermal insulation of buildings. Stakeholder Awareness & Applicator Training.*

Inogate (2015). *Energy efficient lighting technologies, standards and potential savings.* [online] Available at: http://www.inogate.org/documents/1_Technologies__standards__potential_2015–12-15.pdf [Date accessed: 15.03.2021].

Kudarihal, C. S. and Gupta, M. (2015). Artificial lighting systems for energy efficiency. *Lighting India*, Vol. 10, No. 3, pp. 22–25.

Lunn, M. (2015). *Achieving energy efficiency through integrated lighting controls.* White Paper WP525001EN. [online] Available at: https://www.cooperlighting.com/s/lighting-stories/pdf/integrated-lighting-controls-wp525001en.pdf [Date accessed: 15.06.2020].

Ma, Z., Cooper, P., Daly, D. and Ledo, L. (2012). Existing building retrofits: Methodology and state-of-the-art. Energy and Buildings, Vol. 55, pp. 889–902. DOI: 10.1016/j.enbuild.2012.08.018.

NRDC (2013). *Saving money and energy: Case study of the energy-efficiency retrofit of the Godrej Bhavan building in Mumbai.* [online] Available at: https://www.nrdc.org/sites/default/files/energy-retrofit-godrej-bhavan-CS.pdf [Date accessed: 10.08.2020].

Olander, S. and Siggelsten, S. (2012). *Energy-efficient measures when retrofitting the existing building stock.* [online] Available at: http://www.co2olbricks.de/fileadmin/Redaktion/Dokumente/Publications/WP4-OP09_SE_Measures_Retrofitting.pdf [Date accessed: 18.09.2020].

Rey, E. (2004). Office building retrofitting strategies: multicriteria approach of an architectural and technical issue. *Energy and Buildings,* Vol. 36, Issue 4, pp. 367–372. DOI: 10.1016/j.enbuild.2004.01.015.

Roper, K. O. and Pope, B. (2014). Creating a framework for the successful implementation of energy retrofit projects. *Journal of Facilities Management,* Vol. 12, Issue 1, pp. 38–55. DOI: 10.1108/JFM-05–2013-0028.

Santamouris, M. and Dascalaki, E. (2002). Passive retrofitting of office buildings to improve their energy performance and indoor environment: the OFFICE project. *Building and Environment,* Vol. 37, Issue 6, pp. 575–578. DOI: 10.1016/S0360–1323(02)00004–5.

Sudhakaran, P., Joshi, B., Singh, G., Kumar, M. and Ansari, S. (2020). Performance simulation and validation of climate adaptive dynamic facades in campus buildings. *International Journal of Advanced Science and Technology,* Vol. 29, No. 6, pp. 4721–4736.

TERI (2013). *Roadmap for Incorporating energy efficiency retrofits in existing buildings.* [online] Available at: http://cbs.teriin.org/pdf/Energy_Efficiency_Retrofits_in_Existing_Buildings.pdf [Date accessed: 31.06.2020].

TERI (2021). *Window design for day lighting, ventilation and to reduce solar heat gains.* [online] Available at: https://silo.tips/download/chapter-3-window-design-for-day-lighting-ventilation-and-to [Date accessed: 19.05.2021].

Upadhyaya, V., Sudhakaran, P., Shukla, A. K., Kumar, S. and Joshi, B. (2018). Application of small-scale renewable energy techniques in traditional buildings of Jaipur. *International Journal of Civil Engineering and Technology,* Vol. 9, Issue 2, pp. 627–643.

Walker, A. (2016). *Natural ventilation. WBDG Whole Building Design Guide.* [online] Available at: https://www.wbdg.org/resources/natural-ventilation [Date accessed: 15.06.2020].

DOI: 10.23968/2500-0055-2021-6-2-18-30

ACOUSTIC SIMULATION OF THE CENTRAL HALL IN PALAU GÜELL BY GAUDÍ

Genaro González, Albert Samper, Blas Herrera*

Universitat Rovira i Virgili
Spain

*Corresponding author: blas.herrera@urv.cat

Abstract

Introduction: Quadric surfaces are commonly used in buildings due to their geometric ability to distribute and focus sound waves. The Central Hall in Palau Güell — a UNESCO World Heritage Site — is topped by an ellipsoidal dome. Antoni Gaudí envisaged this room as a concert hall where the organ and the dome play a lead role. **Methods**: The two previously mentioned elements are the main subject of our paper, which serves two purposes: 1) determining the values of the acoustic parameters of the hall through onsite measurement and also through simulation, and 2) using the geometric parameters of the quadric surface, which best fits the dome, in order to check whether it is possible to improve the acoustics of the hall by placing a new emission source at the focus of the dome's ellipsoid. **Results and Discussion**: Contrary to the authors' expectations, due to the focal reflection properties of the quadric surface, some acoustic parameters on the listening plane do not improve significantly. Therefore, we conclude that Gaudí took the acoustical impact into account when designing this hall.

Keywords

Ellipsoidal dome, acoustics, Palau Güell, Antoni Gaudí.

Introduction

The Palau Güell (1885–1890) is amongst the first important projects by Antoni Gaudí (1852–1926), and the only new construction he was able to finish. The building was commissioned by the Barcelona businessman Eusebi Güell Bacigalupi, who gave the architect total freedom in design (González et al., 2013).

One of the most representative spaces in Palau Güell is the Central Hall (Fig. 1). Apart from being the space around which the entire residence was arranged, it was created and designed to hold music recitals. Being a music lover, Eusebi Güell suggested that Gaudí's project should include a room where he could listen to live music in the company of friends and artists of their time. As a matter of fact, several Wagner operas were presented in Barcelona during the construction of Palau Güell, resulting in a Wagnerian craze in which Eusebi Güell took an active part (Granell, 2002; Lahuerta, 1992). This stirred up his interest in incorporating music into the palace's design. In addition to using the Central Hall for music recitals — even with choirs and an organ — its design was also suitable for religious services, conferences, and public lectures.

According to González et al. (2013), the decision to provide the palace with an organ was taken very early and had a direct impact on the geometric design of the hall. More specifically, the Central Hall is topped by an ellipsoidal dome with many small holes and a central eye, which ensure daylighting. The dome spans above a quadrangular area of approximately 60 m^2. The height to the central eye is 16.17 m. Throughout this height, the Central Hall musically and visually links three levels: a first level where the audience seats were arranged, a second level for the orchestra, and a third level for the choral ensembles. The organ pipes were installed between the third level and the dome. This hall has an approximate volume of 996.40 m^3 and it features ceramic tilings, marble ornaments, glass enclosures, and oak wood flooring. Therefore, a priori, it is a very reverberant space (Figs. 1 and 2).

Antoni Gaudí envisaged this room as a concert hall where the organ and the dome play a lead role. These two elements are directly involved in our calculations. The following are the topics covered in our paper:

a) Despite the interior finishes and the proportions of space, it is commonly claimed that the Central Hall in Palau Güell has good acoustics. Nonetheless, we are not aware of any rigorous study, which quantifies the acoustic quality at the listening plane, where the audience sat. This paper provides a measure of the acoustic parameters.

b) We are not aware of any original documents by Gaudí explaining the reasons why he designed an ellipsoidal dome. Quadric surfaces are commonly used in theaters, stadiums, and public venues due to their geometric ability to distribute and focus sound (Kircheri, 1673; León-Rodríguez, 1998). Based on

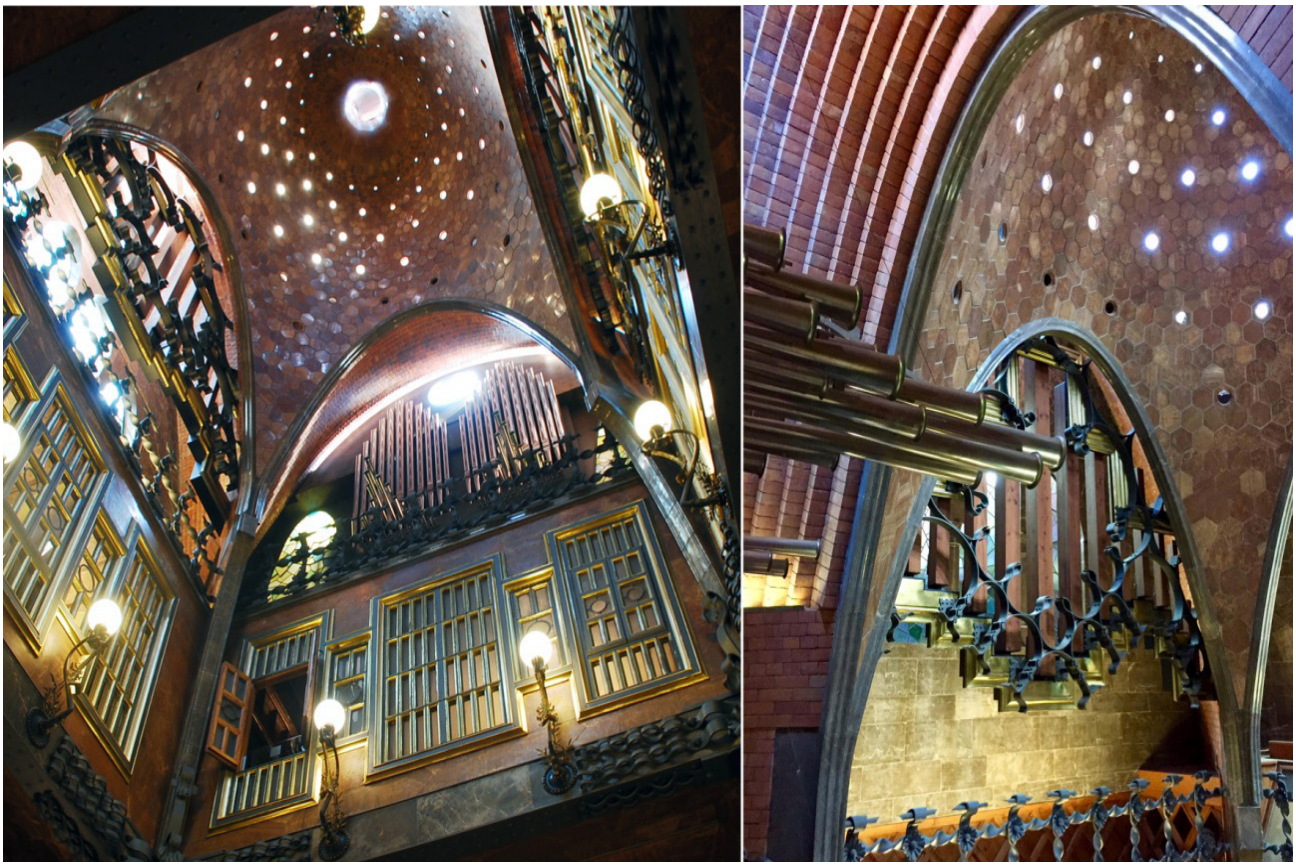

Figure 1. Images of the Central Hall in Palau Güell, showing the two main elements considered in this paper: the ellipsoidal dome and the organ (photos taken by the authors)

the architectural application of these geometric and acoustics properties throughout history, it is important to note that Gaudí designed an ellipsoidal surface in order to adequately distribute the organ sound throughout the entire room. In this paper, we determine the acoustic impact of the dome's surface on the listening plane (where the audience sat).

c) In addition to the foregoing, we analyzed the geometric parameters of the quadric surface, which best fits the dome, and placed the emission source in different positions, but — contrary to our expectations — we did not succeed in significantly improving some of the acoustic parameters at the listening plane. Accordingly, despite the absence of a historical document supplying proof in this regard, we claim that Gaudí took the acoustical impact into account when designing this hall.

In order to investigate these topics, we will generate a virtual simulation of this architectural space. This geometric simulation will enable us to gain a better understanding of the acoustic characteristics and the intelligibility of voice and music in the hall. Our investigation is along the same lines as other research works, such as works on Pompeii's Odeon (Berardi et al., 2016), the Santiago de Compostela Cathedral (Suárez et al., 2015), and the Basilica of San Vitale in Ravenna (Tronchin and Knight, 2016), as well as the Granada Cathedral (Alonso et al., 2017) and the Seville Cathedral (Alvarez-Morales et al., 2017). Virtual and simulated geometrical acoustics studies by D'Orazio et al. (2016), Segura et al. (2011) and Sender et al. (2018) should also be mentioned.

PRELIMINARY REMARKS

After defining the study object and the two main elements of the Central Hall, which will be used for this acoustic analysis (the organ as the emission source, and the ellipsoidal dome as the distributing element), we formulate two arrangement cases and generate their respective acoustic simulations, focusing mainly on the music and speech acoustics indicators.

Case 1: For this acoustic simulation of the Central Hall, the emission source is placed at the organ's location (Gaudí's original design), and the sound receivers are evenly distributed across the audience area at a height of 1.20 m above the floor level (listening plane). Previous to this acoustic simulation, we collected experimental data onsite by placing the emission source at the organ's location and by placing the sound receivers at the same level and the same places as defined for the simulation.

This first case is aimed at 1) confirming or disproving the common claim that the Central Hall of Palau Güell has good acoustics, and 2) providing a measure of the abovementioned acoustic parameters (Fig. 2).

Case 2: For this acoustic simulation of the Central Hall, the emission source (emitting the same tone as for Case 1) is placed at the upper focal point of the ellipse, resulting from the intersection between a vertical plane and the quadric surface, which best fits the dome, and the sound receivers are evenly distributed across the listening plane as in Case 1 (Fig. 2). The best-fitting quadric surface is an ellipsoid.

The parameters studied, grouped according to the main subjective sensations (Gimenez, 1989, 2001), are:

- Reverberation parameters: T30 and EDT (Reverberation Times), Br (Brilliance).
- Energy parameters: C50 (Clarity for speech) and C80 (Clarity for music), G (Strength).
- Intelligibility parameters: STI.

The main subjective qualities of the concert halls are related to the following parameters:

- Reverberation: It represents the degree of vivacity of the hall.
- Transparency: It is important when hearing music. Transparency refers to the perception of separate tones in time and instruments played simultaneously.
- Intelligibility: this parameter quantifies speech comprehension and is essential for hearing speech.

Furthermore, we took into account the values of Just Noticeable Difference (JND), which is the minimum variation of an acoustic parameter that a person can detect. It is currently considered to be the best indicator with which to assess the subjective perception of variations in acoustical parameters.

Methods

Experimental data were collected in the empty hall and according to the specifications of ISO 3382–1:2009. These measurements allowed us to calibrate the hall as it is now and they also allowed us to validate the simulated parameter values obtained for Case 1. In order to validate the simulated values, we assigned sound absorption and sound scattering properties to each modeled surface. After validating the simulated parameter values for Case 1, we compared the two cases stated in this paper. It should be mentioned that the diffraction phenomenon was taken into account. The experimental data were collected using WinMLS2004 software.

The acoustic simulation of the two abovementioned cases was made using CATT Acoustic software (v9.0c). This commercially available software is supported by 3D modeling tools. For the 3D modeling of the hall, we used SketchUp software. Using the generated 3D models, CATT Acoustic simulates sound propagation and provides echograms and synthesized room impulse responses (RIRs). We analyzed the acoustic parameters related to music and speech. Using these tools, we replicated the sound environment of the Central Hall in Palau Güell and obtained simulated acoustic parameter values to be compared with our experimental data. This enabled us to validate these simulated parameter values.

The steps followed:

— Step 1: We collected experimental data onsite at the Central Hall in Palau Güell.

— Step 2: We created a three-dimensional model of the Central Hall. This model is a prerequisite to carry out the simulation.

However, CATT Acoustic can only read 3D polygonal models; it cannot use point clouds or analytical equations. For this reason, we used SketchUp software to model the Central Hall.

Our model consists of two parts: the dome and the rest of the hall. Everything, except for the dome, was modeled on the basis of existing drawings (provided to us by the Diputació de Barcelona) and a whole set of laser measurements and verifications that we carried out onsite.

Before creating a 3D rendering of the dome, we had to use other techniques, the steps of which are described briefly below:

A) Using photogrammetric techniques and PhotoScan software, we generate a cloud $N=\{P_i\}_{i=1}^{i=n}$ made up by $n = 2{,}145{,}493$ points forming the dome (Fig. 3).

B) By means of a quadratic surface regression, we obtain the quadratic surface, which best fits the dome. It turns out to be an ellipsoid, so we find its equation and geometric parameters. In order to do that, we use the mathematical procedure outlined hereafter: For the points P_i, we use 3D coordinates according to the 3D orthonormal coordinate *(x', y', z')* system $\mathcal{R}'=\{O;\vec{u}_1,\vec{u}_2,\vec{u}_3\}$ of the scanning device. We calculate , which is the regression quadratic surface for , and we obtain its general equation, Eq. (1), in the reference system R':

$$\Gamma\equiv 0=B_0x'^2+C_0y'^2+D_0z'^2+E_0x'y'+F_0x'z'+ G_0y'z'+H_0x'+I_0y'+J_0z'+1. \quad (1)$$

This regression surface Γ is the one that best fits the point cloud , minimizing the sum of the quadratic residues $\sum_{i=1}^{i=n}\varepsilon_i^2=\sum_{i=1}^{i=n}\left(B_0x'_i{}^2+C_0y'_i{}^2+D_0z'_i{}^2+E_0x'_iy'_i+F_0x'_iz'_i+G_0y'_iz'_i+H_0x'_i+I_0y'_i+J_0z'_i+1\right)^2$.

In order to solve Eq. (1), we solve the corresponding Gauss normal equations. Thus, we obtain: $B_0 = -0.0033$, $C_0 = -0.0028$, $D_0 = -0.0012$, $E_0 = 0.0008$, $E_0 = 0.0008$, $G_0 = -0.0027$, $H_0 = 0.1091$, $I_0 = 0.0531$, $J_0 = 0.0378$. After making the classical algebraic calculations for quadratic surface classification, we find that surface is an ellipsoid.

Next, we calculate the orthonormal reference system $R=\{\theta;\vec{e}_1,\vec{e}_2,\vec{e}_3\}$, where is the center of the ellipsoid Γ and $\{\vec{e}_1,\vec{e}_2,\vec{e}_3\}$ are three orthonormal direction vectors for the three axes of Γ, such that $\vec{e}_3$ is pointed vertically up to the dome. The points in reference system R have coordinates

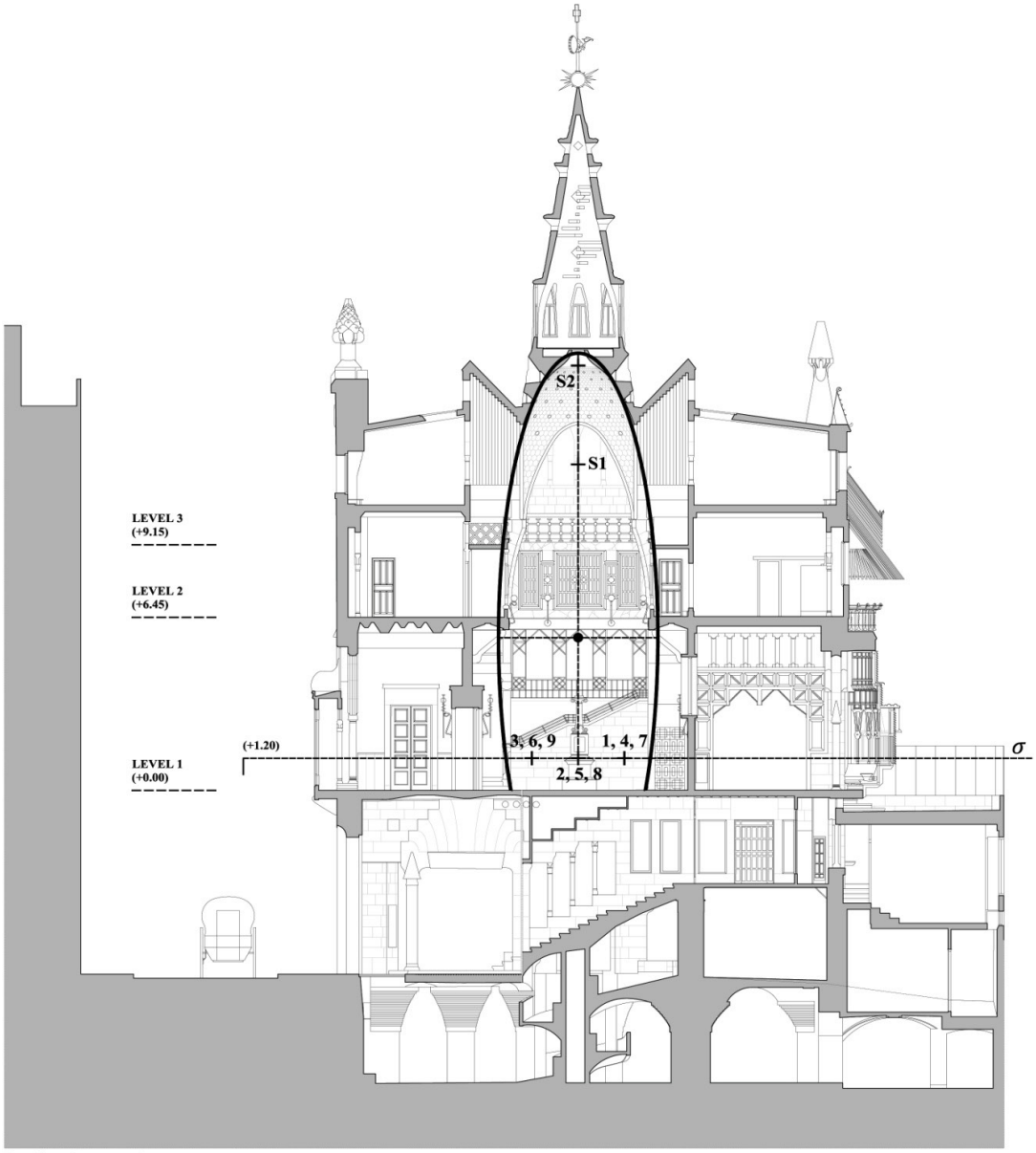

Figure 2. Cross-section and plan view for Level 1 of the Central Hall in Palau Güell, showing the positions S1, S2 and an ellipse. S1 marks the position of the organ in Level 3, on the opposite wall from that drawn in section T-T'. S2 marks the position of one focal point of the ellipse, resulting from the intersection between a central vertical plane and the best-fitting quadric surface. This ellipse is outlined with a thick black line. Besides, both in the cross-section and in the plan view, we outline plane or listening plane, where nine receivers are placed (at a height of 1.20 m above Level 1). Vector shows the listening plane orientation detailed in Figs. 5 and 6. This graphic document is reproduced with kind permission of the Arxiu del Servei de Patrimoni Arquitectònic Local de la Diputació de Barcelona

(x, y, z). For this calculation, we consider that $\{\vec{e}_1,\vec{e}_2,\vec{e}_3\}$ are eigenvectors of the matrix A_{00}, and the coordinates of Θ are obtained as a solution of system

$$A_{00}\vec{x}^t=\left(\frac{H_0}{2},\frac{I_0}{2},\frac{J_0}{2}\right)^t.$$

The coordinates of the points from cloud N are changed from reference system R' to reference system R. In addition to this change, we carry out a normalization consisting of the following three steps. First, the entire cloud N is translated in the direction of vector $\vec{e}_3$ until point D, the lowest point of N, is in plane z = 0. Second, we carry out a homothetic transformation of the entire cloud N with center on Θ and homothetic ratio ρ such that the distance between point D and Θ is 1. Third, we rotate the entire cloud N around the axis of $\vec{e}_3$ until the coordinates of point D in the system R are (1,0,0). Thus, we obtain a normalized cloud $N=\{P_i=(x_i,y_i,z_i)\}_{i=1}^{i=n}$ with D=(1,0,0) in system $R=\{\theta;\vec{e}_1,\vec{e}_2,\vec{e}_3\}$, , where $\vec{e}_3$ is the direction vector for the axis of N; the new coordinates for the points of cloud N in system R are (x_i, y_i, z_i). After all the above calculations, we obtain the new general Eq. (2) for Γ, which is the normalized general equation of in system R:

$$\Gamma\equiv 0=B_1x^2+C_1y^2+D_1z^2+E_1xy+J_1z+1. \qquad (2)$$

The coefficients of Eq. (2) for this ellipsoid Γ are as follows: B_1=-0.9456, C_1=-0.9362, D_1=-0.0759, E_1=0.0087, J_1=-0.3181.

This Eq. (2) allows us to easily find the coordinates of all the geometric elements involved in this paper.

C) The ellipsoid is modeled with AutoCad based on Eq. (2) of the quadratic surface Γ .

D) The surface is exported to SketchUp, where it is polygonized and joined to the other part of the model.

The end result is a 3D model of the Central Hall made up by 10,237 polygonal shapes, 4110 of which correspond to the surface of the ellipsoidal dome (Fig. 3).

— Step 3: After importing the 3D model into CATT Acoustic, each and every polygonal shape of the model is assigned the properties of its constituent material — texture, porosity, and finish — as well as an absorption parameter and a scattering coefficient.

— Step 4: In the acoustic simulations, the emission source and the sound receivers are positioned according to the abovementioned cases.

4.a. Case 1: An omnidirectional emission source is placed at the organ's location (position S1 in Fig. 2). Nine sound receivers are evenly distributed in a grid layout on plane σ parallel to the room's floor at a height of 1.20 m.

4.b. Case 2: An omnidirectional emission source is placed at the upper focal point of the ellipse, resulting from the intersection between a central vertical plane and the ellipsoid Γ, which best fits the dome (position S2 in Fig. 2). Exactly as for Case 1, nine sound receivers are evenly distributed in a grid layout on plane σ parallel to the room's floor at a height of 1.20 m.

— Step 5: Finally we make the corresponding calculations (with CATT Acoustic) in order to find out the main acoustic parameters for both cases. All parameters obtained are averaged values according to ISO 3380–1:2009, for frequencies from 125 Hz to 8 kHz.

ACOUSTIC MEASUREMENTS

As already stated, in order to validate the simulated acoustic values, we collected experimental data onsite. We were only able to collect these experimental acoustic data with the emission source at the position S1. In order to place our emission

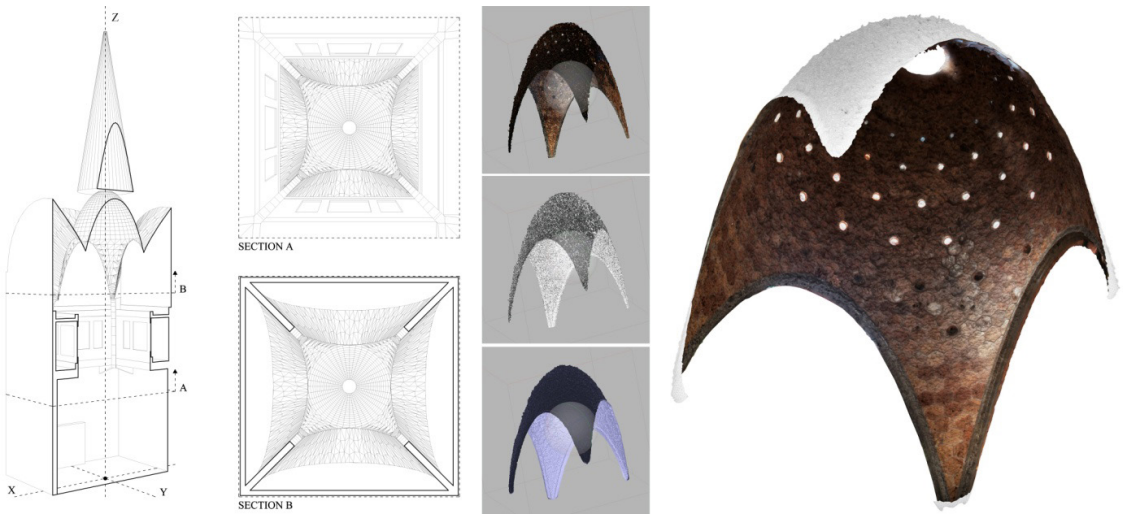

Figure 3. On the right: three-dimensional mesh and textured model based on the point cloud imported into PhotoScan. On the left: three-dimensional model of the Central Hall as imported into CATT Acoustic. This object is generated using SketchUp software, and it is made up by 10,237 polygonal shapes, 4110 of which correspond to the ellipsoidal surface of the dome (image generated by the authors)

source at the position S2 (the focal point of the ellipsoid), it would have been necessary to put up scaffolding at the Central Hall of Palau Güell. Since this is a very important building in Gaudí's work, we were not authorized to do so. For this reason, we were not able to collect experimental data for our second case, with the emission source at S2.

Experimental data for RIRs were collected in the empty hall and according to ISO 3382–1:2009. The Exponential Sine Sweep (ESS) technique (512 k at 48 kHz) allowed a proper signal-to-noise ratio (> 45 dB) in each octave band, according to ISO 3382 requirements (ISO 3382–1:2009). One high-SPL dodecahedron and nine monoaural microphones were used simultaneously in order to carry out the whole survey during one day of measurement (D'Orazio et al. 2016). During our measurements, the temperature in the hall ranged between 12 and 14°C, and the relative humidity ranged between 70 and 75%. The microphone was placed 1.2 m above the floor level, at the locations marked in Fig. 2.

1. GEOMETRIC CHARACTERISTICS OF THE VIRTUAL MODEL

The acoustic simulation allowed us to assess the acoustic behavior of the hall for one of our cases. The virtual acoustic model was generated from the 3D model described in step 2 above. This 3D model was exported to CATT-Acoustic v.9.0. Table 1 shows the most relevant geometric characteristics of the model used by us.

Table 1. Geometric characteristics of the virtual model

Floor surface (m^2)	66.74
Volume (m^3)	1033.88
Total surface (m^2)	1228.75
Length/width/height (m)	8.17/8.17/25.20
No. of faces	10,267

2. VIRTUAL MODEL CALIBRATION

The acoustic properties of the surface materials in the 3D model are assigned by means of the parameter values shown in Table 2.

Table 2. Sound absorption coefficients associated to materials in order to calibrate the model (α: absorption coefficient, s: scattering coefficient).

Material	Surface (%)	α	125 Hz	250 Hz	500 Hz	1 kHz	2 kHz	4 kHz
Stone (Bork, 2005)	46.4	α	0.07	0.07	0.05	0.07	0.08	0.08
		s	0.20	0.24	0.28	0.32	0.36	0.40
Marble or glazed tile (Vorländer, 2007)	13.1	α	0.01	0.01	0.01	0.02	0.02	0.02
		s	0.05	0.10	0.20	0.35	0.45	0.50
Plaster (Vorländer, 2007)	1.6	α	0.01	0.01	0.02	0.03	0.04	0.05
		s	0.10	0.10	0.10	0.10	0.10	0.10
Organ (Alonso et al., 2014)	1.5	α	0.12	0.14	0.16	0.16	0.16	0.16
		s	0.30	0.40	0.50	0.60	0.70	0.80
Windows (Meyer, 2003)	2.2	α	0.35	0.25	0.18	0.12	0.07	0.04
		s	0.01	0.01	0.05	0.10	0.20	0.25
Solid wooden doors (Bork, 2005)	1.4	α	0.14	0.10	0.06	0.08	0.10	0.10
		s	0.30	0.40	0.50	0.60	0.70	0.80
Wood (Vorländer, 2007)	1.4	α	0.10	0.15	0.18	0.20	0.20	0.20
		s	0.05	0.10	0.20	0.35	0.45	0.50

3 VIRTUAL MODEL VALIDATION

The values obtained for reverberation time (T30) do not exceed 1 JND. A value of 1 JND is an adequate value for parameter C80 according to Martellota (2010). The values for strength (G) are around 1.5 JND. The values for definition (D50) exceed 2 JND for middle and low frequencies. The values obtained are shown in Fig. 4.

In conclusion, these experimental values allow us to validate the values obtained with the acoustic simulation and analyze the stated cases.

Results

ANALYTICAL RESULTS

The acoustic model simulations provide the room impulse response (RIR) for each receiver, as well as detailed information on the acoustic characteristics of the Central Hall in Palau Güell. We present the results for spatial impression, perceived

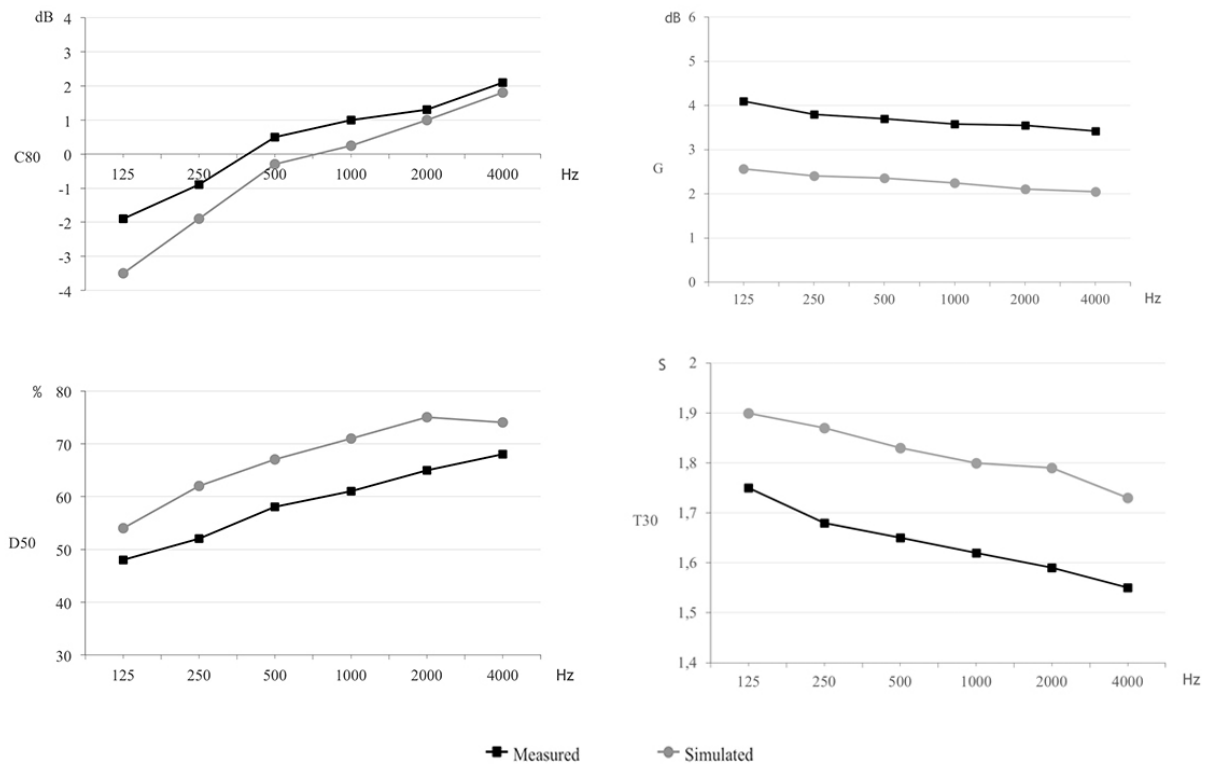

Figure 4. Case 1, comparison of the mean values for parameters C80, G, D50 and T30, as obtained through onsite measurement and through simulation

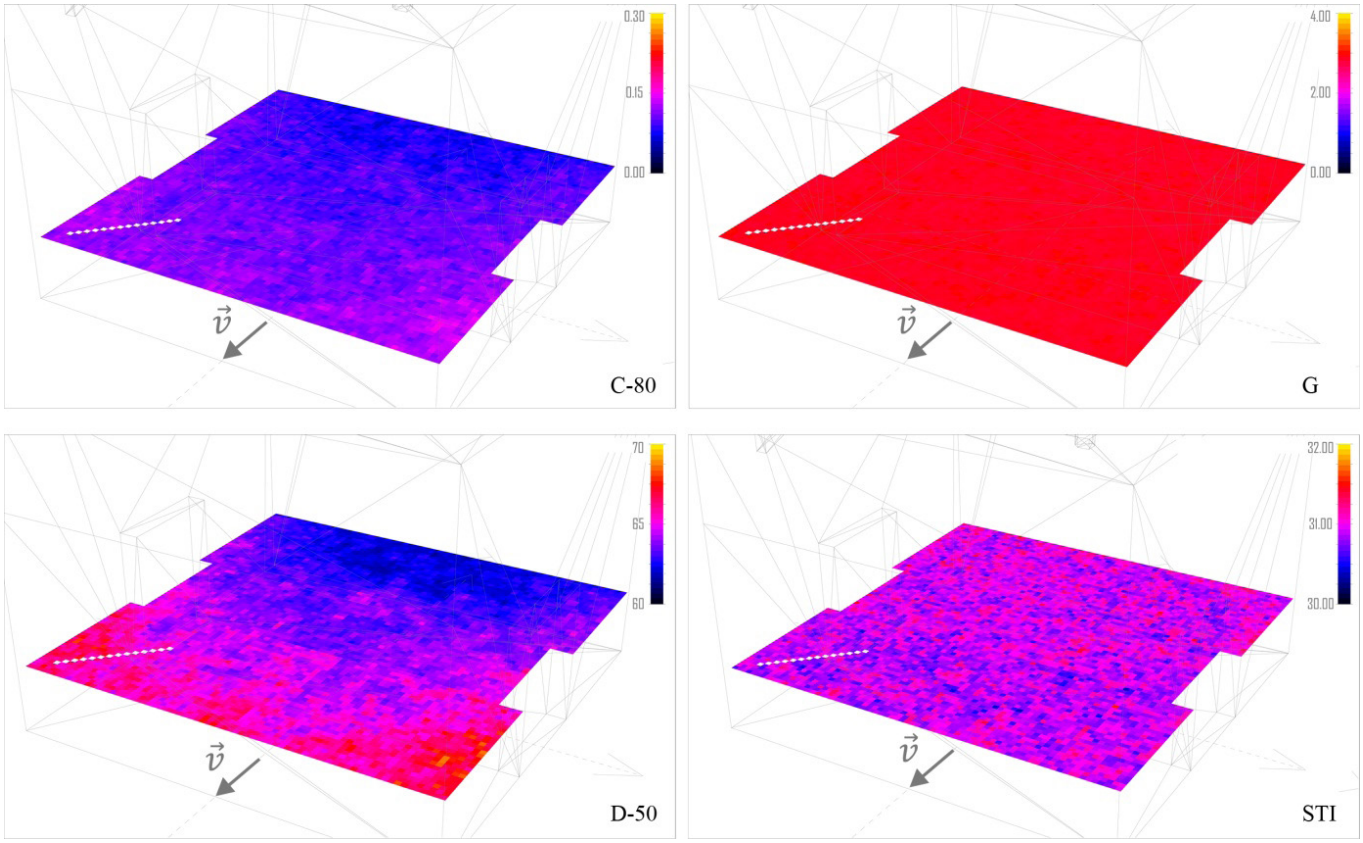

Figure 5. Distribution of the parameters C80, G, D50 and STI for Case 1. Vector determines the orientation of plane σ in Fig. 2

reverberation, and transparency & intelligibility of speech and music.

With regard to spatial impression, we calculated the value G. With regard to perceived reverberation, we calculated the T30 values. As for the study of transparency and intelligibility of speech and music, we calculated the parameters C80, D50 and STI, as well as the Br values.

The values obtained for all sound receivers are shown in Table 3 (with a frequency of 1 kHz) and Table 4. Figs. 5 and 6 show the spatial distribution of several parameter values on plane σ (see location in Fig. 2).

Table 3. Average simulation values obtained for both cases

Parameters	Unit	Source	Receivers								
			P1	P2	P3	P4	P5	P6	P7	P8	P9
G	dB	S1	3.68	3.9	3.75	3.45	2.90	2.75	2.53	2.31	1.98
		S2	2.45	2.56	2.41	2.35	2.25	2.11	2.05	1.85	1.55
T30	s	S1	1.78	1.78	1.79	1.79	1.81	1.78	1.82	1.81	1.82
		S2	1.93	1.92	1.93	1.95	1.95	1.93	1.94	1.93	1.92
		S2	5.43	5.44	5.43	5.43	5.40	5.44	5.40	5.45	5.43
C80	dB	S1	0.27	0.23	0.27	0.25	0.24	0.24	0.12	0.13	0.12
		S2	-1.92	-1.94	-1.94	-1.94	-1.37	-1.95	-1.94	-1.95	-1.93
D50	%	S1	67.6	67.7	67.6	67.1	66.7	66.8	64.7	64.4	64.5
		S2	38.2	39.5	38.8	40.3	42.6	40.7	39.6	40.6	39.1
STI	%	S1	30.9	31.4	30.7	31.5	31.1	31.1	30.1	29.8	30.2
		S2	33.9	33.5	33.7	34.2	44.3	34.4	33.8	33.2	33.7

Table 4. Average simulation values obtained for both cases

Parameters	Source	Receivers								
		P1	P2	P3	P4	P5	P6	P7	P8	P9
Br	S1	0.94	0.95	0.93	0.93	0.92	0.94	0.95	0.95	0.94
	S2	0.93	0.95	0.92	0.93	0.92	0.95	0.95	0.95	0.95

SIMULATION RESULTS

After presenting the analytical results of the simulation (Figs. 5, 6 and Tables 3, 4), we shall now show the impact of each case on the Central Hall acoustics on the basis of: spatial impression, perceived reverberation, and intelligibility of speech and music.

The obtained values are compared to the recommended values. Scientific literature has consolidated several objective acoustic parameters, which characterize the sound environment of an architectural space. Even though these scientific papers usually refer to concert halls and theaters, they can be extrapolated to this hall in view of its intended use (Ando, 1983, 1985; Barron, 1993; Beranek 1996, 2004).

First case: Emission source at position S1 (organ's location)

Fig. 5 shows the distribution of several parameter values in the hall when the emission source is placed at the organ's location (S1). For the parameters C80 and D50, this distribution is dependent on the position of the emission source. Conversely, the distribution of the G values is uniform across the entire listening plane for all frequencies.

The sound strength (G) values in the empty hall lie in the range of 2 to 4 dB (for the frequency interval between 125 Hz and 4 kHz). These values would be good for a concert hall, according to Beranek (1996).

The reverberation time T30, with values close to 1.78 s, is considered acceptable for theater and chorus recitals, according to Beranek (1996). Conversely, Meyer (1993) considers that the appropriate values for organ music are those between 2.5 and 3.0 s.

The music clarity in the room is good, with the C80 values in the range -2dB > C80 > 2dB. The sound is optimal for a concert hall, according to Barron (1993) and Marshall (1994).

The obtained values for the parameter D50 at places near the emission source position S1 are good for opera halls and theaters according to Arau (1999). The clarity of speech decreases at the corners opposite to the emission source.

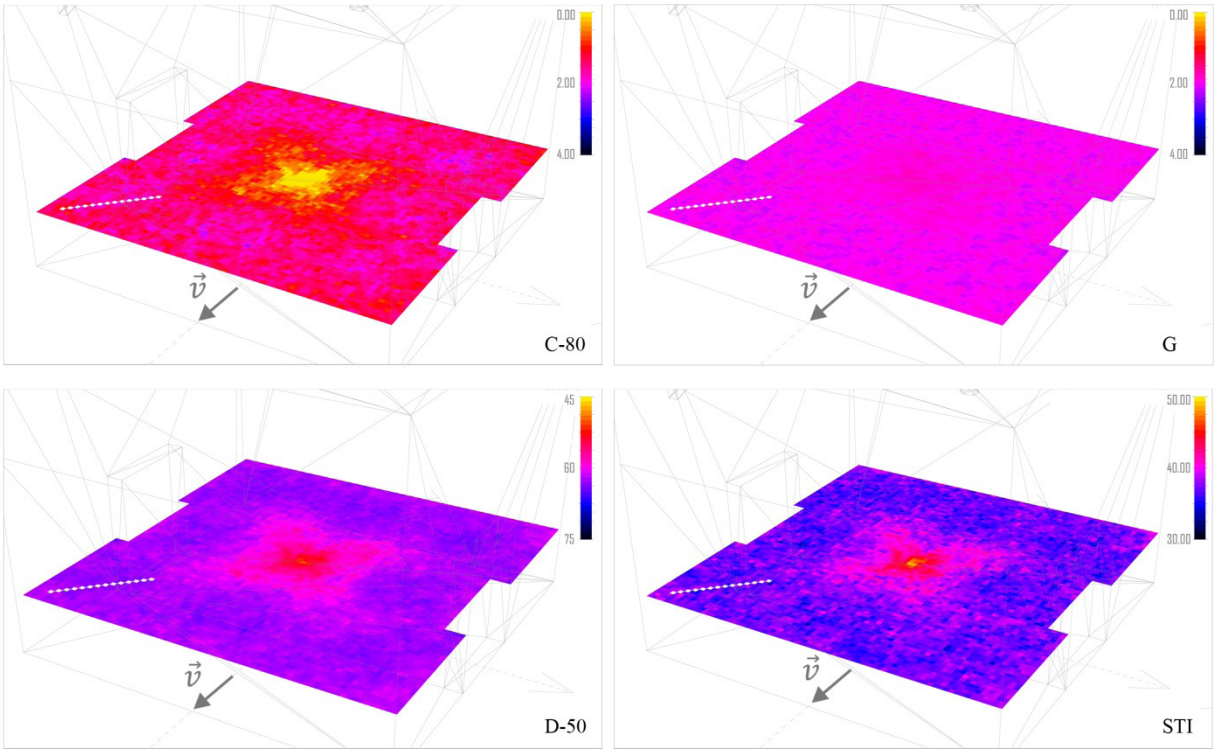

Figure 6. Distribution of the parameters C80, G, D50 and STI for Case 2. Vector $\vec{v}$ determines the orientation of plane σ in Fig. 2

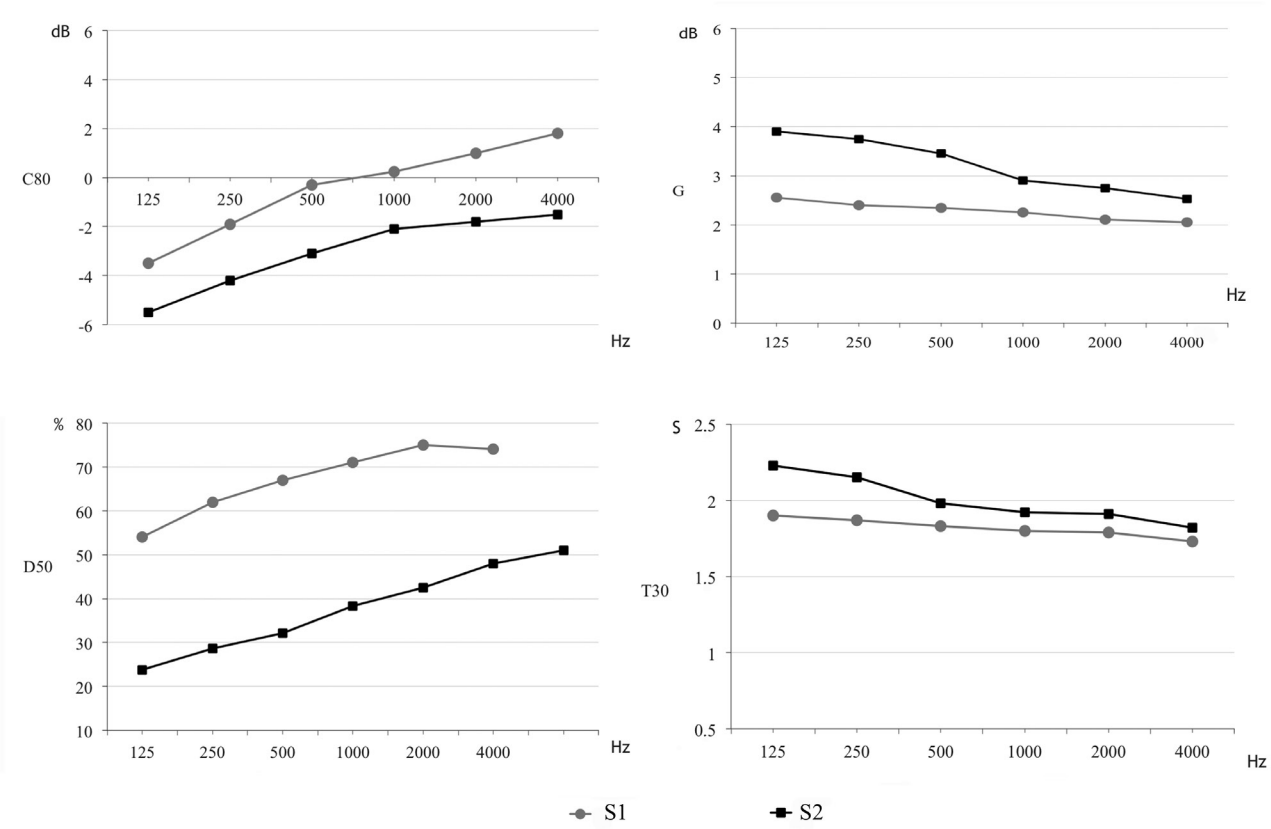

Figure 7. Comparison of the mean values for the parameters C80, G, D50 and T30, as obtained through simulation with the emission source at the organ's location, position S1 (Case 1), and through simulation with the emission source at the focal point of the ellipsoid, position S2 (Case 2)

The values for speech intelligibility (STI) are considered to be fair according to Arau (1999). The obtained values are not regularly distributed.

We calculated the high-frequency response value (Br), which is close to 1, suitable for concert halls and theaters. This is a bright room, and the sound is clear and rich in harmonics according to Arau (1999).

The mean value for low-frequency richness (BR) is 0.94. This value is far from satisfying the strict criterion of warmth for rooms devoted to music. Nonetheless, it is an adequate value for a room that hosts theater plays and dissertations, according to Arau (1999).

Second case: Emission source at position S2 (the focal point of the ellipsoid)

The sound strength of the hall reaches G values of up to 2 dB (for the frequency interval between 125 Hz and 4 kHz), which are good for a concert hall, according to Beranek (1996). As with the first case, the distribution of the G values is almost constant across the entire listening plane.

However, the rest of the parameters are affected by the position of the emission source (S2 in this case). The values obtained for the second case differ strongly from those obtained for the first case. The calculated T30 values are optimal for a room that hosts organ and choral recitals, according to Beranek (1996) (Fig. 6).

The calculated music clarity values (C80) lie in the range from -5 to 0 dB. These are the recommended values for listening to symphonic music, according to Beranek (1996). With high frequencies (higher than 1 kHz), the values lie within the range recommended by Barron (1993) and Marshall (1994). According to Arau (1999), the definition values (D50) obtained are good for concert and opera halls. The STI values are medium-high (Arau, 1999).

The calculated high-frequency response value (Br) is close to 1, which indicates again that the sound is rich in harmonics. The BR values obtained for Case 2 are below 1. This is not optimal for a hall that hosts music recitals, but it is good enough for conference rooms or theater halls according to Arau (1999) (Table 5).

Discussion

In the light of the results shown in the previous section, we note the following considerations:

As far as the parameter G is concerned, the subjective spatial impression of the room is good in both cases. The values obtained are similar for both cases. The spatial distribution of these values is almost constant for both cases.

The T30 values for both cases suggest that the hall is especially suited for listening to choral recitals and also for theater plays. These were the most commonly used musical forms in the Central Hall in Palau Güell. Despite their low sound absorption and high sound scattering properties, the construction materials used in the hall do not affect the T30 values.

The music clarity values (C80) are good in both cases, which means that the hall is well suited to accommodate concerts. However, the distribution of these values on the listening plane is affected by the position of the emission source. Specifically, the spatial distribution resulting from placing the emission source at the organ's location (position S1) fits better with the original use as a concert hall, where the audience was facing the performer (Fig. 5).

The definition values (D50) are good in both cases. Nonetheless, the hall shows a better response for concerts when the emission source is placed in position S1. The distribution of D50 on the listening

Table 5. Reference values for various parameters

Parameter	Unit	Author	Use of hall	Reference values
G	dB	Beranek	Concert hall	2.00–6.00
T30	s	Beranek	Theater	0.70–1.20
		Meyer and Newman	Organ music	2.50–3.00
C80	dB	Beranek	Concert hall	C80 < -4.0 / C80 > 0.00
		Barron and Marshall	Concert hall	C80 < -2.0 / C80 > 2.00
		Arau	Concert hall	C80 < 4.0 / C80 > 0.00
			Theater	C80 < 6
D50	%	Arau	Theater	D50 > 60
			Concert hall	50 < D50 < 65
STI	%	Arau	Concert hall	0.45–0.60 (acceptable)
				0.60–0.75 (good)
				0.75–1 (excellent)
Br		Arau	Concert hall	0.80–1.00

plane is affected by the position of the emission source. As was the case with the parameter C80, the distribution resulting from placing the emission source at the organ's location (position S1) fits better with the original use of the hall (Fig. 5).

The high-frequency response value (Br) is close to 1 in both cases. This translates into a bright room where the sound is clear and rich in harmonics, which is excellent for listening to sound nuances in music.

The BR values obtained for Case 2 are similar to those obtained for Case 1. These values are not correct for a room that hosts music recitals, but they are adequate for a hall where speech plays a central role.

Conclusions

Despite the interior finishes and the proportions of space, it is commonly claimed that the Central Hall in Palau Güell has good acoustics. Nonetheless, we are not aware of any rigorous study supporting this impression of acoustic comfort. Furthermore, we are not aware of any original document by Antoni Gaudí explaining why he chose an ellipsoidal dome for this hall or whether this was a deliberate choice, knowing that these surfaces — which are well known since ancient times — provide a good sound distribution in indoor spaces.

After carrying out the acoustical simulations for both cases (Case 1, corresponding to Gaudí's original design; and Case 2, placing the emission source in a different position, which is determined by the geometric parameters of the ellipsoidal dome, in an effort to improve the room acoustics), the following conclusions can be drawn:

1. The values obtained for C80, D50 and G are good in both cases. Taken as a whole, they are very adequate for this particular hall, the purpose of which is listening to organ and choral music.
2. After analyzing the parameters G, D50, C80 and T30 with the emission source at the organ's location (Case 1), we find that the spatial distribution of these values at the listening plane takes the shape of the area where the audience sat during the concerts held at the hall.
3. Owing to the size and proportions of the hall, the reverberant materials used do not excessively hinder the optimal values for listening to music.
4. Contrary to our expectations, despite having analyzed the geometric parameters of the quadratic surface, which best fits the dome, and placing the emission source in a different position, which is geometrically determined by the dome, we have not succeeded in significantly improving some of the acoustic parameters on the listening plane. Accordingly, despite the absence of a historical document supplying proof in this regard, we believe that Gaudí took the acoustical impact into account when designing this hall.

All the acoustical parameters considered by us in reaching the conclusion that this hall is very well suited for accommodating recitals were unknown at the time the building was constructed. Therefore, Gaudí could not possibly have taken them into account when designing this hall. In spite of that, Gaudí's design fulfills, to a very satisfactory degree, all musical requirements that may apply to a hall specially designed for hosting music recitals.

Finally, we conclude that Gaudí designed an acoustically controlled hall by compensating for the use of reverberant materials with a good geometric conception. The characteristics of the hall — very elongated and topped by an ellipsoidal dome — provide good acoustics. Besides, Gaudí took advantage of the dome's geometry and positioned the sound source (organ and choir) in such a way that the audience, who were sitting facing the performer, enjoyed the best possible listening experience.

References

Alonso, A., Sendra, J.J., Suarez, R. and Zamarreño, T. (2014). Acoustic evaluation of the cathedral of Seville as a concert hall and proposals for improving the acoustic quality perceived by listeners. *Journal of Building Performance Simulation,* Vol. 7, Issue 5, pp. 360–378. DOI: 10.1080/19401493.2013.848937.

Alonso, A., Suárez, R. and Sendra, J. J. (2017). Virtual reconstruction of indoor acoustics in cathedrals: The case of the Cathedral of Granada. *Building Simulation*, Vol. 10, Issue 4, pp. 431–446. DOI: 10.1007/s12273–016-0342-z.

Ando, Y. (1983). Calculation of subjective preference at each seat in a concert hall. *The Journal of the Acoustical Society of America*, Vol. 74, Issue 3, pp. 873–887. DOI: 10.1121/1.389874.

Ando, Y. (1985). *Concert hall acoustics*. Berlin: Springer, 154 p.

Arau, H. (1999). *ABC de la acústica arquitectónica*. Barcelona: CEAC, 336 p.

Barron, M. (1993). *Auditorium acoustics and architectural design*. London: E & FN Spon, 504 p.

Beranek, L. L. (1996). *Concert and opera halls: how they sound*. Woodbury, NY: American Institute of Physics, 643 p.

Beranek, L. (2004). *Concert halls and opera houses: music, acoustics, and architecture*. 2nd edition. New York: Springer, 661 p.

Beranek, L. L. (2008). Concert hall acoustics. *Journal of the Audio Engineering Society*, Vol. 56, No. 7/8, pp. 532–544.

Berardi, U., Iannace, G. and Maffei, L. (2016). Virtual reconstruction of the historical acoustics of the Odeon of Pompeii. *Journal of Cultural Heritage*, Vol. 19, pp. 555–566. DOI: 10.1016/j.culher.2015.12.004.

Bork, I. (2005). Report on the 3rd round robin on room acoustical computer simulation — Part II: Calculations. *Acta Acustica United with Acustica*, Vol. 91, No. 4, pp. 753–763.

Bradley, J. S., Reich, R. and Norcross, S. G. (1999). A just noticeable difference in C50 for speech. *Applied Acoustics*, Vol. 58, Issue 2, pp. 99–108. DOI: 10.1016/S0003–682X(98)00075–9.

Carrión, A. (1998). *Diseño acústico de espacios arquitectónicos*. Barcelona: Edicions UPC, 434 p.

D'Orazio, D., De Cesaris, S., Guidorzi, P., Barbaresi, L., Garai, M. and Magalotti, R. (2016). Room acoustic measurements using a high SPL dodecahedron. In: *Proceedings of the 140th Audio Engineering Society Convention, June 4–7, 2016, Paris, France*. Paper 9507. [online] Available at: http://www.aes.org/e-lib/browse.cfm?elib=18206 [Date accessed January 29, 2020].

Giménez, A. (1989). *Contribution to the study of acoustics in closed rooms. Application to concert halls.* PhD. dissertation. Universitat Politécnica de Valencia. Valencia. Spain. pp.43–68.

Giménez, A., Sanchis, A. M., Sabater, A. S., Faus, J. R., Jordá, S. C. and Vanacloy, M. D. J. (2001). Estudio de la evolución de parámetros acústicos que miden la calidad de salas de conciertos. In: *Proceedings of the 32nd Congreso Nacional de Acústica "TecniAcustica".* Logroño, Spain. pp. 1–5.

González, A., Lacuesta, R. and Baldomà, M. (2013). *El Palacio Güell: Una obra maestra de Antoni Gaudí*. 2nd edition. Barcelona: Diputació de Barcelona, 317 p.

Granell, E. (2002). El Palau Güell de Antoni Gaudí en Barcelona: 1886–1888. *DC PAPERS, revista de crítica y teoría de la arquitectura*, No. 7, pp. 48–55.

Kircheri, A. (1673). *Phonurgia nova sive conjugium mechanico-physicum artis & naturae paranympha phonosophia concinnatum.* Rudolphum Dreherr. Kempten. Germany. pp.10–189.

Lahuerta, J. (1992). *Antonio Gaudí: Arquitectura, ideología y política*. Madrid: Electa. pp. 67–117.

León-Rodríguez, A. L. (1998). La acústica de los teatros a través de la historia. In: *Actas del Segundo Congreso Nacional de Historia de la Construcción, October 22–24, 1998, A Coruña, Spain*, pp. 263–271.

Marshall, L. G. (1994). An acoustics measurement program for evaluating auditoriums based on the early/late sound energy ratio. *The Journal of the Acoustical Society of America*, Vol. 96, Issue 4, pp. 2251–2261. DOI: 10.1121/1.410097.

Meyer, J. (1993). Sound of the orchestra. *Journal of the Audio Engineering Society*, Vol. 41, Issue 4, pp. 203–213.

Meyer, J. (2003). *Kirchenakustik*. Frankfurt am Main: Verlag Erwin Bochinsky.

Samper, A., González, G. and Herrera, B. (2017). Determination of the geometric shape which best fits an architectural arch within each of the conical curve types and hyperbolic-cosine curve types: the case of Palau Güell by Antoni Gaudí. *Journal of Cultural Heritage*, Vol. 25, pp. 56–64. DOI: 10.1016/j.culher.2016.11.015.

Segura, J., Giménez, A., Romero, J. and Cerdá, S. A. (2011). A comparison of different techniques for simulating and measuring acoustic parameters in a place of worship: Sant Jaume Basílica in Valencia, Spain. *Acta Acustica United with Acustica*, Vol. 97, No. 1, pp. 155–170. DOI: 10.3813/AAA.918396.

Sender, M., Planells, A., Perelló, R., Segura, J. and Giménez, A. (2018). Virtual acoustic reconstruction of a lost church:

application to an Order of Saint Jerome monastery in Alzira, Spain. *Journal of Building Performance Simulation*, Vol. 11, Issue 3, pp. 369–390. DOI: 10.1080/19401493.2017.1340975.

Suárez, R., Alonso, A. and Sendra, J. J. (2015). Intangible cultural heritage: The sound of the Romanesque Cathedral of Santiago de Compostela. *Journal of Cultural Heritage*, Vol. 16, Issue 2, pp. 239–243. DOI: 10.1016/j.culher.2014.05.008.

Tronchin, L. and Knight, D. J. (2016). Revisiting historic buildings through the senses visualising aural and obscured aspects of San Vitale, Ravenna. *International Journal of Historical Archaeology*, Vol. 20, Issue 1, pp. 127–145. DOI: 10.1007/s10761–015-0325–2.

Vorländer, M. (2007). *Auralization: Fundamentals of acoustics, modelling, simulation, algorithms and acoustic virtual reality*. Berlin: Springer, 365 p.

Vorländer, M., Schröder, D., Pelzer, S. and Wefers, F. (2015). Virtual reality for architectural acoustics. *Journal of Building Performance Simulation*, Vol. 8, Issue 1, pp. 15–25. DOI: 10.1080/19401493.2014.888594.

DOI: 10.23968/2500-0055-2021-6-2-31-36

PROBLEM OF THE ANISOTROPY OF ELASTICITY AND STRENGTH IN ANISOTROPIC FIBER MATERIALS

Vladimir Glukhikh

Saint Petersburg State University of Architecture and Civil Engineering
Vtoraja Krasnoarmeyskaya st., 4, Saint Petersburg, Russia

E-mail: tehmeh@spbgasu.ru

Abstract

Introduction: The paper presents new results of studies on the anisotropy of fiber materials with cylindrical anisotropy, which include filament-wound composite materials reinforced with various fibers. **Methods:** We suggest a mathematical solution to a fourth-order partial differential equation in polar coordinates with two variables for an orthotropic anisotropic body. To solve this equation, we converted it into Cartesian coordinates and presented the stress function as a sum of polynomials. **Results and Discussion:** As a result of the solution, we obtained two relationships between the elastic constants in the principal directions of anisotropy (so-called elasticity parameters). One of them was obtained for the first time, and the other results from the solution of the anisotropy problem for an orthotropic curved body, suggested by S. G. Lekhnitsky. The obtained solution does not contradict Lekhnitsky's solution. Thus, in our opinion, orthotropic materials can be divided into two groups. In one group, when shifting from the radial to the tangential direction, the elastic constants take on extreme values when the layers are at angles of 0, 60, and 90°. In the other group, there is no intermediate extreme value and the elastic constants take on extreme values when the layers are at angles of 0 and 90°. The obtained results can be applied in the development of new high-strength composite materials and new technologies for the design and manufacture of building structures, as well as in the design of high-strength structures from synthetic composite materials.

Keywords

Anisotropy of properties, composite materials, mathematical model, cylindrically anisotropic body, modulus of elasticity, principal stresses, elastic constants, Poisson's ratio, shear modulus.

Introduction

Filament-wound composites reinforced with fibers of carbon, boron or basalt, metallic or glass fibers, and wood as a natural composite material can be classified as anisotropic fiber materials with cylindrical anisotropy.

In nature, composite materials are formed in a natural way, and, according to the basic principles of bionics, their strongest fibers extend in the direction of principal stresses and strains.

By studying natural composite materials, material engineers design materials with pre-determined properties.

Fiber-glass products (including those made of filament-wound fiber-glass), similar to such a natural composite as wood with its annual rings, get widespread use. Wood, as well as fibers in bones of humans and animals, are often taken as prototypes when creating new advanced high-strength materials.

Such materials are anisotropic. Their physical and mechanical properties vary throughout the volume and in different directions, depending on the required performance of the material.

Many researchers in Russia (Ye. K. Ashkenazi, A. I. Kuznetsov, S. G. Lekhnitsky, A. N. Mitinsky, A. A. Pozdnyakov, A. L. Rabinovich, Yu. S. Sobolev, and others) and abroad (C. S. Grove, A. Jlinen, R. Keylwerth, H. Kubler, D. V. Rosato, and others) have been studying the anisotropy of elasticity and strength in anisotropic materials.

Based on the analysis of literature sources, we established that until recently there was no mathematical relationship found between the elastic constants in the principal directions of anisotropy (in contrast with isotropic bodies). According to some researchers (Ye. K. Ashkenazi, Yu. S. Sobolev, and others), this is one of the main reasons for obtaining conflicting experimental and theoretical results. This prompted new studies on elasticity and strength in anisotropic materials and, in particular, composite materials of natural and synthetic origin.

Over the last 15–20 years, new promising data were obtained for anisotropic materials. In most cases, the insights of 50–70 years ago are still used when conducting research or solving practical problems.

In this paper, we present the results of our

theoretical studies on the anisotropy of elasticity in filament-wound composite materials, based on the well-known laws of mathematics and mechanics, and compare those with the results obtained much earlier by Ye. K. Ashkenazi, S. G. Lekhnitsky, Yu. S. Sobolev, and others.

Methods

The following fourth-order homogeneous partial differential equation in polar coordinates for an orthotropic body, known in the theory of elasticity of an anisotropic body (Ashkenazi, 1978; Lekhnitsky, 1977) was taken as the basis for theoretical studies:

$$\frac{1}{E_t}\cdot\frac{\partial^4 F}{\partial r^4}+\left(\frac{1}{G_{rt}}-\frac{2\nu_{rt}}{E_r}\right)\cdot\frac{1}{r^2}\cdot\frac{\partial^4 F}{\partial r^2 d\theta^2}+\frac{1}{E_r}\cdot\frac{1}{r^4}\cdot\frac{\partial^4 F}{d\theta^4}+$$
$$\frac{2}{E_t}\cdot\frac{1}{r}\left(\frac{\partial^3 F}{\partial r^3}\right)-\left(\frac{1}{G_{rt}}-\frac{2\nu_{rt}}{E_r}\right)\cdot\frac{1}{r^3}\cdot\frac{\partial^3 F}{\partial r d\theta^2}- \quad (1)$$
$$-\frac{1}{E_r}\cdot\frac{1}{r^2}\cdot\frac{\partial^2 F}{\partial r^2}+\left(2\frac{1-\nu_{rt}}{E_r}+\frac{1}{E_{rt}}\right)\frac{1}{r_4}\cdot\frac{\partial^2 F}{d\theta^2}+\frac{1}{E_r}\cdot\frac{1}{r^3}\cdot\frac{\partial F}{\partial r}=0,$$

where E_r, E_t — the moduli of elasticity in tension (compression) in the principal directions;
ν_{rt}, G_{rt} — the Poisson's ratio and shear modulus of elasticity.

To solve the problem, Eq. (1) was converted into Cartesian coordinates, which is too cumbersome and, therefore, is not presented in the paper.

To solve Eq. (1) in the plane problem for a circular plate with cylindrical anisotropy, the stress function was taken as a sum of polynomials (Kurdyumov, 1946):

$$F=\sum_{i=1}^{n}x^k\cdot f_k(y), \quad (2)$$

where $f_k(y)$ — unknown functions satisfying differential Eq. (1).

Results

As a result of solving Eq. (1) with the substitution of the corresponding derivatives of stress function (2), after transformations, second-order algebraic Eq. (3) was obtained, the roots of which are as follows:

$$B^2-\frac{2}{3}\left(5+k^2\right)B-\frac{5}{3}k^4+\frac{14}{3}k^2+1=0; \quad (3)$$

$$B_{(1)}=3-k^2; \quad (4)$$

$$B_{(2)}=\frac{1+5k^2}{3}, \quad (5)$$

where $k^2=E_t/E_r$.

One of the roots (4) can be found in the monograph by S. G. Lekhnitsky (1957), solving the bending problem in an anisotropic curved bar (an orthotropic bar with cylindrical anisotropy), where Eq. 24.7 on page 98 is written as follows:

$$\frac{E_t}{E_r}\left(1-2\nu_{rt}\right)+\frac{E_t}{G_{rt}}=3. \quad (6)$$

By substituting the known relationships into Eq. (6), we obtain the same expression (4) for the first root, which does not contradict the relationship between the elastic constants, obtained by S. G. Lekhnitsky. However, we also obtained expression (5), which we could not find in any of the known publications. Thus, we can conveniently divide orthotropic anisotropic materials with cylindrical anisotropy into two groups. In the first group of materials satisfying condition (4), the modulus of elasticity changes from 0 to 90° (from the radial to the tangential direction) passing through an intermediate extremum point when the layers are at an angle of 30° to the force line.

In the second group, there is no intermediate extremum point and the modulus of elasticity changes from 0 to 90° smoothly.

This conclusion can be reached by analyzing the equations we obtained for the elastic constants:

$$\frac{1}{E_{x'}}=\frac{cos^4\theta}{E_r}+\frac{sin^4\theta}{E_t}+\frac{3-k^2}{E_t}sin^2\theta\cdot cos^2\theta;$$

$$\frac{1}{E_{y'}}=\frac{sin^4\theta}{E_r}+\frac{cos^4\theta}{E_t}+\frac{3-k^2}{E_t}sin^2\theta\cdot cos^2\theta;$$

$$\frac{1}{G_{x'y'}}=\frac{8\left(k^2-1\right)}{E_t}sin^2\theta\cdot cos^2\theta+\frac{1}{G_{rt}};$$

$$\frac{1}{\nu_{x'y'}}=-E_{x'}\left[\frac{2\left(k^2-1\right)}{E_t}sin^2\theta\cdot cos^2\theta-\frac{\nu_{rt}}{E_r}\right].$$

According to our solution, the coefficient β, irrespective of $k^2=E_t/E_r$, will be equal to 2 (as in the monograph by S. G. Lekhnitsky (1957)), i.e. it will be exactly the same as in an isotropic bar, and this does not contradict the conclusion drawn by S. G. Lekhnitsky:

$$\beta=\sqrt{1+\frac{a_{11}+2a_{12}+a_{66}}{a_{22}}}=\sqrt{1+\frac{E_t}{E_r}\left(1-2\nu_{rt}\right)+\frac{E_t}{G_{rt}}}.$$

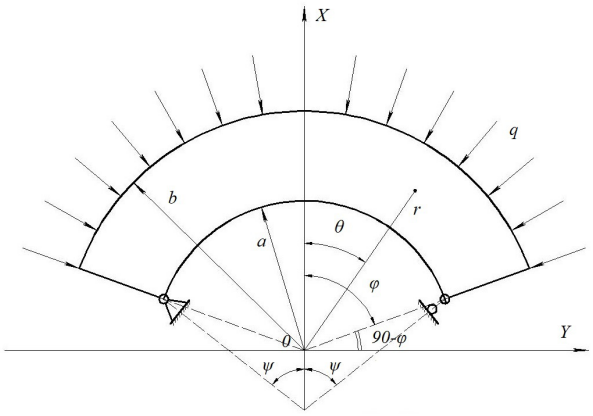

Then the stresses in an orthotropic cylindrically anisotropic curved bar can be calculated using the equations in Lekhnitsky's notations (1957):

$$\left.\begin{aligned}
&\sigma_r = \frac{q}{h}\left[P + Q\left(\frac{r}{b}\right)^{k-1} + R\left(\frac{b}{r}\right)^{k+1}\right] + \\
&+ \frac{q}{b\cdot h\cdot g_1}\cdot\frac{b}{r}\left[\left(\frac{r}{b}\right)^{\beta} + C^{\beta}\left(\frac{b}{r}\right)^{\beta} - \left(1+c^{\beta}\right)\right]\frac{\cos(\varphi-\psi)}{cos\psi}\cdot cos\theta, \\
&\sigma_t = \frac{q}{h}\left[P + Q\ k\left(\frac{r}{b}\right)^{k-1} - R\ k\left(\frac{b}{r}\right)^{k+1}\right] + \\
&+ \frac{q}{b\cdot h\cdot g_1}\cdot\frac{b}{r}\left[(1+\beta)\left(\frac{r}{b}\right)^{\beta} + (1-\beta)c^{\beta}\left(\frac{b}{r}\right)^{\beta}\right. \\
&\left. - \left(1+c^{\beta}\right)\right]\frac{\cos(\varphi-\psi)}{cos\psi}\cdot cos\theta, \\
&\tau_{rt} = \frac{q}{b\cdot h\cdot g_1}\cdot\frac{b}{r}\left[\left(\frac{r}{b}\right)^{\beta} + c^{\beta}\left(\frac{b}{r}\right)^{\beta} - \left(1+c^{\beta}\right)\right]\frac{\cos(\varphi-\psi)}{cos\psi}\cdot sin\theta, \\
&where\ P = \frac{1}{2\left(k^2-1\right)\left(1-c^{2k}\right)g}\ \text{x}
\end{aligned}\right\} \quad (7)$$

$$\left.\begin{aligned}
&\text{X}\left[\begin{matrix}2k(k-1)\left(1-c^{k+1}\right)+2k(k+1)c^{k+1}\left(1-c^{k-1}\right)- \\ \left(k^2-1\right)(1+c)\left(1-c^{2k}\right)m\end{matrix}\right]; \\
&Q = \frac{1}{2(k-1)\left(1-c^{2k}\right)g}\left[\begin{matrix}-(k-1)\left(1-c^2\right)-2kC^2\left(1-C^{k-1}\right) \\ +(k-1)(1+C)(1-C)m\end{matrix}\right]; \\
&\text{R} = \frac{1}{2(k+1)\left(1-c^{2k}\right)g}\text{X}; \\
&\text{X}\left[\begin{matrix}(k+1)c^{2k}\left(1-c^2\right)-2kc^{k+1}\left(1-c^{k+1}\right)-(k+1) \\ (1+c)c^{2k}\left(1-c^{1-k}\right)m\end{matrix}\right]; \\
&c = \frac{a}{b}; m = \frac{sin\varphi\ \ sin(\varphi-\psi)}{cos\psi},
\end{aligned}\right\} \quad (8)$$

where

$$k = \sqrt{\frac{E_t}{E_r}}; g = \frac{1-c^2}{2} - \frac{k}{k+1}\cdot\frac{\left(1-c^{k+1}\right)^2}{1-c^{2k}} + \frac{k\cdot c^2}{k-1}\cdot\frac{\left(1-c^{k-1}\right)^2}{1-c^{2k}};$$

$$g_1 = \frac{2}{\beta}\left(1-c^{\beta}\right) + \left(1+c^{\beta}\right)lnC.$$

During calculations for the second group of anisotropic materials by Eqs. (7) and (8), we should note that the coefficient β depends on k^2, in contrast with the first case: this follows from Eq. 24.7 (Lekhnitsky, 1957) and the second root of algebraic Eq. (3).

$$B = \frac{1+5k^2}{3}, \text{ i.e.}$$

$$\beta = \sqrt{1+\frac{E_t}{E_r}\left(1-2v_r\right)+\frac{E_t}{G_{rt}}} = \sqrt{1+k^2+\frac{1+5k^2}{3}} == 2\sqrt{\frac{1+2k^2}{3}}.$$

The equations to calculate the elastic constants at the second root will take the following form:

$$\frac{1}{E_{x'}} = \frac{cos^4\theta}{E_r} + \frac{1+5k^2}{3}sin^2\theta\cdot cos^2\theta + \frac{sin^4\theta}{E_t};$$

$$\frac{1}{E_{y'}} = \frac{sin^4\theta}{E_r} + \frac{1+5k^2}{3}sin^2\theta\cdot cos^2\theta + \frac{cos^4\theta}{E_r};$$

$$\frac{1}{G_{x'y'}} = \frac{8\left(1-k^2\right)}{3E_t}sin^2\theta\cdot cos^2\theta + \frac{1}{G_{rt}};$$

$$\frac{1}{v_{x'y'}} = -E_{x'}\left[\frac{2\left(1-k^2\right)}{3E_t}sin^2\theta\cdot cos^2\theta - \frac{v_{rt}}{E_r}\right].$$

The ratios of the elastic constants (conventionally called the elasticity parameter) depend on the degree of accuracy in determining each of the constants. The Poisson's ratio is rather small. Besides, the authors of methods for its determination (Ye. K. Ashkenazi, A. N. Mitinsky, Yu. S. Sobolev) acknowledge that when the composite layers are at an angle of 45°, there is an inaccuracy in the determination.

The obtained values of the anisotropy parameters make it possible to eliminate this drawback and facilitate the solution of differential Eq. (1).

Therefore, the calculation of stresses for orthotropic anisotropic bodies with cylindrical anisotropy, performed according to Eqs. (7) and (8) with the use of the coefficient $\beta = 2$ in one case and $\beta = 2\sqrt{\frac{1+2k^2}{3}}$ in the other case, depends on the ratio between the moduli of elasticity $E_t / E_r = k^2$ for a particular anisotropic material.

In this case, it will be necessary to determine in advance which group the anisotropic material belongs to.

Discussion. Extrema of elasticity characteristics

The extremum properties and the position of the principal anisotropy planes are of the most interest when studying the physical and mechanical properties of anisotropic materials, including composite materials of natural and synthetic origin.

The analytical dependence of the modulus of elasticity is known from the theory of elasticity:

$$\frac{1}{E_{x'}} = \frac{cos^4\theta}{E_x} + \frac{sin^4\theta}{E_y} + \left(\frac{4}{E_{xy}^{(45)}} - \frac{1}{E_x} - \frac{1}{E_y}\right)sin^2\theta\cdot cos^2\theta. \quad (9)$$

With the introduction of the following notations:

$$E_x = E_0; E_y = E_{90}; E_{xy}^{(45)} = E_{45}; E_{x'} = E_{\alpha};$$

$$G_{xy} = G_0; G_{xy}^{(45)} = G_{45}; G_{x'y'} = G_{\alpha};\ \mu_{xy} = \mu_0;$$

$$\mu_{yx} = \mu_{90}; C = \frac{E_0}{E_{90}}; b = \frac{E_0}{E_{45}} - \frac{1+C}{4}.$$

Ye. K. Ashkenazi obtained the following instead of Eq. (9):

$$\frac{E_\alpha}{E_0}=\frac{1}{cos^4\theta+b\cdot sin^2 2\theta+C\cdot sin^2\theta}\ .$$

This equation can be applied to any plane of elastic symmetry.

The equation suggested by A. N. Mitinsky (1948) for an orthotropic body in his notations has the following form:

$$G_{xy}=\frac{E_{xy}^{(45)}}{2\left(1+\mu_{xy}^{(45)}\right)}\ .$$

This equation is similar to the equation for isotropic materials:

$$G_{xy}^{(45)}=G_{45}=\frac{E_0\cdot E_{90}}{E_0\left(1+\mu_{90}\right)+E_{90}\left(1+\mu_0\right)}.$$

By equating the first derivative $\frac{dE_\alpha}{d\alpha}$ to zero, Ye. K. Ashkenazi obtained the following:

$$\left[cos^2\alpha-Csin^2\alpha-2b\left(1-2sin^2\alpha\right)\right]sin\alpha\cdot cos\alpha=0\ .$$

The first two extrema can be found by equating the factor outside the brackets to zero. Thus, we get the following:

$$\alpha_1=0°;\ \alpha_2=90°.$$

The third extremum of the modulus of elasticity will be achieved at the following angle:

$$\alpha_3=arcsin\sqrt{\frac{1-2b}{1+C-4b}};$$

or with account for substitution 2.31 (Ashkenazi and Ganov, 1981):

$$\alpha_3=arcsin\sqrt{\frac{1-2\frac{E_0}{E_{45}}+\frac{1+\frac{E_0}{E_{90}}}{2}}{1+\frac{E_0}{E_{90}}-4\frac{E_0}{E_{45}}+\left(1+\frac{E_0}{E_{90}}\right)}}.$$

For an equally reinforced material (at C = 1), e.g. plywood, α_3 = 45°.

The third extremum will be achieved only subject to the following inequality (Ashkenazi and Ganov, 1981):

$$1\geq\frac{1-2b}{1+C-4b}\geq 0.$$

If this condition is not met, the modulus of elasticity will have only two extrema, as, for instance, in filament-wound fiber-glass or natural wood in the plane of the greatest stiffness (in the direction of the fibers).

The modulus of elasticity *Ex'* of an orthotropic anisotropic material in an arbitrary direction can be determined by expression 2.28 from the monograph by Ye. K. Ashkenazi (1978).

For an arbitrary direction of the *X'* axis, with account for the known ratio between the direction cosines:

$$n_1^2+l_1^2+m_1^2=1.$$

Ye. K. Ashkenazi obtained the values of the direction cosines:

1) at n_1 = 0;

$$m_1=\pm\sqrt{\frac{\frac{3}{E_y}-\frac{4}{E_{yz}^{(45)}}+\frac{1}{E_z}}{\frac{4}{E_y}+\frac{4}{E_z}-\frac{8}{E_{yz}^{(45)}}}};\ l_1=\pm\sqrt{(1-m_1^2)};$$

2) at m_1 = 0;

$$n_1=\pm\sqrt{\frac{\frac{3}{E_y}+\frac{1}{E_x}-\frac{4}{E_{xy}^{(45)}}}{\frac{4}{E_y}+\frac{4}{E_x}-\frac{8}{E_{xy}^{(45)}}}};\ l_1=\pm\sqrt{(1-n_1^2)};$$

3) at l_1 = 0;

$$n_1=\pm\sqrt{\frac{\frac{4}{E_z}-2A}{\frac{4}{E_x}+\frac{4}{E_z}-4A}};\ m_1=\pm\sqrt{1-n_1^2},$$

where $A=\frac{4}{E_{xz}^{(45)}}-\frac{1}{E_x}-\frac{1}{E_z}$. In particular cases: m_1 = 0; l_1 = 0; n_1 = ± 1 l_1 = 0; n_1 = 0; m_1 = ±n_1 = 0; m_1 = 0; l_1 = ± 1.

Our solution (Gluhih et al., 2016) coincides with this one.

Conclusions

1) The found mathematical relationship between the elastic constants in the principal directions of anisotropy simplifies the solution of elastic problems for elastic fiber composite materials.

2) Experimental determination of elastic constants can be streamlined.

3) Using the suggested solution, with account for the tensorial nature of elasticity and strength characteristics, it will be possible to study the strength of composite materials considering the angle of the reinforcing fibers.

References

Aksenov, A. A. and Malyukov, S. V. (2014). Hardness and deformation of particle board at negative temperatures. *Forestry Engineering Journal*, Vol. 4, No. 3 (15), pp. 184–192. DOI: 10.12737/6286.

Aksenov, A. A. and Malyukov, S. V. (2015). Influence of negative temperatures and degrees of hardness seals compressed wood. *Fundamental Research,* Issue 5 (Part 1), pp. 9–13.

Ashkenazi, Ye.K. (1978). *Anisotropy of wood and wood materials.* Moscow: Lesnaya Promyshlennost, 224 p.

Ashkenazi, Ye.K. and Ganov, V.V. (1981). *Anisotropy of structural materials. Reference book.* Moscow: Lesnaya Promyshlennost, 320 p.

Gluhih, V. N., Petrov, V. M. and Sojtu, N. J. (2016). Determination of elasticity constants with anisotropy of properties of composite materials used for winding the responsible shell and beam structures in shipbuilding and port infrastructure. *Vestnik Gosudarstvennogo Universiteta Morskogo i Rechnogo Flota Imeni Admirala S. O. Makarova*, Issue 2 (36), pp. 137–142. DOI: 0.21821/2309–5180-2016–8-2–137-142.

Glukhikh, V. N., Prilutskiy, A. A. and Akopyan, A. L. (2016). The use of some natural materials in the development of composites for the building industry. *Fundamental Research,* Issue 3 (Part 2), pp. 235–239.

Kuo, S.-R. and Yau, J. D. (2012). Buckling equations of orthotropic thin plates. *Journal of Mechanics,* Vol. 28, Issue 3, pp. 555–567. DOI: 10.1017/jmech.2012.64.

Kurdyumov, N. (1946). Polynomial solution of a plane elasticity problem. *Journal of Applied Mathematics and Mechanics,* Vol. 11.

Lekhnitsky, S. G. (1957). *Anisotropic plates.* 2nd edition. Moscow: Gostekhizdat, 463 p.

Lekhnitsky, S. G. (1977). *Theory of anisotropic body elasticity.* 2nd edition. Moscow: Nauka, Main Editorial Office for Literature on Physics and Mathematics, 416 p.

Mitinsky, A. N. (1948). Elastic constants of wood as an orthotropic material. *Trudy LTA*, No. 63, pp. 23–54.

Okhovat, R. and Boström, A. (2018). Dynamic equations for an orthotropic cylindrical shell. *Composite Structures,* Vol. 184, pp. 1197–1203. DOI: 10.1016/j.compstruct.2017.10.034.

Pardayev, A. S. (2008). *Ensuring shape stability in non-homogeneous solid wood with account for the cylindrical anisotropy of its elements during shrinkage and swelling.* Author's Abstract of PhD Thesis in Engineering. Minsk: Belarusian State Technical University.

Pardayev, A. S. (2011). Structural models of mechanical anisotropy of wood and their application in CAE systems. *Proceedings of BSTU*, No. 2 (140), pp. 161–163.

Potapov, A. I. (2015). Nondestructive control of elasticity modulus anisotropy of composite materials in the products. *Journal of Mining Institute*, Vol. 216, pp. 97–103.

Rosato, D. V. and Grove, C. S. (1969). *Filament winding.* Moscow: Mashinostroyeniye, 310 p.

Rotter, J. M. and Sadowski, A. J. (2012). Cylindrical shell bending theory for orthotropic shells under general axisymmetric pressure distributions. *Engineering Structures,* Vol. 42, pp. 258–265. DOI: 10.1016/j.engstruct.2012.04.024.

Vinnik, N. I. (1980). *Modified wood.* Moscow: Lesnaya Promyshlennost, 159 p.

ЗАДАЧА АНИЗОТРОПИИ УПРУГОСТИ И ПРОЧНОСТИ ВОЛОКНИСТЫХ АНИЗОТРОПНЫХ МАТЕРИАЛОВ

Владимир Николаевич Глухих

Санкт-Петербургский государственный архитектурно-строительный университет
2-ая Красноармейская ул., 4, Санкт-Петербург, Россия

E-mail: tehmeh@spbgasu.ru

Аннотация
В статье приведены новые материалы исследований анизотропии волокнистых материалов с цилиндрической анизотропией, к которым относятся армированные различными волокнами намоточные композиционные материалы. **Методы:** Автор дает математическое решение дифференциального уравнения четвёртого порядка в частных производных с двумя переменными для анизотропного ортотропного тела в полярных координатах. Для решения этого уравнения перевели в декартовы координаты и использовали функцию напряжений в виде суммы полиномов. **Результаты и обсуждения:** В итоге решения были получены два соотношения между постоянными упругости в главных направлениях анизотропии — так называемые параметры упругости. Одно из них получено впервые, а второе вытекает из решения задачи анизотропии криволинейного ортотропного тела С. Г. Лехницким, и полученное решение ему не противоречит. Таким образом, автор считает, что ортотропные материалы могут быть разделены на две группы. В одной группе, при переходе от радиального направления к тангенциальному, постоянные упругости принимают экстремальные значения при расположении слоёв под углами 0°, 60° и 90°. В другой, промежуточное экстремальное значение отсутствует, и постоянные упругости принимают экстремальные значения при наклоне слоёв под углами 0° и 90°. Результаты исследований представляют интерес при разработке новых высокопрочных композиционных материалов, при разработке новых технологий проектирования и изготовления строительных конструкций, высокопрочных конструкций из синтетических композиционных материалов.

Ключевые слова
Анизотропия свойств, композиционные материалы, математическая модель, цилиндрически анизотропное тело, модуль упругости, главные напряжения, постоянные упругости, коэффициент Пуассона, модуль сдвига.

DOI: 10.23968/2500-0055-2021-6-2-37-44

INVESTIGATING THE CORROSION INITIATION PROCESS IN REINFORCED CONCRETE STRUCTURES UNDER THE IMPACT OF CLIMATE CHANGE

Tran Ngoc-Long[1], Phan Van-Phuc[1]*, Valeriy Morozov[2]

[1]Department of Civil Engineering, Vinh University
182-Le Duan Street, Vinh, Vietnam
[2]Saint Petersburg State University of Architecture and Civil Engineering
Vtoraja Krasnoarmeyskaya st., 4, Saint Petersburg, Russia

*Corresponding author: vanphuckxd@vinhuni.edu.vn

Abstract

Introduction: Climate change (temperature rise and sea level rise) has a considerable influence on the behavior of concrete structures over time. All concrete degradation processes are connected to climate variables and the effects of climate change. The RCP8.5 (Representative Concentration Pathway) scenario, which is part of the report on climate change and level rise scenarios for Vietnam, predicts that the beginning of the 21st century will see an average annual increase in temperature between 0.8 and 1.1°C. In the mid-21st century, the temperature will likely increase by 1.8–2.3°C, with the temperature in the north likely increasing by 2.0–2.3°C and in the south by 1.8–1.9°C. In marine environments, the degradation of concrete structures can occur rapidly due to chloride-induced reinforcement corrosion. Furthermore, sea level rise is going to reduce the distance from the coastline to the structures and lead to increased surface chloride concentration. **Methods:** The evaluation of chloride penetration was based on the ASTM C1202 test (ASTM, 2012). The cylinder specimens (d = 100 mm, h = 200 mm) used for a rapid chloride penetration test (RCPT) were immersed in water for 28 days in a water-curing tank. **Results:** This study proposes a predictive model for analyzing the impact of climate change on the service life of concrete structures on Vietnam's North Central Coast. The corrosion initiation time decreases by 16.5% when the effects of both temperature rise and sea level rise are taken into consideration. When only temperature rise is taken into consideration, the rate of reduction is approximately 9.0%. These results reaffirm that climate change has a significant effect on the corrosion initiation time of concrete structures located in a marine environment.

Keywords

Climate change, temperature rise, sea level rise, reinforced concrete structures, chloride penetration.

Introduction

The study of the durability of concrete under environmental conditions plays a fundamental role in evaluating the degradation processes that occur in concrete structures over time. Most concrete degradation processes are connected to climate variables and the effects of climate change. Global studies have considered the negative impact of climate change on new and existing infrastructure (Andrade and Castillo, 2003; Saha and Eckelman, 2014; Stewart et al., 2011, 2012; Talukdar and Banthia, 2013). Increasing temperature and rising seawater levels are both climate change-related phenomena that can impact the durability of concrete structures (Medeiros-Junior, 2018; Pijaudier-Cabot et al., 2004).

Reinforcement corrosion is directly related to the durability of concrete structures. Reinforcement corrosion induced by the ingress of chlorides leads to a reduction in the durability and serviceability of the structure (Bastidas-Arteaga et al., 2010; Stewart et al., 2011, 2012). Thus, it is important to design structures that ensure durability and consider the effects of climate change. Studies have analyzed the effect of climate change on chloride penetration and the process of concrete structure degradation. Stewart et al. (2012) analyzed the impact of climate change on corrosion and damage to concrete. According to the scenarios evaluated in the study, by 2100, the probability of corrosion will increase by 6–15%. Bastidas-Arteaga et al. (2010) studied the influence of global warming on the degradation of concrete structures in a marine environment. Their findings showed that global warming can reduce the service life of structures located 3.0 km away from the coastline by 6–14 years. Medeiros-Junior et al. (2015) proposed a model to illustrate the effect of climate change on the service life of concrete structures, taking into account the effects of temperature and relative humidity on the chloride diffusion coefficients. They analyzed chloride penetration prediction models for three different scenarios. The results showed that changes in temperature and relative humidity, identified for a period of 100 years, were responsible for reducing

service life by 7.8 to 10.2 years. Heede et al. (2014) showed the effect of global warming on chloride diffusivity. In untracked conditions, concrete that uses fly ash and silica fume is characterized by a very low chloride migration coefficient after 28 days (3.4×10–12 m2/s), which highly contributes to the material's estimated long service life (>100 years). Saha and Eckelman (2014) investigated the impact of corrosion on concrete structures, caused by increases in carbonation and chloride permeability. High and low emission scenarios were used for modeling carbonation and chloride-induced corrosion of concrete structures in the northeast United States.

In the sea level rise scenario, the distance between the coast and the structure decreases, while the concentration of chloride on the surface increases. Consequently, chloride penetration and corrosion increase as well (Ranasinghe et al., 2012). Gao and Wang (2017) proposed a probabilistic model for analyzing the effects of global warming and sea level rise on the service life of coastal concrete structures. Their analysis showed that climate change has a significant impact on the service life of concrete. Knott et al. (2017) presented the effects of rising groundwater, caused by sea level rise, on the service life of pavements in the coastal road infrastructure. The results indicated that service life reduction depended on the current depth to groundwater, the pavement structure, and the subgrade. This study will allow pavement engineers to effectively approach coastal road adaptation projects and significantly reduce costs. Wang et al. (2018) presented a numerical method to analyze the service life of cracked concrete, taking into account global warming and sea level rise. The effect of sea level rise on surface chloride concentration was described by applying the Bruun rule. The analysis showed that the initial service life of 50.0 years is reduced by about 6.0% when temperature rise and sea level rise are taken into account.

According to ACI 365 (Clifton, 2000; L'Hostis et al., 2011; Pijaudier-Cabot et al., 2004), service life consists of the corrosion initiation time and the corrosion propagation time. The corrosion initiation time is defined as the time it takes the chloride content at the steel rebar surface to reach critical level. The corrosion propagation time is defined as the time it takes the steel corrosion degree to exceed the critical steel corrosion (i.e., the corrosion at the concrete surface cracking point). Service life is limited to the corrosion initiation time, which equals the time it takes the aggressive substance to reach the reinforcement and induce passivation (DuraCrete, 2000). Therefore, it is necessary to predict the corrosion initiation time in order to assess the service life of structures in a marine environment. In Vietnam, some studies have also attempted to predict the corrosion initiation time of a reinforced concrete structure under the effects of the environment (carbon dioxide, chlorides, and seawater) and the combined mechanical load of environmental factors (ADB, 2013; Hanh and Furukawa, 2007; Tran et al., 2018). This study will review the influence of climate change on the penetration of chloride ions into concrete structures in a marine environment by including temperature rise and sea level rise into existing models to predict the corrosion initiation time of chloride-exposed concrete. The result will become the basis of designs for enhancing the durability of concrete structures in marine environments.

Temperature Rise and Sea Level Rise Scenario in Vietnam

The RCP8.5 (Representative Concentration Pathway) scenario, which is part of the report on climate change and level rise scenarios for Vietnam (ADB, 2013; Hanh and Furukawa, 2007; Thao et al., 2014; Thuc et al., 2016), predicts that the beginning of the 21st century will see an average annual increase in temperature between 0.8 and 1.1°C. In the mid-21st century, the temperature will likely increase by 1.8–2.3°C, with the temperature in the north likely increasing by 2.0–2.3°C and in the south by 1.8–1.9°C. At the end of the century, the temperature will likely increase by 3.3–4.0°C in the north and by

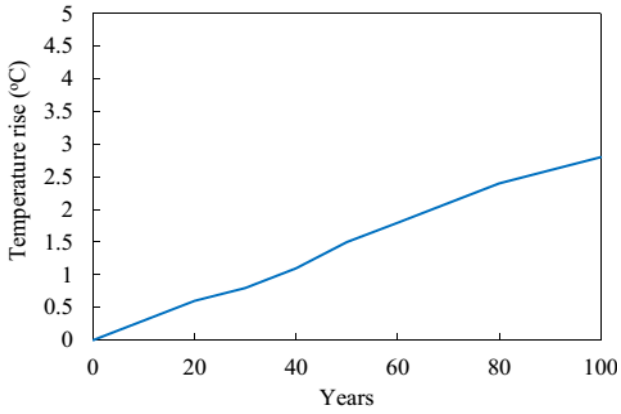

Figure 1. Temperature rise under RCP8.5

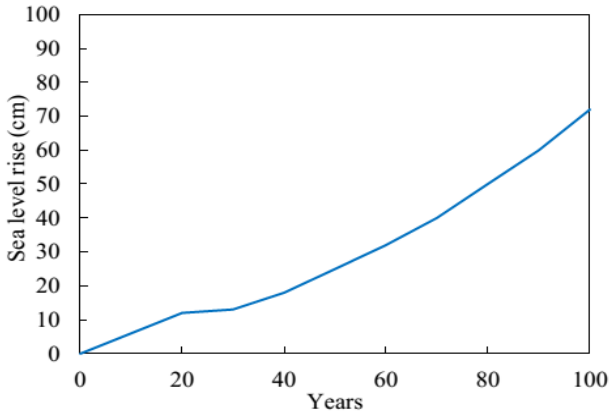

Figure 2. Sea level rise under RCP8.5

3.0–3.5°C in the south.

Under the RCP8.5 (Thuc et al., 2016) scenario, by the mid-21st century, the average sea level rise for the coastal areas of Vietnam would reach about 25 cm (from 17cm to 35 cm), and by the late 21st century, the average sea level rise for the coastal areas of Vietnam would be about 73 cm (from 49cm to 103 cm).

The North Central Coast of Vietnam is considered to be an area of extreme climatic impact, and in recent years it has been heavily affected by climate change (ADB, 2013; Hanh and Furukawa, 2007). Under the RCP8.5 scenario, the air temperature would increase by about 2.8°C due to global warming and the sea level would rise by about 72 cm over the next 100 years.

Methods

Chlorine ions intrude into the concrete parts of reinforced concrete structures in marine environments and accumulate on the reinforcement surface. When the chloride ion concentration on the reinforcement surface reaches the critical threshold, it begins to corrode the rebar. Chloride can enter concrete by many different mechanisms, such as diffusion, convection, and permeability. The chloride diffusion process occurs due to different concentration gradients. The model (Gjørv, 2011) for evaluating the service life of concrete structures was developed from the equation that calculates the the concentration of chloride on the rebar surface, based on Fick's second law, as follows:

$$C(x,t) = C_s\left(1 - erf\left(\frac{x}{2\sqrt{Dt}}\right)\right), \quad (1)$$

where $C(x, t)$ is the chloride concentration at depth x of the concrete cover (% of concrete weight); C_S is the chloride concentration on the surface (% of concrete weight); D is the chloride diffusion coefficient of concrete (10–12 m^2/s); t is the considered time (years); and *erf* is the error function.

The chloride diffusion coefficient decreases over time and is determined as an exponential function of time, as follows:

$$D(t) = D_{28}\left(\frac{t_o}{t}\right)^m, \quad (2)$$

where t_o is the age of experimental concrete with chloride ion permeability; t_o = 28 days = 0.0767 years; m is the factor related to further hydration of the binder and enhanced chloride binding capacity during exposure periods; m = 0.2 (Thomas and Bentz, 2002); and D_{28} is the chloride diffusion coefficient of concrete at the age of 28 days, as determined from the experiment.

In the 21st-century climate change scenario, the environmental temperature on the North Central Coast of Vietnam will rise by about 2.8°C due to global warming (Fig. 1), and the sea level will rise by about 72 cm over the next 100 years (Fig. 2).

The Life365 Model (Service Life Prediction Model of Steel-Reinforced Concrete) proposes the dependence of the chloride diffusion coefficient on temperature, which can be described as follows:

$$D(T) = D_{28}.\exp\left(\beta\left(\frac{1}{T_0} - \frac{1}{T}\right)\right), \quad (3)$$

where β is the activity energy of chloride diffusion (β = 4300); T_0 (298°K) is the reference temperature; and T (°K) is the average temperature at the construction site.

Concrete structures can be placed under different exposure conditions in different marine zones, such as the marine splash zone, the marine spray zone, and the marine atmosphere zone. In this study, we examine concrete structures placed in the marine atmosphere zone, where the chloride surface concentration is related to the distance from the coastline to the structure, d (km). Vu and Stewart (2000) proposed that the chloride surface concentration, C_S (kg Cl-/m^3), can be determined as follows:

C_S(d) = 2.95 kg Cl-/m3 concrete,
when d ≤ 0.1 km; (4)

C_S(d) = 1.15 – 1.81×log10(d) kg Cl-/m3 concrete,
when 0.1 km < d ≤ 2.84 km; (5)

C_S(d) = 0.03 kg Cl-/m3 concrete,
when d > 2.84 km; (6)

when sea level rise is considered, the distance from the coastline to the structure decreases, leading to increased surface chloride concentration. According to Bruun's (Pijaudier-Cabot et al., 2004) equation, when sea level rise is $S(t)$, and the average slope along the overall coastline is i_d (i_d = 0.5–1.5%), then the distance from the coastline to the structure will be reduced to:

$$\Delta d = \frac{S(t)}{i_d}. \quad (7)$$

At this time, if we account for sea level rise, the distance from the coastline to the structure will reach:

$$d' = d - \Delta d = d - \frac{S(t)}{i_d}. \quad (8)$$

The corrosion initiation time (t) is based on the time it takes the chloride concentration on the reinforcement surface to reach the corrosion threshold. As proposed by Kwon et al. (2009) and Life 365 (Bentz and Thomas, 2001; Gjørv, 2011; Thomas and Bentz, 2002), the chloride content in concrete (1.2 kg/m3 corresponding to 0.05% of concrete mass) is the reinforcement corrosion threshold (C_{cr}).

Corrosion occurs when $C(x,t) = C_{cr}$ at the time when $x = h$ (the thickness of the concrete cover), with the average surface chloride concentration (C_S).

The reinforcement corrosion initiation time due to chloride penetration can be rewritten based on Eq. (1) as follows:

$$t_i = \left[\frac{h^2}{4.D.t_o^m.\left(erf^{-1}\left(1-\frac{C_{cr}}{C_S}\right)\right)^2} \right]^{\frac{1}{1-m}}, \quad (9)$$

where erf^{-1} is the inversion of the error function.

Mixture Materials and Composition

This study used PC40 But Son cement, which has a specific gravity of 3.1 g/cm^3 and conforms with ASTM C150. We used natural sand with a maximum size of 4.75 mm as the fine aggregate, and crushed stone with a maximum size of 19 mm as the coarse aggregate. The aggregate grading was compliant with the ASTM C33 limits (ATSM, 2013). The specific gravity, bulk density (unit weight) in a compacted state, and water absorption of the coarse aggregate equaled 2.72 g/cm^3, 1.62 g/cm^3, and 0.52%, respectively. For the fine aggregate, these values were 2.68 g/cm^3, 1.71 g/cm3, and 0.9%, respectively. We investigated two normal-strength concrete types, C1 and C2, which are commonly used in construction (Table 1). Concrete C1 is usually used for substructures, while concrete C2 is mostly used for main bearing structures. The concrete mix was designed in line with ACI 211.1 (Dixon, 1991). The composition of each concrete type is shown in Table 1.

Table 1. Mixture composition for 1m^3 of concrete

Materials	Concrete C1	Concrete C2
Cement, kg	385	448
Sand, kg	811	759
Coarse aggregate, kg	1076	1076
Water, kg	170	170
Superplasticizer, l	3.46	4.03
Water/cement	0.46	0.38
Compressive strength, MPa	38.8	51.4

Results

Testing the Chloride Penetration Resistance of Concrete

The evaluation of chloride penetration was based on the ASTM C1202 test (ASTM, 2012). The cylinder specimens (d = 100 mm, h = 200 mm) used for our rapid chloride penetration test (RCPT) were immersed in water for 28 days in a water-curing tank, which was placed in a temperature room. Before the RCPT test, the cylinder was cut to a height of 50 mm. The resulting discs were sealed with two epoxy resin coats to ensure one-dimensional chloride flow through the discs. We saturated the specimens by placing them in a vacuum container and ensuring that the two end surfaces were exposed. The pressure was decreased below 1 mmHg. We maintained vacuum for four hours, before allowing air to be introduced. Then, water was introduced into the container to immerse the specimen for 18±2 hours before it was taken out and placed in the test setup.

The specimens were then placed in the testing cells. The testing process included monitoring the amount of electrical current passing through the specimen when a potential difference of 60V DC was maintained across the specimen for a period of 6 hours. In this test, chloride ions were forced to migrate out of the NaCl solution by being subjected to a negative charge; they passed through the concrete into a NaOH solution maintained at a positive potential. The results of testing the chloride permeability of two concrete types are shown in Table 2.

Berke and Hicks reported a correlation between the chloride diffusion coefficient and the chloride permeability of normal concrete (Bentz and Thomas, 2001). The following equation links the effective chloride diffusion coefficient with concrete permeability:

$$D = 0.0103\times(\text{coulombs})\ 0.84\ (10–12\ m^2/s). \quad (10)$$

Table 2 recapitulates the RCP values and the chloride diffusion coefficients (*D*) for two concrete types, C1 and C2. The chloride permeability of concrete C1 and C2 is “moderate” according to ASTM C1202.

Table 2. Chloride ion permeability and chloride diffusion coefficients for two concrete types

No.	Rapid chloride permeability, RCP (coulombs)		Chloride diffusion coefficient, 10–12 m2/s	
	Concrete C1	Concrete C2	Concrete C1	Concrete C2
1	3180	2234	9.01E-12	6.70E-12
2	3101	2290	8.82E-12	6.84E-12
3	3095	2259	8.81E-12	6.76E-12
Average	3125	2261	8.88E-12	6.77E-12

We carried out parametric studies to demonstrate the effects of temperature rise and sea level rise on the corrosion initiation time. Two types of concrete, C1 and C2, have the ratio of w/c = 0.46 and 0.38, respectively. The thickness of the concrete cover is 20–70 mm (according to Loreto, 2019) for reinforced concrete structures in marine environments). The exposure area has the marine atmosphere zone conditions. In this zone, the distance from the coastline to the structure is 300 m, the coastal slope is 1%, and the initial temperature is 25°C.

To evaluate the impact of climate change on the corrosion initiation time, caused by temperature rise and sea level rise, we ran tests for three case scenarios: no climate change (case 1), temperature rise (case 2), and both temperature rise and sea level rise (case 3). The corrosion initiation time is calculated and illustrated in Figs. 3 and 4, for all equations above and for structures using concrete C1 and C2. In cases 2 and 3, the corrosion initiation time is lower than in case 1. When considering the impact of sea level rise, the decrease in the corrosion initiation time is even more pronounced. When the w/c ratio decreases, the corrosion initiation time increases. When the thickness of the concrete cover increases, the corrosion initiation time also increases. Therefore, sea level rise has a significant impact on corrosion initiation time.

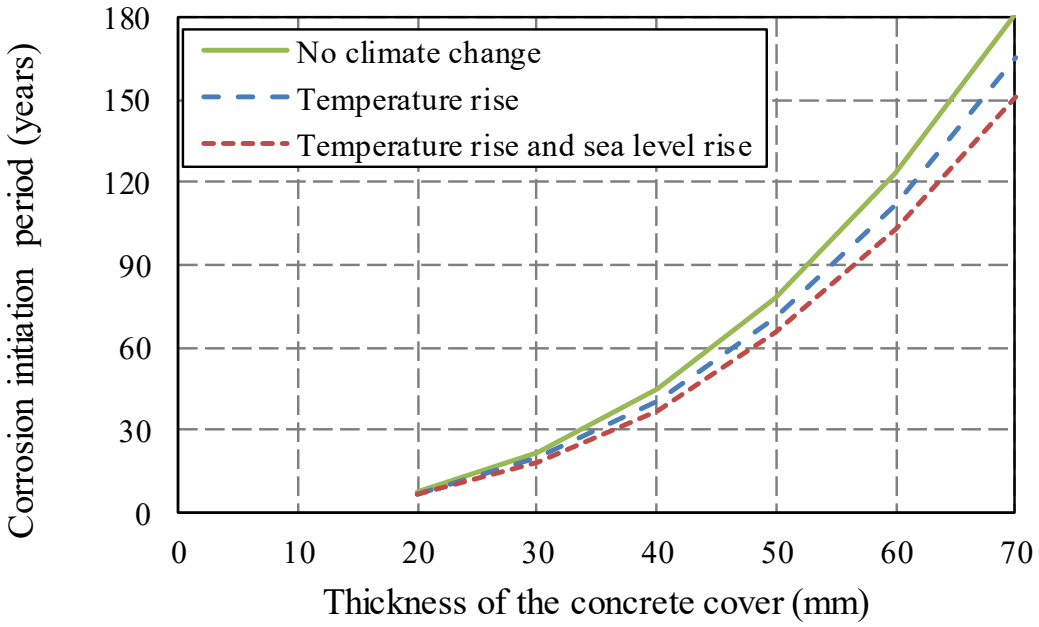

Figure 3. Corrosion initiation time for a structure with concrete C1

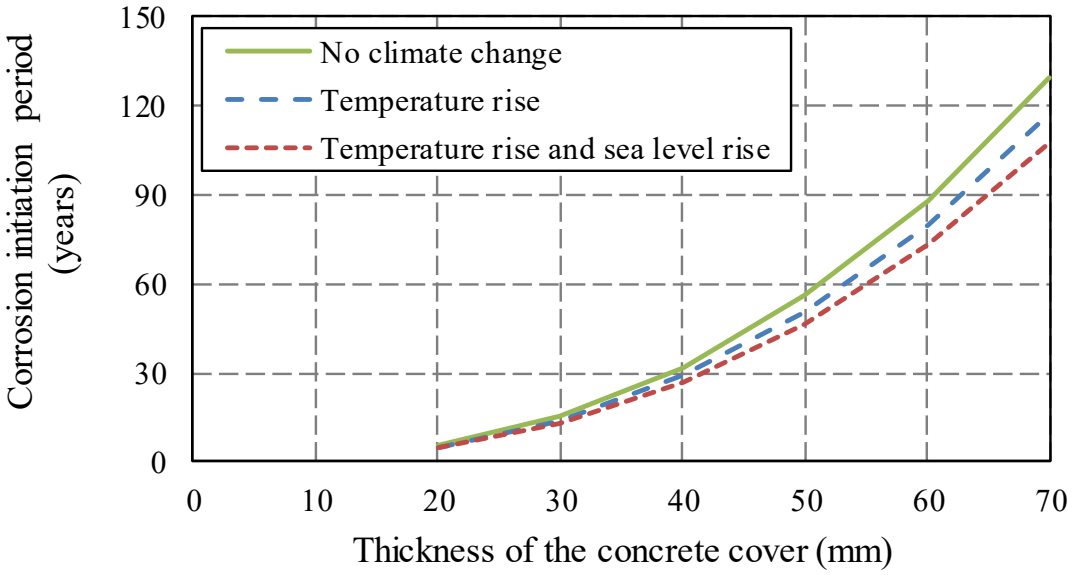

Figure 4. Corrosion initiation time for a structure with concrete C2

Table 3. Corrosion initiation time

Type	Thickness of the concrete cover (mm)	Corrosion initiation time (years)		
		No climate change	Temperature rise	Temperature rise and sea level rise
C1	30	15.5	14.1	13.0
	40	31.9	29.0	26.6
	50	55.7	50.7	46.5
C2	30	21.8	19.8	18.2
	40	44.8	40.7	37.4
	50	78.2	71.2	65.3

Table 3 shows the results of predicting the corrosion initiation time of reinforced concrete structures. According to TCVN 9346–2012 (Loreto, 2019), the standards for reinforced concrete structures in the marine atmosphere zone (where the distance from the coastline to the structure is about 0 to 1 km) are as follows. The minimum required cover thickness usually ranges from 30 to 50 mm, depending on the type of concrete, to achieve a service life of up to 50 years. When the thickness of the concrete cover is 50 mm, the corrosion initiation time of concrete C1 (w/c = 0.46) and concrete C2 (w/c = 0.38) is 55.7 years and 78.2 years, respectively, in the case of no climate change. With adjustments for temperature rise, the corrosion initiation time of concrete C1 and C2 decreases to 50.7 years and 71.2 years, respectively (the reduction ratio is about 9.0%). With adjustments for both temperature rise and sea level rise, the corrosion initiation time of concrete C1 and C2 decreases to 46.5 years and 65.3 years, respectively (the reduction ratio is about 16.5%). Thus, climate change has a major impact on the corrosion initiation time of concrete structures.

Discussion

This study provides a new approach to predicting the corrosion initiation time. This approach takes into account the effect of temperature rise and sea level rise. The study also considers the impact of global warming (temperature rise) on the diffusion coefficient. Due to a high sea level rise, the distance between the structures and the coastline decreases, and thus, the chloride concentration at the structure's surface increases. We review the effect of sea level rise on the surface chloride concentration by using Bruun's studies.

According to the climate change scenario for the North Central Coast of Vietnam, which has a tropical climate, the corrosion initiation time of reinforced concrete decreases by about 16.5% when the impact of temperature rise and sea level rise is taken into account. When only considering temperature rise, the corrosion initiation time decreases by about 9.0%. The results of this study show that climate change has a significant impact on the corrosion initiation time of reinforced concrete structures.

Acknowledgments

This study is supported by Vinh University, Vietnam and St. Petersburg State University of Architecture and Civil Engineering.

References

ADB (2013). *Viet Nam: Environment and climate change assessment.* Manila: Asian Development Bank. p. 68.

Andrade, C. and Castillo, A. (2003). Evolution of reinforcement corrosion due to climatic variations. *Materials and Corrosion,* Vol. 54, Issue 6, pp. 379–386. DOI: 10.1002/maco.200390087.

ASTM (2012). ASTM C1202–18. Standard test method for electrical indication of concrete's ability to resist chloride ion penetration. West Conshohocken: ASTM International. C1202–18, p. 8.

ASTM (2013). ASTM C33. Standard Specification for Concrete Aggregates. West Conshohocken: ASTM International.

Bastidas-Arteaga, E., Chateauneuf, A., Sánchez-Silva, M., Bressolette, Ph., and Schoefs, F. (2010). Influence of weather and global warming in chloride ingress into concrete: A stochastic approach. *Structural Safety,* Vol. 32, Issue 4, pp. 238–249. DOI: 10.1016/j.strusafe.2010.03.002.

Bentz, E. C. and Thomas, M. D. A. (2001). Life-365 Service Life Prediction Model and computer program for predicting the service life and life-cycle costs of reinforced concrete exposed to chlorides. *User Manual,* Version 2.

Clifton, J. R. (2000). ACI 365.1R-00. Service-life prediction — state-of-the-art report. [online] Available at: http://civilwares.free.fr/ACI/MCP04/3651r_00.pdf [Date accessed 12.04.2021].

Dixon, D. E. (1991). *Standard practice for selecting proportions for normal, heavyweight, and mass concrete* (ACI 211.1–91). [online] Available at: https://kashanu.ac.ir/Files/aci%20211_1_91.pdf [Date accessed 17.02.2021].

DuraCrete (2000). Brite EuRam: DuraCrete — Final technical report. Probabilistic performance based durability design of concrete structures. Document BE95–1347/R17.

Gao, X.-J. and Wang, X.-Y. (2017). Impacts of global warming and sea level rise on service life of chloride-exposed concrete structures. *Sustainability,* Vol. 9, Issue 3, article 460. doi: 10.3390/su9030460.

Gjørv, O. E. (2011). Durability of concrete structures. *Arabian Journal for Science and Engineering,* Vol. 36, Issue 2, pp. 151–172. DOI: 10.1007/s13369–010-0033–5.

Hanh, P. T. T. and Furukawa, M. (2007). Impact of sea level rise on coastal zone of Vietnam. *Bulletin of the College of Science. University of the Ryukyus,* No. 84, p. 45–59.

Van den Heede, P., Maes, M. and De Belie, N. (2014). Influence of active crack width control on the chloride penetration resistance and global warming potential of slabs made with fly ash + silica fume concrete. *Construction and Building Materials,* Vol. 67, Part A, pp. 74–80. DOI: 10.1016/j.conbuildmat.2013.10.032.

Loreto, G., Di Benedetti, M., De Luca, A., & Nanni, A. (2019). Assessment of reinforced concrete structures in marine environment: a case study. Corrosion Reviews, 37(1),pp. 57–69.

Knott, J. F., Elshaer, M., Daniel, J. S., Jacobs, J. M. and Kirshen, P. (2017). Assessing the effects of rising groundwater from sea level rise on the service life of pavements in coastal road infrastructure. *Transportation Research Record: Journal of the Transportation Research Board,* Vol. 2639, Issue 1, pp. 1–10. DOI: 10.3141/2639–01.

Kwon, S. J., Na, U. J., Park, S. S. and Jung, S. H. (2009). Service life prediction of concrete wharves with early-aged crack: Probabilistic approach for chloride diffusion. *Structural Safety,* Vol. 31, Issue 1, pp. 75–83. DOI: 10.1016/j.strusafe.2008.03.004.

L'Hostis, V., Millard, A., Perrin, S., Burger, E., Neff, D. and Dillmann, P. (2011). Modelling the corrosion–induced cracking of reinforced concrete structures exposed to the atmosphere. *Materials and Corrosion*, Vol. 62, Issue 10, pp. 943–947. DOI: 10.1002/maco.200905578.

Medeiros-Junior, R. A. (2018). Impact of climate change on the service life of concrete structures. In: Pacheco-Torgal, F., Melchers, R. E., Shi, X., De Belie, N., Tittelboom, K. V. and Sáez, A. (eds.) Eco-Efficient Repair and Rehabilitation of Concrete Infrastructures. Elsevier, pp. 43–68. DOI: 10.1016/B978–0-08–102181-1.00003–4.

Medeiros-Junior, R. A., Lima, M. G. and Medeiros, M. H. F. (2015). Service life of concrete structures considering the effects of temperature and relative humidity on chloride transport. *Environment, Development and Sustainability,* Vol. 17, Issue 5, pp. 1103–1119. DOI: 10.1007/s10668–014-9592-z.

Pijaudier-Cabot, G., Haidar, K., Loukili, A. and Omar, M. (2004). Ageing and durability of concrete structures. In: Darve. F. and Vardoulakis, I. (eds.) *Degradations and Instabilities in Geomaterials.* Vienna: Springer, pp. 255–286. DOI: 10.1007/978–3-7091–2768-1_9.

Ranasinghe, R., Callaghan, D. and Stive, M. J. F. (2012). Estimating coastal recession due to sea level rise: beyond the Bruun rule. *Climatic Change,* Vol. 110, Issue 3–4, pp. 561–574. DOI: 10.1007/s10584–011-0107–8.

Saha, M. and Eckelman, M. J. (2014). Urban scale mapping of concrete degradation from projected climate change. *Urban Climate,* Vol. 9, pp. 101–114. DOI: 10.1016/j.uclim.2014.07.007.

Standard, A. (2013) "C33, Standard Specification for Concrete Aggregates. 1996," Annual Book of ASTM Standards, pp.1–11.

Stewart, M. G., Wang, X. and Nguyen, M. N. (2011). Climate change impact and risks of concrete infrastructure deterioration. *Engineering Structures,* Vol. 33, Issue 4, pp. 1326–1337. DOI: 10.1016/j.engstruct.2011.01.010.

Stewart, M. G., Wang, X. and Nguyen, M. N. (2012). Climate change adaptation for corrosion control of concrete infrastructure. *Structural Safety,* Vol. 35, pp. 29–39. DOI: 10.1016/j.strusafe.2011.10.002.

Talukdar, S. and Banthia, N. (2013). Carbonation in concrete infrastructure in the context of global climate change: Development of a service lifespan model. *Construction and Building Materials,* Vol. 40, pp. 775–782. DOI: 10.1016/j.conbuildmat.2012.11.026.

Thao, N. D., Takagi, H. and Esteban, M. (eds). (2014). *Coastal disasters and climate change in Vietnam: Engineering and planning perspectives*. London, Watham: Elsevier, 393 p.

Thomas, M. D. A. and Bentz, E. C. (2002). Computer program for predicting the service life and life-cycle costs of reinforced concrete exposed to chlorides. In: *Life365 Manual,* SFA, pp. 12–56.

Thuc, T., Thang, N. V., Huong, H. T. L., Khiem, M. V. Hien, N. X. and Phong, D. H. (2016). *Climate change and sea level rise scenarios for Viet Nam*. Ha Noi: Ministry of Natural Resources and Environment, 170 p.

Tran, T. T., Truong, Q. V., Ranaivomanana, H. and Abdelhafid, K. (2018). Effect of pre-loading on chloride diffusion in concrete. *Journal of Asian Concrete Federation,* Vol. 4, No. 2, pp. 22–28. DOI: 10.18702/acf.2018.07.3.1.22.

Vu, K. A. T. and Stewart, M. G. (2000). Structural reliability of concrete bridges including improved chloride-induced corrosion models. *Structural Safety,* Vol. 22, Issue 4, pp. 313–333. DOI: 10.1016/S0167–4730(00)00018–7.

Wang, X.-Y., Lee, H. and Kwon, S. (2018). Analysis of service life of cracked marine concrete considering global warming and Bruun rule. *International Journal of Sustainable Building Technology and Urban Development,* Vol. 9, Issue 2, pp. 61–73. DOI: 10.22712/susb.20180007.

DOI: 10.23968/2500-0055-2021-6-2-45-51

EXPERIMENTAL MODELING OF SNOW ACTION ON UNIQUE CONSTRUCTION FACILITIES

Olga Poddaeva

Head of the University Research and Production Laboratory for Aerodynamic and Aero-Acoustic Testing of Building Structures, National Research Moscow State University of Civil Engineering
26, Yaroslavskoye Shosse, Moscow, Russia

E-mail: poddaevaoi@gmail.com

Abstract

Introduction: In modern civil engineering, repetitive architecture gives way to unique buildings. However, the available laws and regulations do not provide any recommendations for setting loads on unique construction facilities. The foregoing is fully true for snow loads as well. The Regulations “Loads and Actions” include a method to calculate snow loads for standard roof shapes. **Methods:** This paper proposes a method of experimental modeling for snowdrifts and snow deposits on complex roof shapes that differ from the standard shapes described in the Regulations, using wind tunnels of architectural and construction type. This method provides clear recommendations on experimental studies with the use of wind tunnels. **Results:** It was tried and tested in the building of a sports center under design. During the study, patterns of snowdrifts and snow deposits formation were also obtained.

Keywords

Aerodynamics, wind tunnel, snow actions, snow deposits, experimental studies, snowdrifts.

Introduction

Technological advances together with the development of computer modeling in construction made it possible for architects to design unique buildings in terms of their shape. However, this achievement raised a number of issues before engineers and designers regarding the development of design documentation. When erecting a building with original spatial forms, additional studies are required on the impact of natural and man-made factors, including wind and snow actions (Shishkina and Kaloshina, 2018; Shumeyko and Kudinov, 2013).

Nowadays, one of the most important design tasks is to account for the snow load on complex roofing having a shape that differs from the primitive elements listed in the Regulations SP 20.13330.2016 “Loads and Actions” (Ministry of Construction of Russia, 2016; Popov et al., 2016). This is due to the fact that, in buildings with non-standard roofing, it is impossible to predict snowdrifts with analytical methods (Churin and Gribach, 2016).

The snow load on the roof surface is determined as the snow weight per unit of area. This value depends on climatic conditions in the built-up area. However, elements that prevent snowdrifts on the roof surface are also important in determining the snow load.

Methods

This paper proposes a method for experimental studies of snow action on buildings, performed in the Large Research Gradient Wind Tunnel (Churin and Gribach, 2016).

According to this method, a study shall be performed as follows:

1. Analysis of meteorological and topographical data in the built-up area;
2. Design and creation of a scaled-down model for the studied facility;
3. Experimental modeling of the snow cover to determine basic patterns of snowdrifts and snow deposits formation on the roof surface of the studied facility. The shapes of snow bags are analyzed to decompose the roof surface into primitive elements, and then the snow load is determined for these elements in accordance with the Regulations.
4. Development of conclusions and recommendations based on the findings.

Experimental determination of basic patterns of snowdrifts and snow deposits formation on the roof surface of construction facilities includes the following steps:

— a uniform layer of the model material (wood powder 200, bulk density — 200 kg/m3, moisture — 3.5–4%) with a thickness of 1–1.5 mm is applied to the model;

— the flow velocity increases uniformly from 0.1 to 7.9 m/s (up to Level 4 according to the Beaufort Wind Scale), the model material moves from the smooth painted surface at the wind velocity of 3.4 m/s. The velocity is controlled using appropriate verified equipment. When model material begins to drift, the flow velocity becomes steady, and air

blowing continues until the formation of distinctive snow deposits. The starting points of drifting and formation of distinctive snow deposits are determined visually;

— photos of snowdrifts are made;

— the model turns in the tunnel with a pitch corresponding to the experimental conditions (as a rule, the most distinctive wind directions at the construction site in winter are considered). The process of model material application and air blowing is repeated for each angle;

— based on the results of the experimental modeling, distribution patterns of the coefficient μ are built for further calculation of the snow load.

Particular attention should be given to the selection of special substances modeling snow. For instance, Isyumov (1979) used bran as the substance modeling snow in wind-tunnel testing in order to study snowdrifts at the lower level of a two-level roof at different wind velocities and directions.

O'Rourke et al. (O'Rourke et al., 2004, 2005; Thiis and O'Rourke, 2012) studied snowdrift velocities on roofs of different shapes in a water flume using crushed walnut shells and obtained good agreement when comparing the results with those of field studies.

They also considered the matters of establishing the estimated snow loads. O'Rourke's papers provided the basis for structural analysis considering snow loads in American standards (American Society of Civil Engineers, 2005).

Professor A. A. Semenov and PhD students at the Ufa State Petroleum Technological University, together with experts from UNICON Novosibirsk Department, carried out experimental studies of the snow load on the roofs of cylindrical tanks in a special wind tunnel of architectural and construction type. They used wood powder as the model material (Porivaev et al., 2012).

In addition to the studies of the snow action on the roofs of buildings and structures, we should mention studies of snowdrifts in urban pedestrian areas. Such studies were conducted in Japan at the Hokkaido Building Research Institute (Setoguchi, 2011). The territory in the northern part of Japan was studied. It is a cold and heavy snowfall region where many cities experience snowstorms. Setoguchi modeled not only snow loads but also snowdrifts. The designed area should be comfortable for pedestrians. It should be barrier-free (i.e., accessible for the elderly and the disabled). Therefore, it should accumulate as little snow as possible. Besides, the area should have commercial buildings and information boards and signs. The experiment was aimed at choosing the most optimal location of the facilities in the area so that to ensure no snow piles in the pedestrian areas and easy snow removal. Snow was modeled using white soil powder since its properties are similar to those of snow in Japan. In the course of the study, several location options for the facilities were considered. For each option, snow cover and snowdrift distribution patterns were obtained, and the optimal design of the area was chosen. The resulting design minimizes the negative effect of snow actions on the designed area.

Results

This paper describes testing of the method described above, using the building of a sports center being designed in Yekaterinburg as an example (Fig. 1).

According to Step 1 of the method, the climatic region (I-V), the prevailing wind directions (western and north-western), and the average annual wind velocity (3 m/s) were determined in the development area.

Then, based on the initial data, a model of the studied facility was designed and created (Pomelov et al., 2016). Considering the dimensions of the test section of the wind tunnel, the model scale of 1:150 was chosen as the maximum possible scale under the blockage conditions. The studied model was rigidly mounted on an automatic turntable in the test section of the wind tunnel at the 0-degree mark relative to the direction of the ram air (Fig. 2).

Then, the study was conducted: a uniform layer of the model material (wood powder 200, bulk density — 200 kg/m^3, moisture — 3.5–4%) with a thickness of 1–1.5 mm was applied to the model. After the wind tunnel engines were started and the wind velocity reached 6–7 m/s, air blowing was performed until the formation of distinctive snow deposits on the roof surface. The results were recorded by the experimental group. In accordance with the experimental conditions, full-circle exposure along the wind direction with a pitch of 90° was performed. Photos of snowdrifts at different wind directions are provided below. Based on these, it is possible to obtain data on the snowdrift types, as well as directions and volumes for each type of snowdrift (Churin and Gribach, 2016).

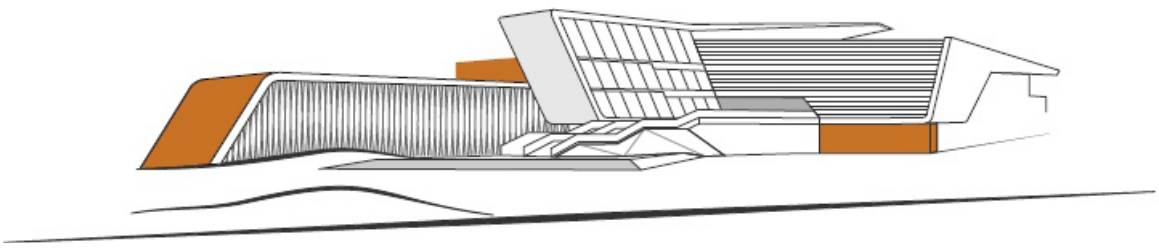

Figure 1. Facility under consideration

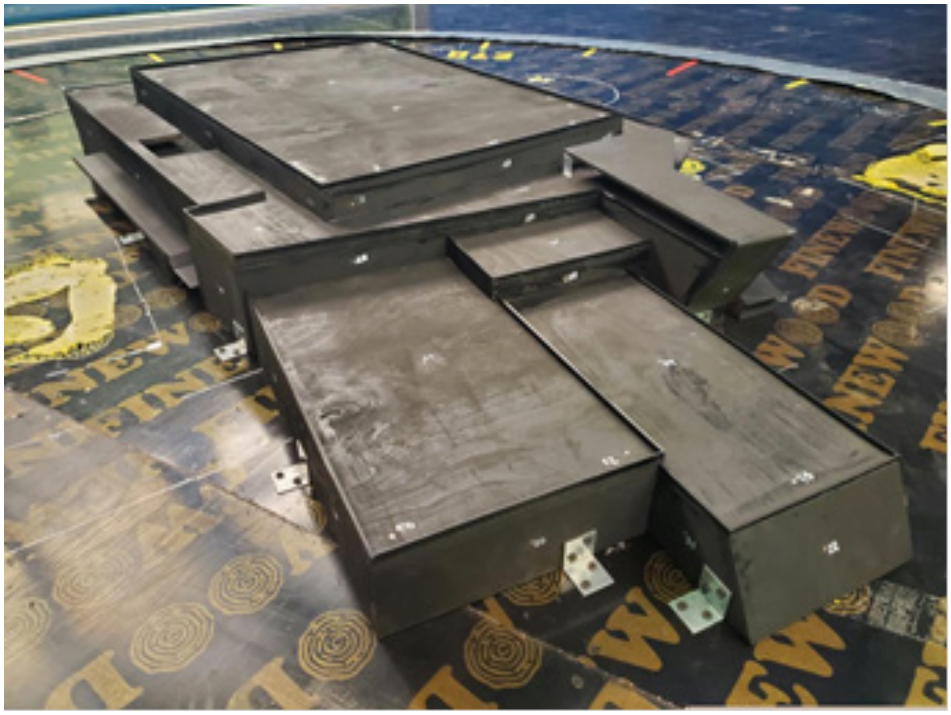

Figure 2. Model of the studied facility

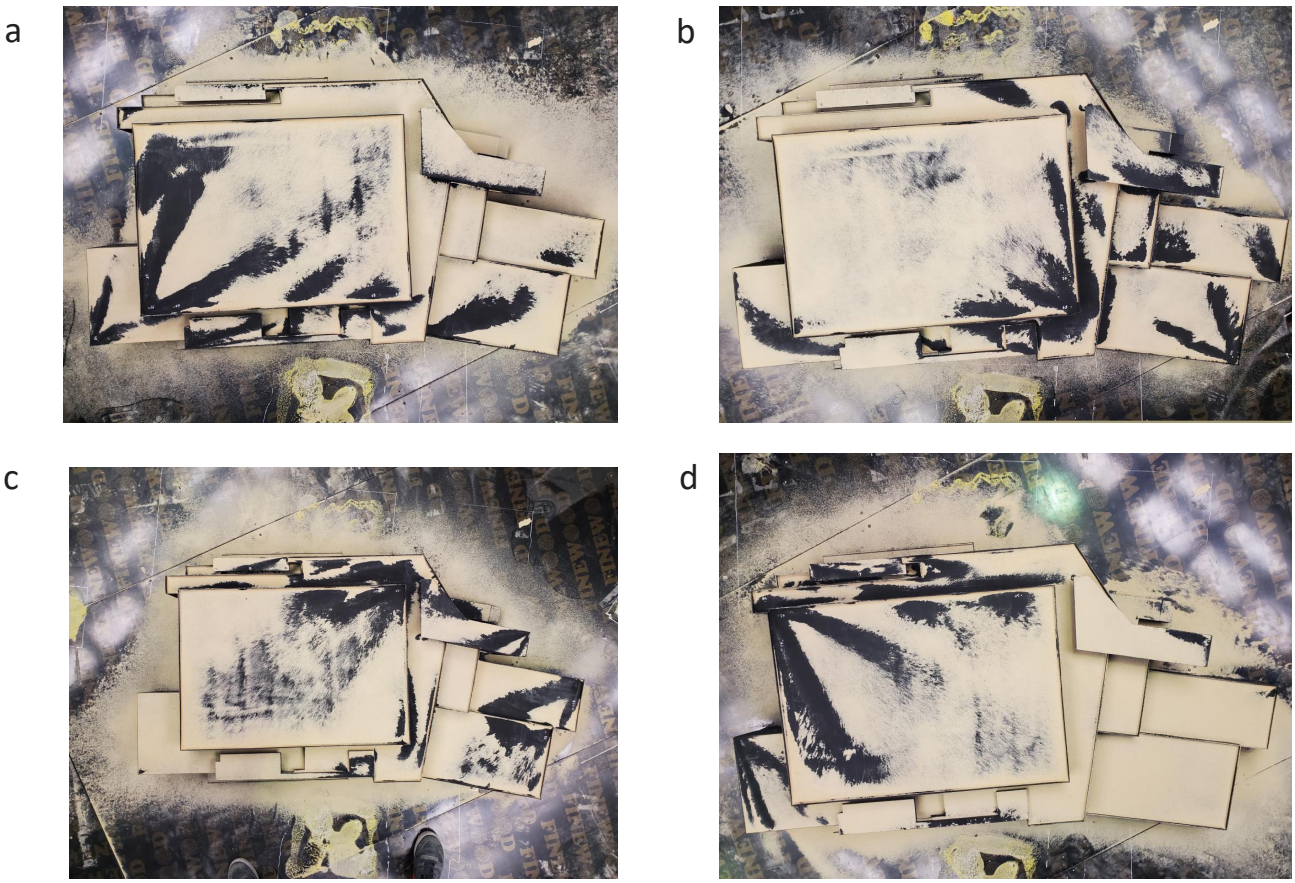

Figure 3. Distinctive zones of snow deposits at the following angles of the ram air: a — 0°, b — 90°, c — 180°, d — 270°

Taking into account the climatic analysis conducted, the distinctive wind directions in the development area in winter are the western (model position angle — 0°), north-western (model position angle — 45°), and south-eastern directions (model position angle — 225°). For these directions, diagrams of snow deposits on the roof surface of the studied facility were made after a series of aerodynamic tests (Fig. 4).

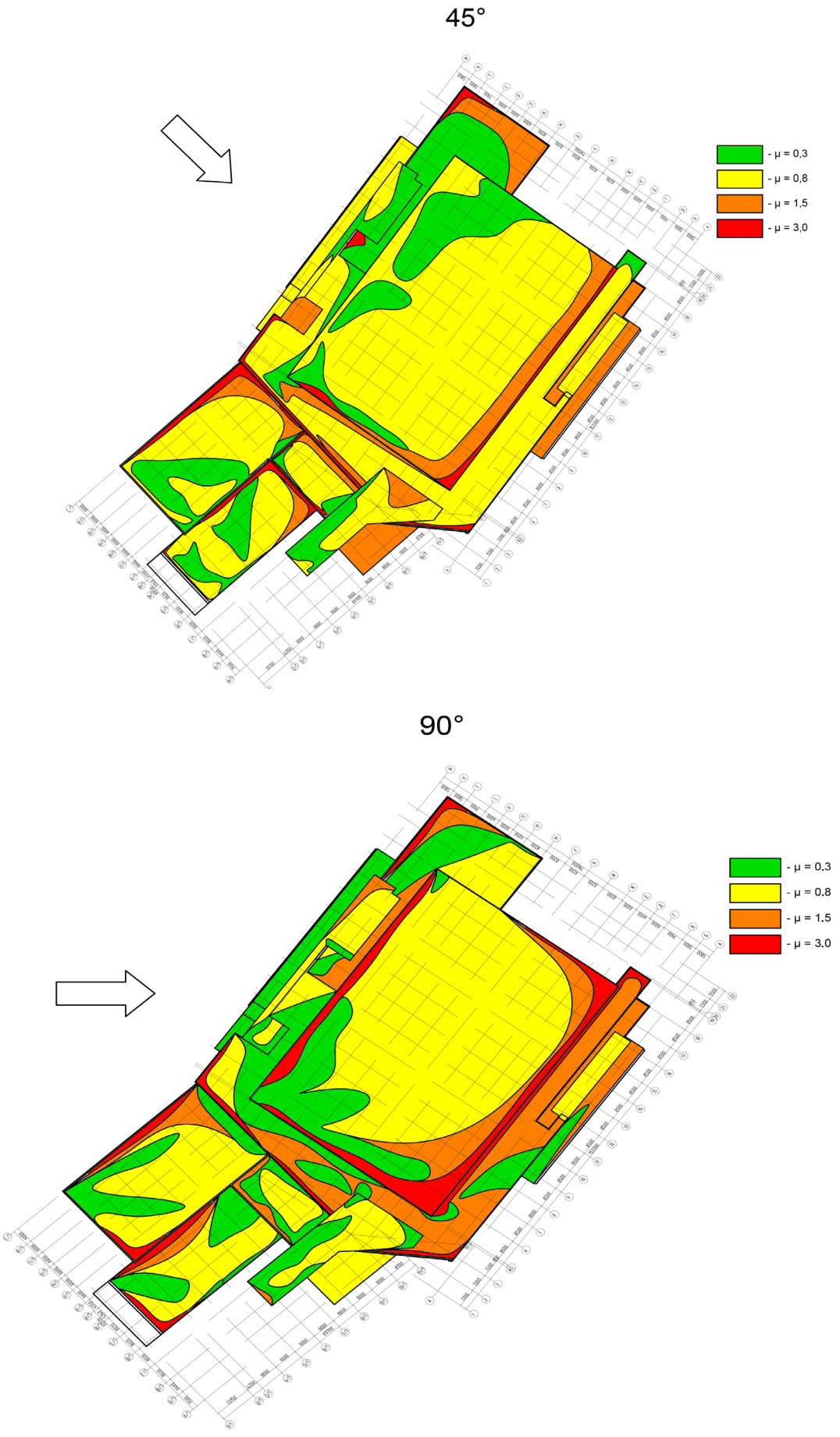

Figure 4. Diagrams of snow deposits

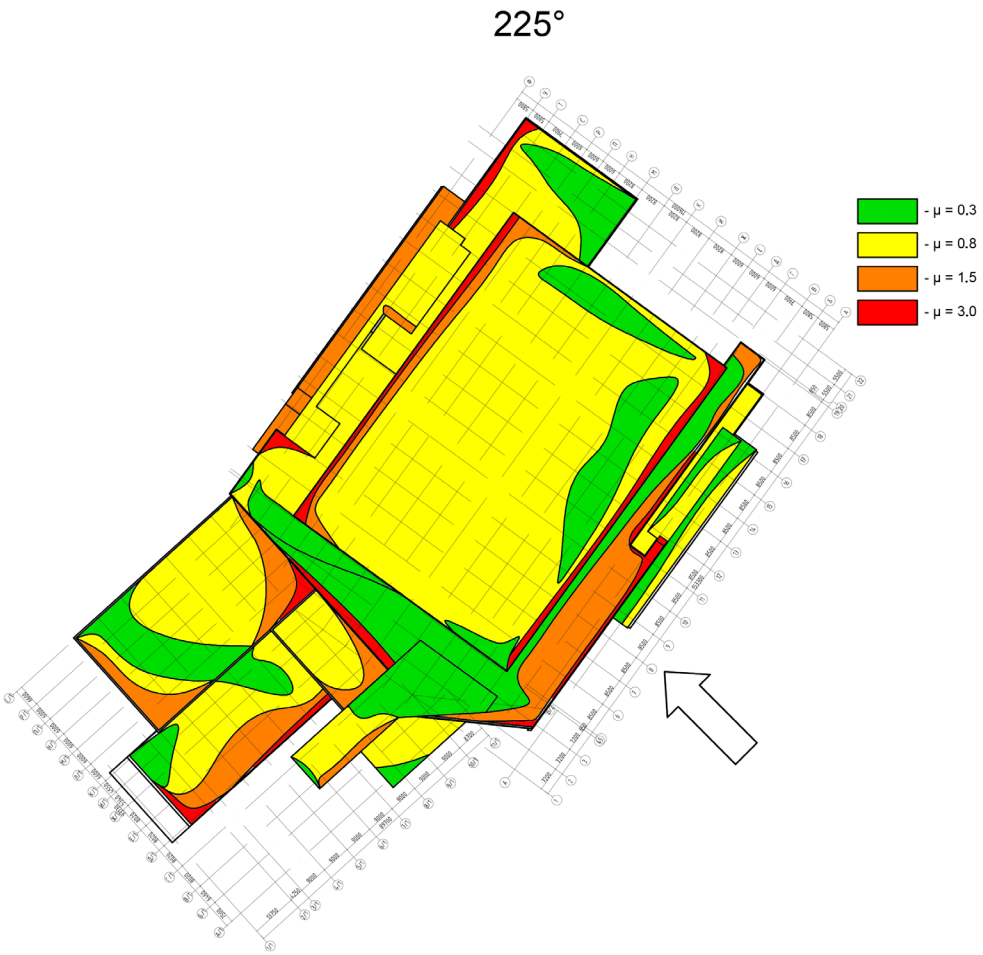

Figure 4. Diagrams of snow deposits

Discussion

The paper proposed a method of experimental modeling of snow actions on complex roof shapes, using wind tunnels. It provides clear recommendations on experimental studies of snow actions: the range of ram air velocities in the test section of the wind tunnel during testing, and the material that can be used as snow when modeling snow deposits and snowdrifts. This method was tried and tested in a structure being designed. As a result, distinctive zones of snow deposits were obtained. The method can be applied to facilities with roofs of shapes that differ from the primitive elements listed in the Regulations SP 20.13330.2016 “Loads and Actions”.

Acknowledgments

This work was financially supported by the Ministry of Science and Higher Education of the Russian Federation (Project: Theoretical and experimental design of new composite materials to ensure safety during the operation of buildings and structures under conditions of technogenic and biogenic threats #FSWG-2020-0009).

References

American Society of Civil Engineers (2005). ANSI/ASCE 7-95. Minimum design loads for buildings and other structures. American Society of Civil Engineers, 419 p.

Churin, P. S. and Gribach, J. S. (2016). Experimental study of wind and snow influence on projected airport complex. *Industrial and Civil Engineering,* Issue 11, pp. 24–27.

Isyumov, N. (1979). *An approach to the prediction of snow loads. PhD Thesis.* London, Canada: University of Western Ontario.

Ministry of Construction of Russia (2016). Regulations SP 20.13330.2016. Loads and actions. *Revised edition of Construction Rules and Regulations SNiP 2.01.07-85* (with Amendments Nos. 1, 2).* Moscow: Standartinform.

O'Rourke, M., DeGaetano, A. and Tokarczyk, J. D. (2004). Snow drifting transport rates from water flume simulation. *Journal of Wind Engineering and Industrial Aerodynamics*, Vol. 92, Issue 14–15, pp.1245–1264. DOI: 10.1016/j.jweia.2004.08.002.

O'Rourke, M., DeGaetano, A. and Tokarczyk, J. D. (2005). Analytical simulation of snow drift loading. *Journal of Structural Engineering,* Vol. 131, Issue 4, pp. 660–667. DOI: 10.1061/(ASCE)0733-9445(2005)131:4(660).

Pomelov, V., Gribach, D. and Churin, P. (2016). Methods for prototyping high-rise and unique buildings and structures for carrying out aerodynamic tests. *Building and Reconstruction,* No. 3 (65), pp. 56–60.

Popov, N. A., Lebedeva, I. V., Bogachev, D. S. and Berezin, M. M. (2016). Impact of wind and snow loads on large-span roofs. *Industrial and Civil Engineering,* Issue 12, pp. 71–76.

Porivaev, I. A., Safiullin, M. N. and Semenov, A. A. (2012). Research of wind and snow cover loads on the roofs of the vertical cylindrical tanks. *Magazine of Civil Engineering,* Issue 5 (31), pp. 12–22.

Setoguchi, T. (2011). Public square design with snow and wind simulations using wind tunnel. In: Lerner, J. C. and Boldes, U. (eds.) *Wind tunnels and experimental fluid dynamics research.* DOI: 10.5772/18619.

Shishkina, A. V. and Kaloshina, S. V. (2018). Accounting for natural and climatic factors affecting housing construction. *Modern Technologies and Construction.* Theory and Practice, Vol. 2, pp. 86–93.

Shumeyko, V. I. and Kudinov, O. A. (2013). On the design features a unique, long-span and high-rise buildings and structures. *Engineering Journal of Don,* Issue 4.

Thiis, T. and O'Rourke, M. (2012). A model for the distribution of snow load on gable roofs. In: *Proceedings of the 7th International Conference on Snow Engineering,* Fukui, Japan.

ЭКСПЕРИМЕНТАЛЬНОЕ МОДЕЛИРОВАНИЕ СНЕГОВЫХ ВОЗДЕЙСТВИЙ НА УНИКАЛЬНЫЕ СТРОИТЕЛЬНЫЕ ОБЪЕКТЫ

Ольга Игоревна Поддаева

Заведующая УНПЛ по аэродинамическим и аэроаккустическим испытаниям строительных конструкций,
НИУ Московский Государственный Строительный Университет
Ярославское шоссе, 26, Москва, Россия

E-mail: poddaevaoi@gmail.com

Аннотация
В современном строительстве типовая архитектура уступает место нетиповой, в то время как нормативная база не содержит рекомендаций для назначения нагрузок на уникальные строительные объекты. Сказанное выше в полной мере справедливо и по отношению к снеговым нагрузкам. СП «Нагрузки и воздействия» содержит методику расчета на снеговые нагрузки для типовых форм кровель. **Методы:** В работе предложена методика экспериментального моделирования в аэродинамических трубах архитектурно-строительного типа явлений снегопереноса и снеговых отложений на покрытия зданий со сложной кровлей, отличающихся от приведенных в СП типовых форм. Приведенная в статье методика содержит четкие рекомендации по проведению экспериментальных исследований в аэродинамических трубах. **Результаты:** Представленная методика апробирована на здании проектируемого спортивного комплекса. Получены картины снегопереноса и снегоотложений.

Ключевые слова
Аэродинамика, аэродинамическая труба, снеговые воздействия, снеговые отложения, экспериментальные исследования, явление снегопереноса.

DOI: 10.23968/2500-0055-2021-6-2-52-62

ASSESSING THE IMPACTS OF CITY SPRAWL ON URBAN FREIGHT TRANSPORT IN DEVELOPING COUNTRIES

Bhavesh Dhonde[1]*, Chetan R. Patel[2]

[1]Department of Civil Engineering, Government Engineering College, Daman
Pin- 396 210, U.T. of Dadra & Nagar Haveli and Daman & Diu, India
[2]Department of Civil Engineering, Sardar Vallabhbhai National Institute of Technology (SVNIT), Surat
Pin- 395 007, Gujarat, India

*Corresponding author: bhaveshdhonde@gmail.com

Abstract

Introduction: In the 21st century, cities in developing countries have witnessed faster growth as compared with cities in developed countries. Countries like India, China and Brazil have one of the most densely populated cities in the world. The transport infrastructure in these cities struggles to deal with the increasing population and geographic sprawl. Though some efforts are made to improve the transportation systems in these cities, urban freight transport is largely overlooked as the focus remains on passenger transport. **Methods:** This study aims to assess the impacts of the city's geographic sprawl on urban freight transport using the example of the textile industry in Surat, India. The sprawl of the city and its textile industry is measured based on historical maps, Google imagery, and establishment surveys. Changes in urban freight trip lengths are determined using the data of a commercial vehicle drivers' survey. **Results:** In the last two decades, the city expanded geographically by almost three times. The relocation of textile manufacturing units led to a 40% increase in trip lengths and additional 56 tons of carbon dioxide generation per year. Due to the city sprawl, the overall efficiency of the urban freight transport system reduced. There is a need for a holistic planning approach towards urban freight movement and related urban infrastructure for sustainable freight flows. This can serve as a policy framework to decide on the location of a logistics hub or as guidelines to allocate manufacturing enterprises in the proximity of the urban area, thus enabling sustainable development of the city.

Keywords

Urban, freight, logistics, city sprawl, cities, developing countries.

Introduction

Rapid industrialization and mass urbanization in cities have generated a challenging situation for city managers to maintain a balance between the economic development of the city and a sustainable environment for its inhabitants. With city boundaries expanding over the years, trip lengths of passenger and freight transport have increased substantially. Urban freight trips generated by various industries largely depend on the type of industry, its geographic distribution in the city, and its supply chain requirements. The present study focuses on providing a technical background to the planners for considering the share of infrastructure requirements caused by industrial development. The textile industry of Surat is taken up as a case study. The supply chain of the textile industry is overly complex and freight-intensive in nature. Hence, the textile industry is selected for studying the impacts of freight transportation on city logistics.

The selected study area, Surat, has one of the biggest textile manufacturing hubs in the country. Surat is considered the economic capital of Gujarat state. It is a pivotal center on the Delhi–Mumbai side of the Golden Quadrilateral, having direct linkages with the industrial urban centers of Vadodara, Ankleshwar, and Vapi. Fig. 1 shows the location of Surat on the map of India. Surat has been a prominent mercantile node on the western coast of India since the 17th century and a contemporary industrial city, which today presents a mix of continuity and change in its social and economic character. The city is popular for its textiles and diamond manufacturing industry. Surat is known as the Silk City of India, the Textile Capital of India, and the Diamond City.

In addition to textile manufacturing and diamond polishing, Surat also has quite well-developed enterprises in the engineering, chemical, and IT sectors. The city witnesses migration of people seeking employment from other states of the country. The population of the city drastically increased from 2.8 million in 2001 to 4.6 million in 2011 (Directorate of

Census Operations, 2011). Though some surrounding areas were included within the municipal limits in the year 2006, the city is still one of the fastest-growing in terms of population (4.5% per annum). In terms of area covered, Surat is smaller than other major cities like Mumbai, Delhi, or Chennai; however, its population density is comparable to that in some of the most densely populated cities in the world. Table 1 presents such a comparison.

It can be seen that cities with the highest population densities are all located in Asia except for Lagos and Bogota (Table 1).

Table 1. Cities with the highest population densities

City	Country	Population	Area (km2)	Density (people/km2)
Mumbai	India	14.35	484	29,630
Kolkata	India	12.70	531	23,920
Karachi	Pakistan	9.80	518	18,920
Lagos	Nigeria	13.40	738	18,155
Shenzhen	China	8.00	466	17,160
Seoul	S. Korea	17.50	1049	16,685
Taipei	Taiwan	5.70	376	15,180
Chennai	India	5.95	414	14,360
Bogota	Columbia	7.00	518	13,515
Shanghai	China	10.00	746	13,410
Surat	India	4.46	326	13,680

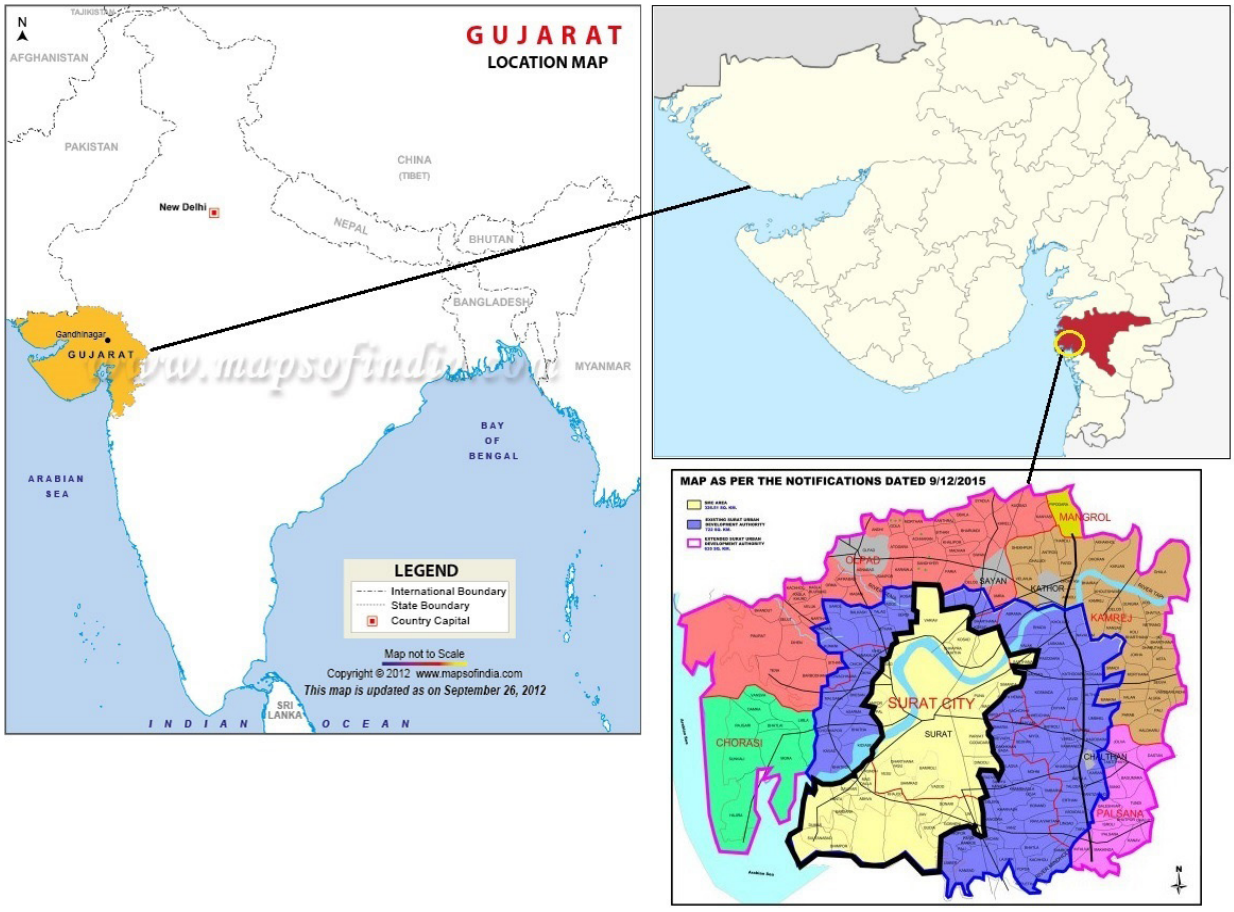

Figure 1. Location of Surat on the map of India
Source: Website of mapsofindia.com, suratmunicipal.gov.in

All the major cities in Europe and North America, which are more advanced in terms of urban freight transportation, do not have such high population densities. Proximity to Mumbai has helped various industries to prosper in Surat. It has two seaports, Hazira and Magdalla, for supporting overseas trade. It is well connected by national highways and railways with major cities like Mumbai and Delhi. The city has recently got an international airport providing direct flights to Indian and global cities, which boosts the business potential of Surat and leads to further growth of its textile industry.

City Sprawl of Surat

Surat witnessed a radial spatial expansion along five major corridors in the north, south, east, west, and south-west of the city till the end of the 1980s. Since then, the city has been growing rapidly in the eastern, southern, and south-western directions. Nearby towns are periodically included in the city's municipal limits by the Surat Urban Development Authority (SUDA). One of the major expansions was in the year 2006 when the city's area increased from 112.28 sq. km (2001) to 326.5 sq. km. It is proposed to expand the boundaries further, from 326.5 sq. km to 496.52 sq. km. The proposal is currently under consideration by the planning authorities. Fig. 2 shows the increase in the built-up area of the city. As per the mid-year estimates drawn by the Surat Municipal Corporation, the population of the city is believed to be around 6.63 million in the year 2020 and 6.93 million by the next official census in the year 2021.

The growth of the built-up area of the city is shown in five-year intervals from the year 2000 to 2018. The urbanized area in Surat city increased by almost three times between 1978 and 2004, with development mainly occurring within the municipal limits of the city. The metropolitan area has developed largely in terms of residential and industrial clusters (Surat Urban Development Authority (SUDA), 2018).

Textile Industry in Surat

Surat is one of the largest centers in the world to produce synthetic fibers, mainly nylon and art silk. Around 90% of polyester used in India comes from Surat. The city accounts for 40% of the total nation's man-made (synthetic) fabric production and 28% of man-made fiber production. It also accounts for 18% of the total nation's man-made fiber export. The textile industry in Surat produces 30 million meters of raw fabric and 25 million meters of processed fabric daily (Government of Gujarat, 2017). The textile industry has developed organically, and its manufacturing clusters are spread across the city. The major segments of the industry are weaving units, processing units, value-addition units, and the textile

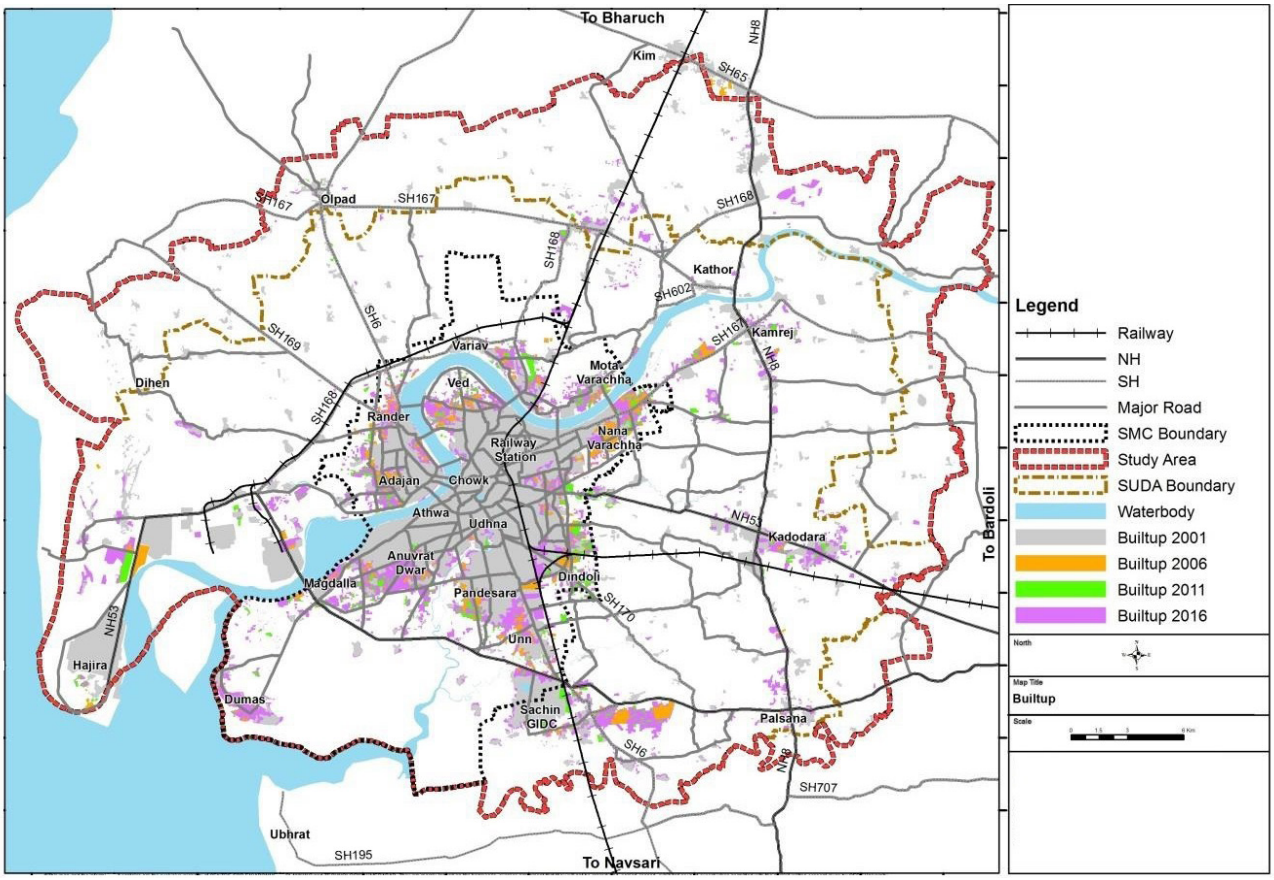

Figure 2. Growth of Surat city over time
Source: Comprehensive Mobility Plan Surat 2046 (Surat Urban Development Authority (SUDA), 2018)

market. The manufacturing segments in the form of industrial clusters are spread all over the city. The textile market is located in the ring road area of the city. The textile market also serves as a distribution center for textile raw materials and semi-finished goods. Table 2 shows characteristics of various production facilities of the textile industry established in the city. Since 1956, the Indian Government's policy of providing incentives and protection to small-scale enterprises has given a major boost to power loom weaving in the city. The industry has grown rapidly owing to the huge demand from the domestic market as well as the Middle East countries. Exports to other parts of the world have also increased gradually.

Table 2. Characteristics of the textile industry in Surat

Type of units	No. of units	No. of clusters	Approximate area occupied
Weaving units	25,000	24	3,000,000 sq. m
Processing units	400	5	743,000 sq. m
Value-addition units	11,000	12	1,200,000 sq. m (approx.)
Trading	75,000	2	3,300,000 sq. m (approx.)

As stated above, there are four major manufacturing segments in the textile industry in the city: weaving units, processing units, value-addition units, and a distribution hub (textile market). Some weaving units are small-scale with only 12 weaving machines (power looms) in a single unit. The total number of weaving units operating in the city is 25,000. The same is the case with embroidery work units. Dyeing, printing, and sizing of raw fabric are done at processing units. These units require large investments in machinery, labor, and land. Therefore, in most cases, they are managed by private or public limited companies. Trading units are represented by shops for bulk sales and purchase of raw, semi-finished, or finished textile products. The textile market occupies an area of approx. 3 sq. km, where 160–170 building complexes house more than 75,000 textile trading units or shops.

The number of power looms in the city increased from approx. 25,000 in 1980 to approx. 650,000 in 2018. As per the data obtained from the above sources, the city currently has approx. 650,000 power looms and approx. 50,000 shuttleless looms in 25,000 weaving units, nearly 120,000 embroidery machines in 11,000 value-addition units, 400 processing units, 160–170 wholesale complexes with approx. 75,000 trading units. The textile industry employs (directly and indirectly) around 1.5 million people in the city.

Literature Review

Urban sprawl (city sprawl) is traditionally studied with reference to the entire logistics or warehouse industry in the city or metropolitan region. The effects of urban sprawl with regard to industries and their freight flow patterns have not been sufficiently explored. Urban sprawl has an impact on the warehouse industry, which affects the overall freight trip characteristics in a broader sense as compared with a particular industry. Though the present study is focused on the sprawl of the textile industry in the city and its effects on freight flow patterns, we review the existing studies on urban sprawl to gain an in-depth understanding of various methodologies used for curbing uncontrolled sprawl and/or mitigating congestion impacts.

The location of logistics facilities significantly affects not only the urban goods movement but also the urban environment since such facilities are major originators and receivers of freight. The freight industry appears to have contradicting issues in urban areas, as it is required to operate efficiently and sustainably and adjust to the increasing urban freight activities (Aljohani and Thompson, 2016). The mega-region concept is particularly well-suited to the analysis of freight transport systems because freight transport's market areas, driven by global supply chains, are largely disconnected from a single city and spatially organized on a regional and multicity basis (Dablanc and Ross, 2012). Some recent research focuses on the megaregional scale, showing its significance for the understanding of freight flows and the increasing interconnection of facilities. Megaregions, as they contain both urban and suburban environments, have a higher share of road transport, which significantly adds to severe congestion issues. In the future, this will threaten the country's logistics performance.

Dablanc et al. (2014) compared the growth in geographic distribution of warehouses in the Los Angeles, California, and Seattle, Washington, metropolitan areas during 1998–2009. To measure sprawl, the barycenter, or geographic center of warehousing establishments, was determined, as was the average distance of warehouses to that center. Warehousing in Los Angeles sprawled considerably, with the average distance increasing by 6 miles, while in Seattle, the region locations remained relatively stable. Dablanc et al. explained that logistics sprawl characteristic of exceptionally large metropolitan areas, which serve both as trade nodes to the entire region and country as well as enormous consumer markets. Differences in land prices are also considered as an important factor in the large metropolitan areas (Dablanc et al., 2014; Woudsma

et al., 2016). According to Sakai et al. (2015), from the year 1980 to 2003, logistics facilities in the Tokyo Metropolitan Area migrated outward, although on a much smaller scale as compared with some U. S. and European cities. Besides, the authors' analysis of the shipment data confirmed that logistics sprawl increases truck travel. Furthermore, they found that, regardless of their age, logistics facilities tend to increase shipping distances as their distances to the urban center increase, due to the spatial mismatch between the locations of the facilities and the shipment origins and destinations. According to Lindholm and Behrends (2012), the common challenge for the cities is that freight transport is growing. Freight transport is needed for the cities to be liveable as well as functional, but at the same time citizens perceive it as a disturbing factor for local sustainability. On the other hand, local authorities recognize freight transport as an important factor for the economic development of their region. The NCHRP Report 739 and NCFRP Report 19 state the following: in short, the freight transportation system will need to do more with less. This adds pressure to state transportation agencies and metropolitan planning organizations to balance the conflicting objectives of the stakeholders involved and impacted by freight. The lack of research and data concerning freight affects all facets of transportation demand analysis: generation of cargo, distribution, mode choice, and traffic assignment (Transportation Research Board of the National Academies, 2012).

In their study, Dablanc and Rakotonarivo (2010) discussed that the Paris (Ile-de-France) region had witnessed deconcentration of parcel transport terminal locations over the period of 1974–2008. The centrographic analysis, performed by them, showed an increased mileage resulting from those more distant terminals, which they translated into net added CO2 emissions of 15,000 tons per year. According to Diziain et al. (2012), the Ile-de-France region has concentrated its action on real estate and land use, with an objective of counter-acting logistics sprawl phenomena. The region has worked with private partners and identified five levels of markets for the emerging urban logistics real estate, ranging from large multi-story facilities to small-scale urban logistics service depots. Toilier et al. (2016) described methods to gather data on the urban goods movement in the Paris region occupying a territory of 12,000 sq. km. They used multidimensional data analysis methods to gather data on such a huge scale. According to Taniguchi et al. (2016), city logistics requires a range of data and information to define problems, develop models and evaluate schemes. Recent developments in ICT allow the performance of urban freight systems to be monitored more extensively and accurately. This provides opportunities for enhancing efficiency and reducing the impacts of goods movement in cities. Recent developments in alternative fuel vehicles and advanced manufacturing have good potential for reducing the impact of freight in urban areas.

Methods

The textile industry in Surat got a major boost in the 1980s when the textile industry in Mumbai witnessed a downfall due to labor union issues and bankruptcy. At the time, the city's boundaries were limited by the current ring road, which was considered the outermost road of the city. It enabled entry into the city from the railway station and the state transport bus terminal, which were then located on the outskirts. The textile market developed along the ring road due to easy access from those transport terminals. Over the years, the city expanded, and the ring road area became denser. The city grew rapidly and sprawled over an area of 326.5 sq. km. This expansion brought the transport terminals and the textile market area to the city center. Due to an increase in land prices, narrow streets, and lack of parking spaces, the industry gradually shifted to new locations on the outskirts. Since background data are limited, we consider only 20 years of the geographic expansion (sprawl) of the textile industry (from the year 2000 to 2019). The sprawl of the industry is estimated based on the data obtained from an establishment survey conducted at several textile manufacturing units and a map study using historical maps available from the Surat Municipal Corporation (Surat Urban Development Authority, 2017) as well as Google Maps. The sprawl of the textile industry in Surat can be divided into two processes: the sprawl of the manufacturing clusters and the expansion of the textile market area. To understand the characteristics of freight trips generated by the textile industry, we conducted an establishment survey at weaving units in various textile manufacturing clusters of the city. Its results are presented in detail in the section dedicated to the analysis of freight trips generated by the textile industry.

Sprawl of the Manufacturing Clusters

The manufacturing clusters of the textile industry are spread all over the city. The number of clusters gradually increased from 16 in 2000 to 26 in 2019 due to the sprawl of the city and the growth of the textile industry. Fig. 3 presents sprawl maps showing the expansion of the textile industry clusters from the year 2000 to 2019. The maps were developed using ArcMap software.

New clusters developed on the outskirts in the north, east, and south directions. Over the years, some clusters expanded in size while others became denser as the other types of land use were reduced. The sprawl of the manufacturing clusters shown in Fig. 3 is presented in 5–6-year intervals considering the periodic expansion of city limits. The maps were developed using information collected during the field survey and satellite imagery from Google Earth Pro. It should be noted that the size of a couple of industrial clusters located in the central area reduced

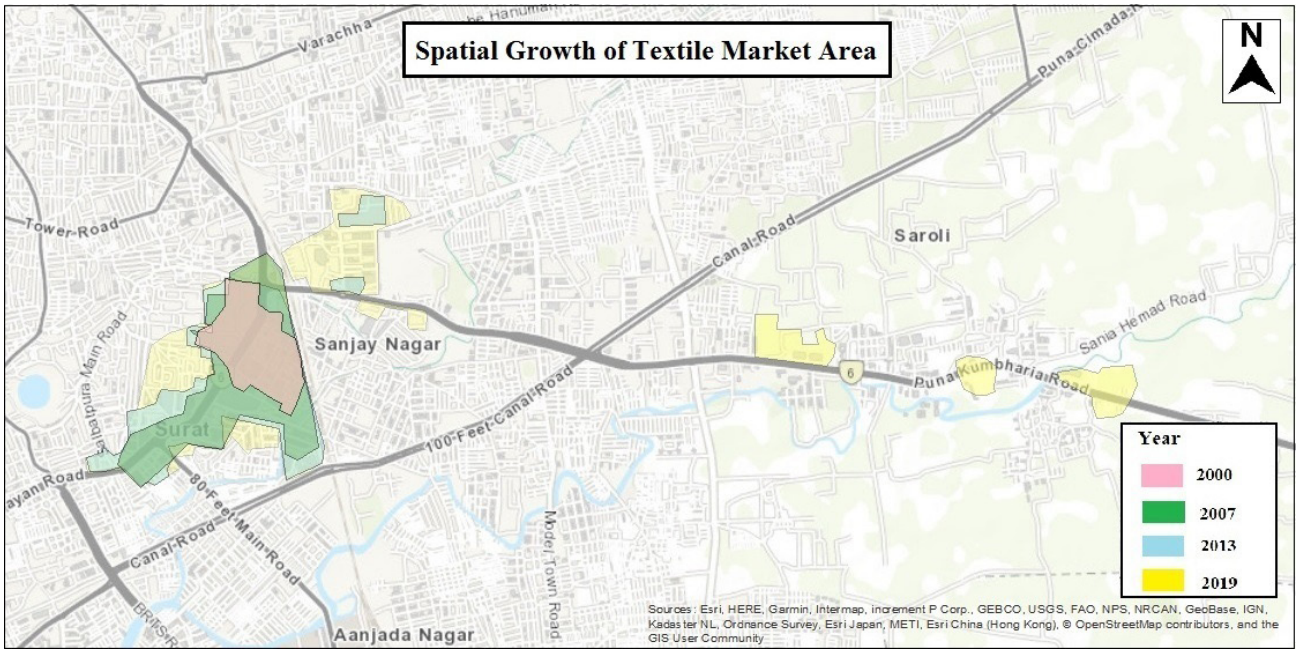

Figure 3. Spatial growth of the textile manufacturing clusters in 2000–2019
Source: Own work

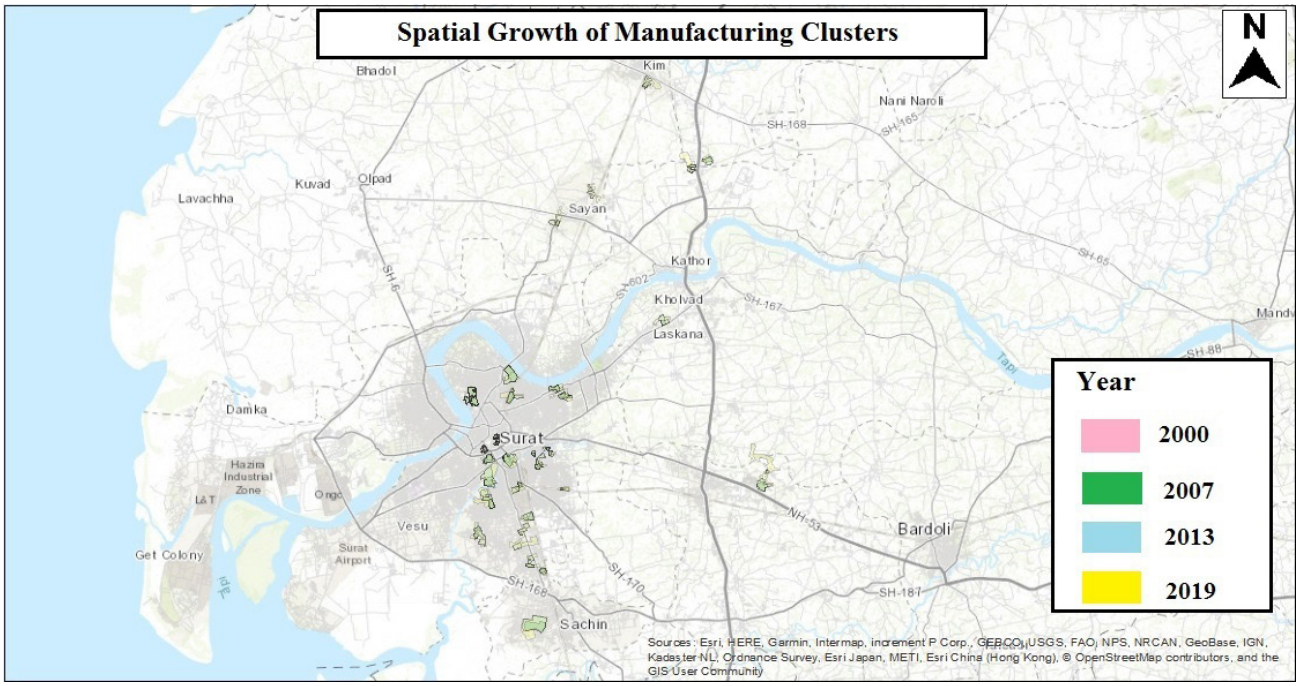

Figure 4. Spatial growth of the textile market area in 2000–2019
Source: Own work

over the years. This is due to the expansion of the textile market located nearby.

Sprawl of the Textile Market

The textile market developed along the ring road of the city, and its latest extension was in the direction of Surat–Bardoli Road. Over the years, more building complexes were constructed in the area solely for textile business purposes. Currently, there are around 160 functional textile market complexes in Surat along the ring road and almost 20 new complexes along the Surat–Bardoli Road, which are, however, sparsely located. Fig. 4 shows the expansion of the textile market area.

The textile market area can be considered the heart of the entire industry. Its location along the ring road is very strategic for the business due to its proximity to the Surat railway station and the central bus terminal of the city. In Fig. 4, the sprawl of the textile market area in 2000–2019 is shown with different color codes. The textile market area in Surat is one of India's largest trading districts with thousands of shops crammed into multiple malls or

commercial building complexes. Traders sell silk and cotton fabric, saris with intricate jari embroidery, and suits to local buyers and visitors. Along the ring road, the market is also lined with simple restaurants, banks, and offices of mobile service providers. These units are basically to cater to the requirements of those involved in the textile market. Since 2011, the market has witnessed eastward sprawl along Surat–Bardoli Road. Some sparsely located building complexes have become functional while many more are under construction or designed.

Increase in average distances in the textile industry

Our study of the geographic expansion of the textile industry included the temporal sprawl of the manufacturing clusters and the textile market area. Due to the limited data available, we analyzed only the last two decades. Over the years, the number and size of the manufacturing clusters increased and the clusters became quite dense. In fact, their number increased from 16 to 26 due to new clusters forming on the outskirts of the city. The textile market area has witnessed an increase in density as well as sprawl in the eastward direction with new complexes forming on Surat–Kadodara Road. Based on the study of the temporal growth of the manufacturing clusters and the textile market area, we determined that the average distance between a manufacturing cluster and the textile market area (considering the center-to-center distance) had increased from 5.9 km in 2000 to 10.17 km in 2019. This is due to new manufacturing clusters developed away from the city center as well as the growth of the clusters in size.

Analysis of Freight Trips Generated by the Textile Industry

It is difficult to obtain the exact data on the number of machines or units because the industry is highly segmented and characterized by small-scale operations. The industry also does not have any controlled manufacturing policy. Hence, the data obtained are just estimates provided by concerned authorities. It is assumed that the manufactured goods, leaving a segment, are delivered to the ring road trading market area, which causes 3–4 unnecessary trips during manufacturing of final products from grey cloth. We conducted a survey by visiting weaving units located in different parts of the city (250 weaving units were approached, and 122 owners agreed to participate in the survey). We cautiously supervised data collection at manufacturing units of different types and sizes to get an overall idea about freight trip generation characteristics. The data on the number and locations of various textile establishments in the city for the year 2008 were obtained from a local municipal body (Fig. 5). The details on the textile clusters for the corresponding year were obtained from the interviews carried out during the study. In total, 122 respondents shared information and knowledge about the industry and its spread in the city. The data obtained from various textile establishment owners were again sufficiently verified with the Regional Office of the Textile Commissioner.

Based on a freight carrier survey, we obtained data on the origins/destinations of trips of commercial vehicles during business hours of the ring road market. Table 3 shows results obtained for the origins/destinations of 1137 trips of commercial vehicles carrying textile goods. In order to quantify textile units, we represented graphically their dispersion around the center for the trading of textile goods in the city (i.e., the ring road market area) and performed a spatial analysis of the geographic data on the textile clusters. The row “Others” mentioned in Table 3 includes such areas as Kapodra, Karanj, Kosad, Olpad, Parvat Patiya, etc. The number of trips to these areas is less than the number of trips to other areas mentioned in Table 3. The trips within the ring road market area are characterized by the highest numbers. It can be seen from Table 3 that, in terms of the number, the trips within the ring road market area are followed by the trips to such clusters as Varachha, Pandesara GIDC, Kadodara, Sachin GIDC, and Palsana. The maximum trip length is 34.4 km to Kim followed by 21.8 km to Palsana. The minimum distance traveled is 2.6 km to Anjana. The average trip length is 11.17 km. Based on the data on the locations of the textile clusters in the city for the year 2008, we established that the farthest one was Kamrej (in 18.2 km), while the majority of the enterprises were in the area of Bhatena, Ved Road, Sagrampura, and Salabatpura located very close to the ring road market center. It is not quite possible to analyze the origins/destinations for the year 2008 now, but if we assume the same freight flow frequency, then the average freight trip length will be 6.73 km. It can be inferred that the average freight trip length increased by 4.44 km in the last decade. If the assumptions are true and the industry gains momentum within the government’s campaign, trade experts expect the industry to grow by 12–15% percent annually. With the expansion of the city, freight trip lengths are also bound to increase.

Table 3. OD survey count in the textile market area

Origin location	Destination location	Distance (km)	Percentage
Ring road market	246 (internal)	-	21.64
Amroli	6	9.3	0.53
Anjana	23	2.6	2.02
Bamroli	10	8.9	0.88
Bhatar	41	6.8	3.61
Bhatena	13	2.6	1.14
Bhestan	10	6.9	0.88
Chowk Bazar	6	2.7	0.53

Dindoli	20	4.9	1.76
Gadodara	16	6.7	1.41
Kadodara	83	11.1	7.30
Kamrej	34	18.2	2.99
Katargam GIDC	28	5.7	2.46
Kim	10	34.4	0.88
Limbayat	12	3.3	1.06
Palsana	58	21.8	5.10
Pandesara GIDC	130	9	11.43
Sachin GIDC	73	14.9	6.42
Saroli	44	4.8	3.87
Sayan	16	21	1.41
Udhna	46	7.6	4.05
Varacha	139	14.2	12.23
Ved Road	24	5.1	2.11
Others	49	-	4.31
Total	1137		

Reduction in the number of freight trips by directly transporting goods from one phase of production to the other without transporting goods to the market area is an ideal solution to reduce the overall goods movement in the city. Several attempts have been made in this regard by a local municipal body. It discouraged the delivery of goods to the market area by increasing parking charges for commercial vehicles. Strict time frames for the movement of medium and heavy commercial vehicles were established in many areas of the city by the traffic control department. A special transportation hub was created in the periphery of the city for the collection and distribution of textile goods. Though these steps were taken to improve the efficiency of city traffic and transportation facilities, they were not welcomed by the stakeholders of the textile industry. Weavers, processors, and traders' associations jointly opposed this move as their business was adversely affected. Since the industry is highly unorganized and there

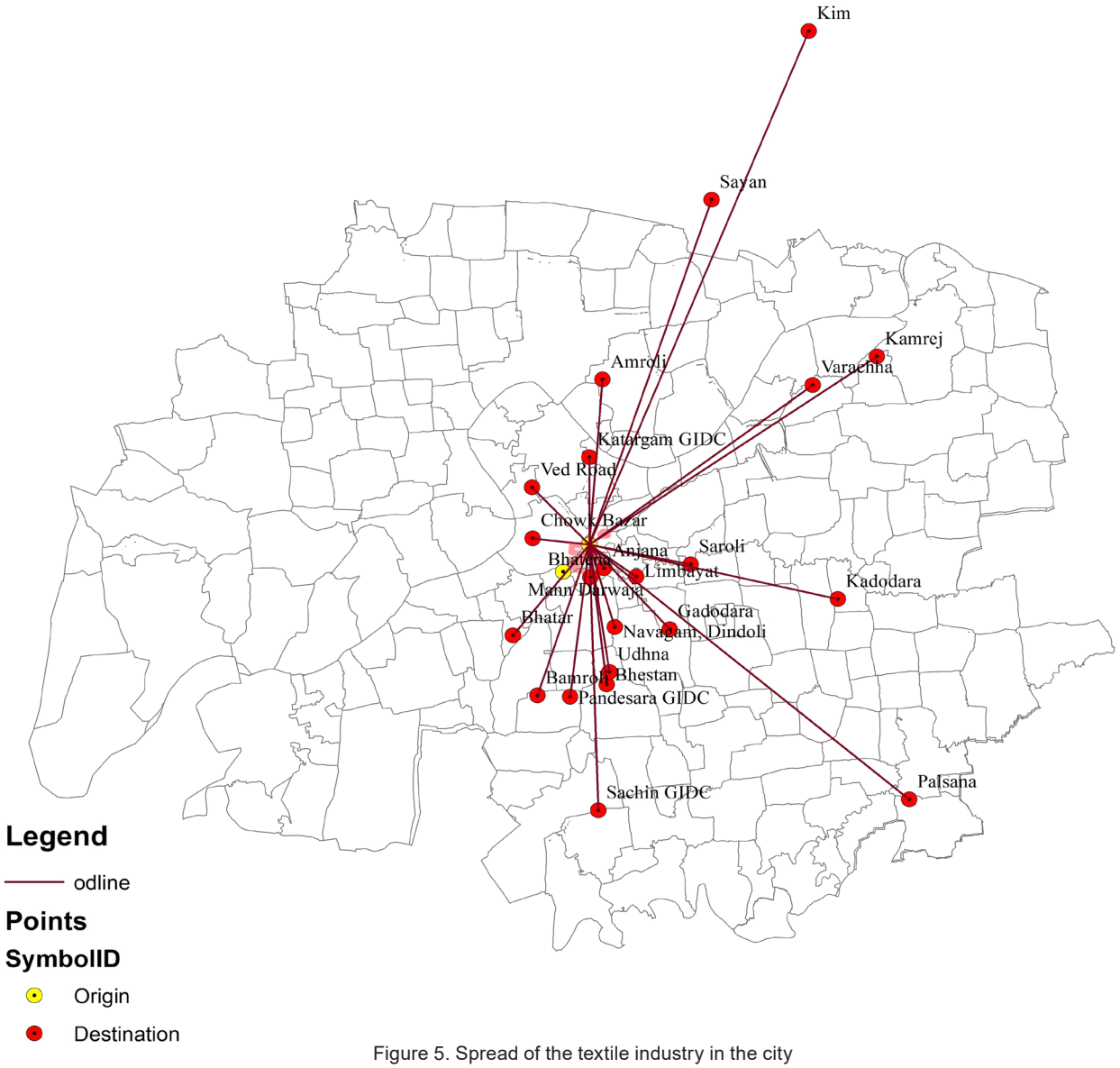

Figure 5. Spread of the textile industry in the city
Source: Own work

are thousands of people involved at various stages of production and distribution of goods in the textile industry, it is quite difficult to change the pattern of goods movement in the industry. Due to continued protest by the textile industry community, parking charges were gradually reduced. In the interest of the growth and development of the textile industry, which is one of the biggest economic forces in the city, regulatory measures related to inhibiting the goods movement, which might affect the functioning of the industry, were discouraged.

To estimate the reduction in freight trips due to sharing, trips are calculated based on the factors affecting trip generation. The number of trips generated depends on the total number of weaving machines, the total floor area, and the total number of employees at the unit, as well as the type and capacity of the vehicle used for freight transportation. Using the data collected, we developed a multi-linear regression model for freight trips based on the above dependent variable. The trip generation model for a power loom unit is as follows:

$$T = 0.6438 + (0.0652 * N_{pm}) + (0.0044 * A) + (0.1120 * Ne), \quad (R^2 = 0.8293), \tag{1}$$

where:

T = trips generated per month (ea.),

N_{pm} = total number of machines at the unit (ea.),

A = total floor area of the unit (sq. m),

Ne = total number of employees at the unit (people).

Considering the aggregate data in the power loom industry obtained from various sources, we found that there are 650,000 power loom machines installed in the city. Based on the survey data, the average area of one unit is 970 sq. m and the number of employees calculated as per the thumb rule is 1 per 12 machines per shift of 12 hours. The number of the generated freight trips estimated using the above equation is approx. 8850 if all freight trips are shared and freight vehicles are used at their full capacities only. Such trips are generated only for transporting raw fabric to processing units or to the market. According to the survey results, at least 4 internal trips are generated during the manufacturing phase. Hence, a minimum of 35,000 trips is expected due to the internal goods movement during their manufacturing. Considering 4.44 additional km to deliver goods in the city of Surat due to its sprawl, a net addition of CO2 emissions is calculated below. Yet again, these are just the bare minimum addition considering the textile industry alone. There would be other trips generated due to service and maintenance requirements, which are not considered in this study. The calculation is based on unitary emissions (g/km) from vans and trucks, provided by the Indian Emissions Regulations (Automotive Research Association of India (ARAI), 2018). According to the Bharat Stage VI (BS-VI) Emission Standards, the threshold value of CO emissions for a diesel vehicle is 1 gm/km. For 35,000 freight trips with extra 4.44 km (on average), CO2 emissions are supposed to increase by 56,210 kg (56.21 tons) per annum.

Results

As a result of the in-depth industry analysis in terms of the pattern of goods movement, we found that the manufacturing process and supply chain in the textile industry are overly complex due to scattered locations of processing units in the city. Different manufacturing phases are carried out at different clusters specialized in a particular value addition process, and each independent phase increases the movement of semi-finished goods manifold, thereby increasing the overall number of trips per unit of goods manufactured. According to estimates, a unit of fabric makes 7 internal trips before reaching its final distribution point. For 4–5 of the above trips, the wholesale market (ring road) area is either the origin or destination location, while the other point (destination or origin point, respectively) is located across the city or, in some cases, is in the city area. Besides, due to trading activity in the market area, many internal trips are generated here.

Hence, the ring road area occupying approx. 3 sq. km experiences an exceedingly high number of incoming and outgoing freight trips. Due to the municipal restrictions imposed on heavy commercial vehicles' movement in the major residential and commercial belts of the city, most of the internal goods movement in the textile industry is carried out by LCVs and three-wheeler carriers. This can also be confirmed by the category-wise vehicle count carried out in the ring road area. It was found that the average trip length for freight vehicles had increased from 6.73 km in 2008 to 11.17 km in 2018. This is basically due to the relocation of production units to the outskirts and suburban areas due to the urban sprawl.

Conclusions

There is a need for a holistic planning approach towards urban freight movement and related urban infrastructure for sustainable freight flows. This can serve as a policy framework to decide on the location of a logistics hub or as guidelines to allocate manufacturing enterprises in the proximity of the urban area. An incentive mechanism can also be added as a corresponding cost-effective measure. However, according to the early estimates of approx. 30% of the city's textile-related freight trips taking place within the ring road market area, it is advisable to provide a central warehousing facility for the area through collaborative efforts of the industry and the Municipal Corporation. We calculated the net additional emissions of CO_2 generated by an increase in the distances traveled by vans and trucks to reach their final destinations. However, our calculations are quite general, and more accurate

estimates are required with account for particular transport organizations and temporal changes. This research is ongoing. We have reached a general conclusion regarding the approximate amount of CO_2 generated by urban sprawl. More detailed research is needed with regard to the industry and its ancillaries sprawling in metropolitan areas and sprawl impacts on the distance traveled. The location patterns of textile manufacturing facilities and corresponding temporal changes should be closely compared with those in other major industries in the city.

Acknowledgments

We would like to thank the Surat Municipal Corporation (SMC), the Surat Urban Development Authority (SUDA), and the Regional Office of the Textile Commissioner in Surat for sharing information about the history of the textile industry in Surat city. We are also thankful to various textile weavers' associations, as well as owners and operators of the weaving and trading units located in several clusters across Surat city for participating in the establishment survey and sharing their data with us.

Funding

The paper was prepared as part of the PhD studies without any funding from any government or non-government organization.

References

Automotive Research Association of India (ARAI) (2018). *Indian Emissions Regulations.* [online] Available at: https://www.araiindia.com/pdf/Indian_Emission_Regulation_Booklet.pdf [Date accessed 15.03.2021].

Aljohani, K. and Thompson, R. G. (2016). Impacts of logistics sprawl on the urban environment and logistics: Taxonomy and review of literature. *Journal of Transport Geography*, Vol. 57, pp. 255–263. DOI: 10.1016/j.jtrangeo.2016.08.009.

Dablanc, L., Ogilvie, S. and Goodchild, A. (2014). Logistics sprawl: differential warehousing development patterns in Los Angeles, California, and Seattle, Washington. *Transportation Research Record: Journal of the Transportation Research Board*, Vol. 2410, Issue 1, pp. 105–112. DOI: 10.3141/2410–12.

Dablanc, L. and Rakotonarivo, D. (2010). The impacts of logistics sprawl: How does the location of parcel transport terminals affect the energy efficiency of goods' movements in Paris and what can we do about it? *Procedia - Social and Behavioral Sciences*, Vol. 2, Issue 3, pp. 6087–6096. DOI: 10.1016/j.sbspro.2010.04.021.

Dablanc, L. and Ross, C. (2012). Atlanta: a mega logistics center in the Piedmont Atlantic Megaregion (PAM). *Journal of Transport Geography*, Vol. 24, pp. 432–442. DOI: 10.1016/j.jtrangeo.2012.05.001.

Directorate of Census Operations (2011). *Census of India, Gujarat. Series 25, Part XII-B. District Census Handbook. Surat.* Gujarat: Directorate of Census Operations, 415 p.

Diziain, D., Ripert, C. and Dablanc, L. (2012). How can we bring logistics back into cities? The case of Paris metropolitan area. *Procedia - Social and Behavioral Sciences*, Vol. 39, pp. 267–281. DOI: 10.1016/j.sbspro.2012.03.107.

Government of Gujarat (2017). *Vibrant Gujarat Global Summit Report.* Government of Gujarat, India.

Lindholm, M. and Behrends, S. (2012). Challenges in urban freight transport planning – a review in the Baltic Sea Region. *Journal of Transport Geography*, Vol. 22, pp. 129–136. DOI: 10.1016/j.jtrangeo.2012.01.001.

Sakai, T., Kawamura, K. and Hyodo, T. (2015). Locational dynamics of logistics facilities: Evidence from Tokyo. *Journal of Transport Geography*, Vol. 46, pp. 10–19. DOI: 10.1016/j.jtrangeo.2015.05.003.

Surat Urban Development Authority (SUDA) (2017). *Development Plan 2035.* [online] Available at: https://www.sudaonline.org/wp-content/uploads/2017/03/SUDA-DP-2035-report-final-22.02.2017.pdf [Date accessed 11.02.2021].

Surat Urban Development Authority (SUDA) (2018). *Comprehensive Mobility Plan Surat 2046.* Surat, India.

Taniguchi, E., Thompson, R. G. and Yamada, T. (2016). New opportunities and challenges for city logistics. *Transportation Research Procedia*, Vol. 12, pp. 5–13. DOI: 10.1016/j.trpro.2016.02.004.

Toilier, F., Serouge, M., Routhier, J.-L., Patier, D. and Gardrat, M. (2016). How can urban goods movements be surveyed in a megacity? The case of the Paris region. *Transportation Research Procedia*, Vol. 12, pp. 570–583. DOI: 10.1016/j.trpro.2016.02.012.

Transportation Research Board of the National Academies (2012). *NCHRP Report 739 and NCFRP Report 19. Freight Trip Generation and Land Use.* Washington DC: Transportation Research Board, 150 p.

Woudsma, C., Jakubicek, P. and Dablanc, L. (2016). Logistics sprawl in North America: methodological issues and a case study in Toronto. *Transportation Research Procedia*, Vol. 12, pp. 474–488. DOI: 10.1016/j.trpro.2016.02.081.

Technique and Technology
of Land Transport in Construction

DOI: 10.23968/2500-0055-2021-6-2-63-69

SELECTING MADIUN–DOLOPO TRACE ROUTE WITH THE FUZZY AHP (*ANALYTIC HIERARCHY PROCESS*) METHOD

Septiana Widi Astuti*, Muhammad Adib Kurniawan, Adya Aghastya

Politeknik Perkeretaapian Indonesia
Indonesia

*Corresponding author: septiana@ppi.ac.id

Abstract

Introduction: The National Railway Master Plan (RIPNAS), dated 2018, mentions that the railway network size and railway service capacity for using trains as the main means of transportation can be increased by reactivating non-operational routes and improving the condition of the existing routes. **Methods**: In our study, we propose the Fuzzy Analytic Hierarchy Process (Fuzzy AHP) method to determine the best option for the reactivated Madiun–Dopolo trace route in East Java, Indonesia. The data obtained were derived from questionnaires filled in by experts in the field. The model used six main criteria: land use, technical aspects, transportation node integration, social insecurity, disaster factors, and funding. **Result and Discussion**: The analysis reveals that the predominant route selection criterion chosen by the respondents was the Land Use (with a score of 0.25). The least significant Madiun–Dopolo route selection criterion was the Disaster Factors (0.07). Based on the results of weighting the criteria and aggregating the respondent alternatives, the trace route most commonly chosen by the respondents was the Alternative Trace Route (Trace Route 2), with a score of 0.698, while the Existing Trace Route (Trace Route 1) had a score of 0.302. The Alternative Trace Route is longer than the Existing Trace Route, but it will mostly pass through farming regions, which is assumed to create less social conflicts than in the case of Trace Route 1. This also automatically means that Trace Route 2 will need fewer funds in land acquisition.

Keywords

Fuzzy Analytic Hierarchy Process, route, railway.

Introduction

In 2018, the number of passenger and freight train users rose by 7.54 and 12.92% respectively compared with the previous year. Such an increase must be followed by the enhancement of facilities and infrastructure services. The National Railway Master Plan (RIPNAS), dated 2018, mentions that the railway network size and railway service capacity for using trains as the main means of transportation can be increased by reactivating non-operational routes and improving the condition of the existing routes. One example is the Madiun–Ponorogo railway, which is expected to be reactivated and launched between 2025 and 2030.

The Madiun–Ponorogo railway has not been active since 1984, when it was used for distributing goods as well as passengers. This railway route links Madiun City in Madiun Regency and Slahung District, Ponorogo Regency. There are two major sugar factories along the route.

Ministerial Regulation No. 11 of 2012, which concerns the procedure of determining railway routes, defines a trace route as a railway track layout with known coordinates. The arrangement of a railway trace route becomes a guideline for performing technical design activities, analyzing the environmental impact, and actualizing the land before building the railway.

The Analytical Hierarchy Process (AHP) is a popular method for tackling multi-criteria analysis problems involving qualitative data (Saaty, 1980). This method uses unique mathematical procedures to process single or multiple subjective preferences, based on pairs of factors, helping relevantly rate and analyze decisions (Saaty and Vargas, 2012). In most cases, the individuals who take part in the rating process are experts in particular fields. The AHP has already been used for studying the alternative development of the railway trace route to NYIA Indonesia airport. The results showed that the prior trace route had the potential of social conflict and did not comply with the new master plan of the airport (Chasanah and Putro, 2018). Mohajeri and Amin (2010) used the methods of the AHP and data

envelopment analysis (DEA) to find the optimum site for a railway station in the city of Mashhad, Northeast Iran. They identified a four-level hierarchy model for the railway station site selection problem. The model used four main criteria: rail-related, passenger services, architecture and urbanism, and economics (Mohajeri and Amin, 2010).

The Fuzzy AHP combines analysis using the AHP method and the fuzzy approach concept. The fuzzy method includes subjective criteria that can compensate for the weaknesses of the AHP method. The fuzzy theory helps to deal with the subjective ratings made by humans who use language or linguistic methods (Chang, 1996). Buckley (1985) extended Saaty's AHP to the case where the evaluators are allowed to employ fuzzy ratios in place of exact ratios, to address difficulties with assigning exact ratios when comparing two criteria and derive the fuzzy weights of criteria through the geometric mean method.

The applications of the Fuzzy AHP have been well-documented in construction management literature, especially literature on project site selection. Yu and Liu (2012) proposed a FAHP model to select the most suitable projects among multiple sites for safety improvement. With the Fuzzy AHP model, they were able to capture the comprehensive impacts of all contributory factors that are usually neglected by most other existing single- or multi-criteria approaches during the safety project selection process (Yu and Liu, 2012).

The Fuzzy AHP was also used by Peetawan and Suthiwartnarueput (2018) to identify factors affecting the success of rail infrastructure development projects contributing to Thailand's logistics platform. The projects addressed in the study included double-tracking the existing railways and constructing new routes. It was found that a rail development master plan has the highest influence on a project's success.

Based on the background above, we are interested in studying the selection of the most suitable Madiun–Dolopo railway trace route with the Fuzzy AHP method. In the future, we expect that this study can contribute to selecting the best trace route when planning the reactivation of the Madiun–Dopolo Railway.

Table 1. Fuzzy numbers used for making qualitative assessments

Fuzzy numbers	Membership function
1	(1,1,3)
x	(x-2,x,x + 2) f or x = 3,5,7
9	(7,9,11)

$$S_i = \frac{\sum_{j=1}^{m} \mu_i^j}{\sum_{i=1}^{n} \sum_{j=1}^{m} \mu_i^j}, i = 1,2,...,n \quad (1)$$

FUZZY ANALYTIC HIERARCHY PROCESS

The Fuzzy AHP is designed to solve the problems of making multi-criteria decisions while working with subjective ratings. The Fuzzy AHP is considered to be better in describing uncertain decisions than the AHP (Buckley, 1985). The first Fuzzy AHP method was proposed by Van Laarhoven and Pedrycz (1983), who used the Triangular Fuzzy Numbers (TFNs) in the comparison pairs of a matrix. Within the Fuzzy AHP, the comparison of both the criteria and the alternatives can be done through linguistic variables, represented by triangular numbers (Emrouznejad and Ho, 2018). The scale of linguistic variables within the AHP, as applied by Saaty (1991), ranges from 1 to 9. It is then converted to fuzzy form using the Triangular Fuzzy Numbers. These Triangular Fuzzy Numbers can be denoted by (l, m, u) (Chang, 1996). It is easier to show the fuzzy problem by using the Triangular Fuzzy Numbers rather than the interval number (Zhang and Liu, 2010). Fuzzy numbers used for making qualitative assessments are listed in **Table 1** (Deng, 1999).

Consistency Index (CI)

An important measure of consistency for pairs of expert judgment comparisons is the consistency ratio (CR) (Saaty, 1980). The steps in the Fuzzy AHP Consistency test (Saaty, 2010) are to find the max value of λ, followed by finding the CR, which is determined by Eq. (2).

$$CI = \frac{\lambda_{max} - n}{n-1}, \quad (2)$$

where *CI* = consistency index, n = size of matrices < λ, max = maximum or principal Eigen value of the judgment matrix.

The CI is modified into the Consistency Ratio (CR), which is CR = CI/RI (RI = Random Index, based on the size of matrices n). Saaty (1980) suggested that the value of the CR should not exceed 0.1 for a confident result.

Methods

We began our study by reviewing literature, such as journals and scientific articles, in order to gain supporting references. Data collection involved primary and secondary data. Primary data included the results of the survey on the condition of the Existing Madiun–Dopolo Trace Route (Trace Route 1) and Alternative Madiun–Dopolo Trace Route (Trace Route 2) and the results from the questionnaires. In turn, secondary data included the neighborhood map and the hamlet document of the Ministry of Madiun City and Regency, as well as the map of the existing Madiun–Dopolo railway. For collecting the data samples, we used the purposive sample method. A purposive sample is a non-probability sample that is based on the segment of the population with the most information on the characteristic of interest and the objective of the study (Guarte and Barrios, 2006).

After gaining these data, we then followed up with

data management, which was done by using the Fuzzy AHP method with the help of Microsoft Excel.

Below are the steps of data management (Buckley, 1985; Chang, 1996; Tzeng and Huang, 2011) Figure 1:

a. Create a three-level hierarchical structure model, as shown in Fig. 1.
   Level 1 indicates the target;
   Level 2 indicates criteria to ease decision-making;
   Level 3 indicates the railway trace route options.
b. Construct matrix comparison pairs among all the elements/criteria in the dimensions of the hierarchy system, using the TFN scale.

$$\begin{bmatrix} (1,1,1) & \tilde{a}_{12} & \cdots & \tilde{a}_{1n} \\ \tilde{a}_{21} & (1,1,1) & \cdots & \tilde{a}_{2n} \\ \vdots & \vdots & \ddots & \vdots \\ \tilde{a}_{n1} & \tilde{a}_{n2} & \cdots & (1,1,1) \end{bmatrix}. \quad (3)$$

c. Define the fuzzy geometric mean and fuzzy weights for each criterion, using the geometric mean technique by Buckley (1985), as follows:

$$\tilde{r}_i = \left(\tilde{a}_{i1} \otimes \tilde{a}_{i2} \otimes \ldots \otimes \tilde{a}_{in}\right)^{1/n}; \quad (4)$$

$$\tilde{w}_i = \tilde{r}_i \otimes \left(\tilde{r}_1 \otimes \ldots \otimes \tilde{r}_n\right)^{-1}, \quad (5)$$

where $\tilde{a}_{in}$ is the value of fuzzy comparison of criterion i to criterion n, thus, $\tilde{r}_i$ is the geometric mean value of fuzzy comparison between criterion i and each criterion, $\tilde{w}_i$ is the fuzzy weight of the i^{th} criterion, $\tilde{w}_i = (l_i, m_i, u_i)$ are the lower, middle and upper values of the fuzzy weight of the i^{th} criterion.

d. Calculate the fuzzy weight that has been defuzzified by each matrix comparison pair. The fuzzy weight vector of each criteria was calculated by dividing the minimum degree of possibility by the summation of the minimum degree of possibility:

$$w_i = \frac{MinP_i}{\sum_i^n MinP_i}, i = 1, 2, \ldots, n. \quad (6)$$

e. Calculate the defuzzy weight with the Center of Area Method.

$$M_i = \frac{lw_i + mw_i + uw_i}{3}. \quad (7)$$

f. Normalize the fuzzy weight vector.

$$N_i = \frac{M_i}{\sum_{i=1}^n M_i}. \quad (8)$$

g. Calculate the value of the Consistency Index (CI) and Consistency Ratio (CR).
h. Calculate the alternative weight. The steps for calculating the alternative weight are the same as for calculating the criteria weight, but each alternative must be compared with each criterion (6 criteria).
i. Rank the fuzzy number and interpret the calculation results and draw conclusions.

Results and Discussion

The aim of this study was to obtain the right option to meet a specific goal (selection of the Madiun–Dolopo railway trace route). The options were based on the criteria determined. We followed up on our literature overview by spreading questionnaires for data collection. The questionnaires were then analyzed using the Fuzzy AHP method with the help of Microsoft Excel.

a. General Description of Respondents

There were seven respondents involved in the study: functionaries of the Madiun City and District Transportation Office, functionaries of the Madiun Regency Development Planning Agency at Sub-National Level, functionaries of PT.KAI DAOP 7 Madiun, and lecturers in the railways field. These respondents were considered to be involved and competent in determining the policy and technicalities of railway construction. The general description of the respondents includes their position, latest education, and period of working experience in the field. The

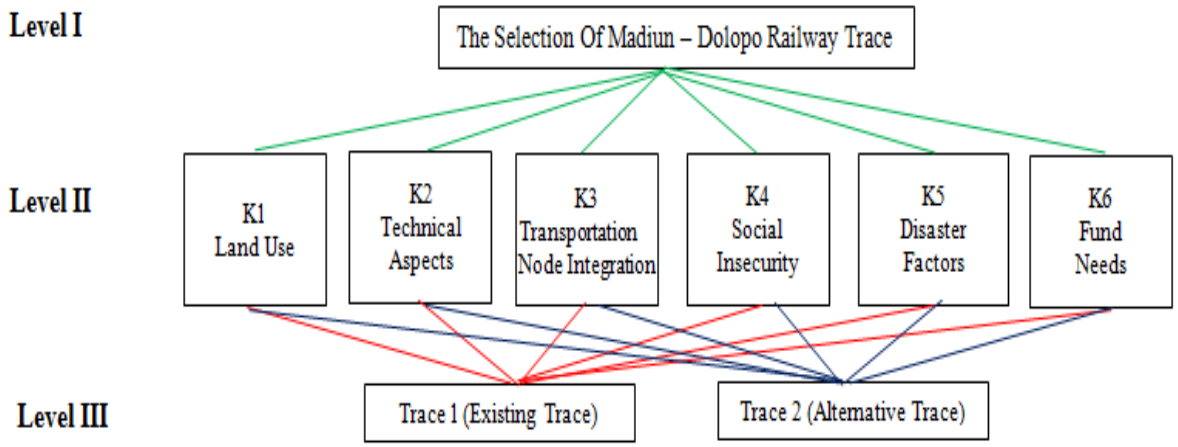

Figure 1. Hierarchical structure of the trace route selection process

respondents' education level represents two stages of education: 42.86% of the respondents hold a Bachelor's degree (S1) and 57.14% hold a Master's degree (S2). In terms of working experience, the respondents can be divided into three groups: 57.14% have 1–10 years of experience, 28.57% have 10–20 years of experience, and 14.29% have over 20 years of experience.

b. Existing Trace Route (Trace Route 1)

The existing trace route, with the total length of 18 km, is divided into three parts: Madiun Station–Kanigoro Station (7 km), Kanigoro Station–Pagotan Station (5 km), and Pagotan Station–Dopolo Station (6 km), with at-grade construction and fairly flat topography. There are 19 curves in total along Trace Route 1. Based on the observation results, the railways between Madiun Station and Dopolo Station have mostly deteriorated, and the location is utilized by citizens as a populous settlement. Some of the rail tracks can still be seen in some small areas, yet they cannot be used due to wear and tear as well as corrosion. The land between Madiun Station and Dopolo Station is predominantly used for settlements, shop complexes, graveyards, and even government buildings. We can classify the land use as follows: 87,331.8 m^2 for rice fields, 368,188 m^2 for settlements, 580.6 m^2 for public graveyards, and 9864.8 m^2 for farming.

c. Alternative Trace Route (Trace Route 2)

The proposed alternative trace route is 23+250 km further and longer compared with the existing trace route, with at-grade construction and fairly flat topography. There are 15 curves in total along Trace Route 2. This trace route passes from Madiun Station to Sukosari, then heads to rice field areas, which end at the border of Kanigoro Station. After that, it mostly passes through more rice fields and ends at Dopolo Station. The land use is allocated as follows: about 439,660.8 m^2 for rice fields and about 368,188 m^2 for citizen settlements.

d. Weighting Criteria

The process of determining the priorities of railway trace route selection was structured by decomposing the relevant problems in order to picture the influence factors along with the alternative decisions, arranged in the form of hierarchy. All elements within the decision structure have different intensities, in order to give impact to the goal. This study includes six criteria that need to be considered when selecting the trace route: land use (K1), technical aspects (K2), transportation node integration (K3), social insecurity (K4), disaster factors (K5), and funding (K6). The Land Use aspect became one of the criteria for selecting the trace route; its indicator is a percentage ratio of the railway trace route that passes through a specific region/land to the total length of the railway trace route (%) (Palayukan and Adisasmita, 2018). In our study, we based the Land Use indicator on the area of rice fields, settlements, public graveyards, farmlands, and rivers that might be affected by the activity of the railway. In turn, the Technical Aspects indicator included the trace route length, the total number of curves, the types of construction used, and topography. The Transportation Node Integration aspect was related to the distance between the planned station and the terminal. Social risk, defined as the severity and uncertainty of an activity with respect to human values, which may influence the whole society and lead to social unrest (Aven and Renn, 2009), was prevalent. The Social Insecurity aspect referred to the possible social conflict that might occur, for instance, if the economic compensation of land acquisition and housing demolition was not handled properly (Yang and Kuang, 2019), as well as to resistance against the reactivation plan. The Disaster Factors aspect pertained to the regions or areas with potential of natural disaster that were traversed by the trace route; such factors included geology, hydrometeorology, or even geotechnical factors. The Disaster Factors that we calculated in this study were the factors of flooding from nearby areas over the last 20 years. The results from observing the area around the existing and alternative trace routes showed that the area is safe from prolonged floods. The last criterion (Funding) is related to the estimated funds needed for route reactivation, from the design phase to the execution phase. These could be the funds for both technical and non-technical activities, especially land acquisition.

e. Calculation of Weighting Criteria

In the Fuzzy AHP, the assessment (preferences) of decision-making under conditions of uncertainty is modeled by using logical fuzzy operations (Chang, 1996). Similar to the conventional AHP, the information within the Fuzzy AHP was obtained in the form of matrix comparison pairs. According to Deng (1999), fuzzy numbers are used for making qualitative assessments.

Table 2. Triangular Fuzzy Numbers for Likert Scale

Definition of linguistic variables	Likert Scale	TFN	Likert Scale	TFN
Similar importance	1	(1,1,3)	1/1	(1/1,1/1,1/3)
	2	(1,2,4)	½	(1/4,1/2,1/1)
Moderate importance	3	(1,3,5)	1/3	(1/5,1/3,1/1)
	4	(2,4,6)	¼	(1/6,1/4,1/2)
Intense importance	5	(3,5,7)	1/5	(1/7,1/5,1/3)
	6	(4,6,8)	1/6	(1/8,1/6,1/4)
Demonstrated importance	7	(5,7,9)	1/7	(1/9,1/7,1/5)
	8	(6,8,10)	1/8	(1/10,1/8,1/6)
Extreme importance	9	(7,9,11)	1/9	(1/11,1/9,1/7)

The stages of weighting criteria were defined by creating a matrix comparison. The weight value of each criterion was determined by using pair comparison questionnaires. We then continued by searching for the geometric mean values, derived from the value of fuzzy comparison (Ri). The process is explained below in **Table 3.**

Table 3. Value of Geometric Means from Criteria

Criteria	R_i		
	1	m	u
K1	1.814	2.67	3.502
K2	1.487	2.263	3.067
K3	1.582	2.515	3.595
K4	0.576	0.92	1.385
K5	0.464	0.696	1.113
K6	0.813	1.407	2.074
Total	6.735	10.471	14.736
Inverse	0.148	0.096	0.068
Increasing Order	0.068	0.096	0.148

After finding the value of R_i, the next stage was to determine the relative fuzzy weight of the criteria (W_i), as explained in **Table 4.**

The next table (**Table 5**) shows the value of M_i and N_i, which is the weight of the criteria after normalization.

After finding the weighting value, the next stage was to calculate the Consistency Ratio (CR), based on the Eigen value (λ), the maximum Eigen value (λmax), and the Consistency Index (CI). The calculation results can be seen in **Table 6**

Table 4. Relative Fuzzy Weight of Criteria

Criteria	Wi		
	l	m	U
K1	0.12	0.26	0.52
K2	0.10	0.22	0.46
K3	0.11	0.24	0.53
K4	0.04	0.09	0.21
K5	0.03	0.07	0.17
K6	0.06	0.13	0.31

Table 5. Relative Fuzzy Weight of Criteria

Criteria	M_i	N_i	(%)
K1	0.30	0.25	24.64
K2	0.26	0.21	21.19
K3	0.29	0.24	24.18
K4	0.11	0.09	9.13
K5	0.09	0.07	7.22
K6	0.17	0.14	13.65
Total	1.21	1.00	100

Table 6. Results of *Eigen* Value Calculation

Criteria	Total	Weight	Eigen Value
K1	1.814	0.246	7.362
K2	1.487	0.212	7.016
K3	1.582	0.242	6.542
K4	0.576	0.091	6.313
K5	0.464	0.072	6.428
K6	0.813	0.136	5.957
		Eigen Max	6.603

Based on the table above, the values of CI and CR were obtained as follows:

$$CI = \frac{\lambda_{max} - n}{n-1} = \frac{6.603 - 6}{6-1} = 0.121, \quad (9)$$

with R_i for n = 6, which is 1.24, we then obtained $CR = \frac{CI}{RI} = 0.121/1.24 = 0.0973.$ Since the value of CR is smaller, we can conclude that the results from the data used are consistent and do not require decision-making i mprovement.

f. Alternative Weighting

Our alternative weighting calculations used the same stages as criteria calculations, but with one addition: alternative weighting needed to be compared with each criterion. In other words, this analysis was repeated six times for each existing criterion. The alternative weighting was derived from the results of the respondents' assessments in the questionnaires. We conducted a test on normalizing the data after obtaining the weighting value from pair comparison. In order to achieve the best alternative, the weighting totaling was based on the normalized data. We reached the final decision through developing priority weights for the six criteria (K1, K2, K3, K4, K5, K6) with the two alternatives (Trace Route 1, Trace Route 2) to reach the overall objective, as mentioned in **Table 7**.

In line with the goal (obtaining the best criteria for trace route selection), the Land Use criterion achieved the highest value of priority weight compared with the other five criteria: 25%. On the other hand, the Disaster Factors criterion achieved the lowest value of priority weight, 7%. According to the disaster factor survey, which shows the factors of flooding over the last 20 years, the areas close to both the existing railway and the alternative railway are safe from prolonged floods. Therefore, this aspect achieved the lowest value of priority weights among all other aspects.

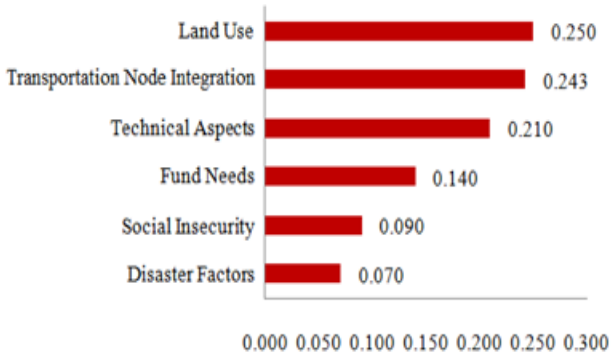

Figure 3. Diagram of Weighting Criteria

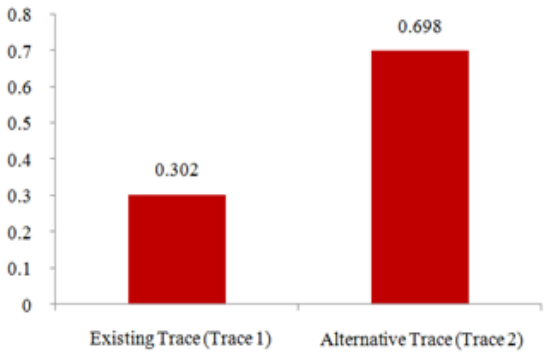

Figure 4. Diagram of Best Altemative

Table 7. Combination of Priority Weights

Criteria	Weights	Trace 1	Trace 2
K1	0.250	0.202	0.798
K2	0.210	0.324	0.676
K3	0.243	0.448	0.552
K4	0.090	0.224	0.776
K5	0.070	0.429	0.571
K6	0.140	0.195	0.805

Table 8. Alternative Weighting

Criteria	Weights	
	Trace Route 1	Trace Route 2
Land Use	0.202	0.798
Technical Aspects	0.324	0.676
Transport Node Integration	0.448	0.552
Social Insecurity	0.224	0.776
Disaster Factors	0.429	0.571
Funding	0.195	0.805
Total	0.302	0.698

As stated in **Table 8** above, the values of the alternative trace route are higher in every criterion. We ordered the criteria from the highest down to the lowest: Funding, Land Use, Social Insecurity, Technical Aspects, Disaster Factors, and Transport Node Integration. Trace Route 1 needs less funding for technical activities because there are still some remaining functional railways, with a shorter trace than Trace Route 2. However, the funding needed for land acquisition is higher because of the greater requirements for demolishing settlements and other buildings as compared with Trace Route 2, which mostly passes through farming fields.

Based on the total responses with relation to weighting criteria and the alternative, the most frequently chosen Madiun–Dopolo railway trace route option was the Alternative Trace Route (Trace 2 Route), with a score of 0.698. The least frequently chosen option was the Existing Trace Route (Trace Route 1), with a score of 0.302.

Conclusion

Based on the analysis done, there are several conclusions to be drawn, as follows:

a) According to the Fuzzy AHP calculations, the most influential criterion for selecting railway trace routes chosen by the respondents is the Land Use criterion (0.25). The least influential criterion is the Disaster Factors criterion (0.07).

b) The railway trace route most favored by the respondents is the Alternative Trace Route (Trace Route 2) (0.0698), while the Existing Trace Route (Trace Route 1) was favored less (0.302). Even though the Alternative Trace Route is longer than the Existing Trace Route, it will mostly pass through farming regions, which is assumed to create less social conflicts than in the case of Trace Route 1. This also automatically means that Trace Route 2 will need fewer funds in land acquisition.

References

Aven, T. and Renn, O. (2009). On risk defined as an event where the outcome is uncertain. *Journal of Risk Research*, Vol. 12, Issue 1, pp. 1–11. DOI: 10.1080/13669870802488883.

Buckley, J. J. (1985). Fuzzy hierarchical analysis. *Fuzzy Sets and Systems*, Vol. 17, Issue 3, pp. 233–247. DOI: 10.1016/0165–0114(85)90090–9.

Chang, D.-Y. (1996). Applications of the extent analysis method on fuzzy AHP. *European Journal of Operational Research*, Vol. 95, Issue 3, pp. 649–655. DOI: 10.1016/0377–2217(95)00300–2.

Chasanah, F. and Putro, A. A. H. (2018). Studi Alternatif Pengembangan Trase Jalur Kereta Api DAOP VI Yogyakarta Menuju NIYA Kulon Progo. *Jurnal Teknologi Rekayasa*, Vol. 3, No. 1, pp. 79–88. DOI: 10.31544/jtera.v3.i1.2018.79–88.

Deng, H. (1999). Multicriteria analysis with fuzzy pairwise comparison. *International Journal of Approximate Reasoning*, Vol. 21, Issue 3, pp. 215–231. DOI: 10.1016/S0888–613X(99)00025–0.

Emrouznejad, A. and Ho, W. (2018). *Fuzzy analytic hierarchy process*. Boca Raton: CRC Press, 430 p.

Guarte, J. M. and Barrios, E. B. (2006). Estimation under purposive sampling, *Communications in Statistics — Simulation and Computation*, Vol. 35, Issue 2, pp. 277–284. DOI: 10.1080/03610910600591610.

Mohajeri, N. and Amin, G. R. (2010). Railway station site selection using analytical hierarchy process and data envelopment analysis. *Computers & Industrial Engineering*, Vol. 59, Issue 1, pp. 107–114. DOI: 10.1016/j.cie.2010.03.006.

Palayukan, R. O. and Adisasmita, S. A. (2018). Analisis Pemilihan Trase Jalur Kereta Api (Studi Kasus : Tanah Grogot — Batulicin – Pelaihari), pp. 146–154.

Peetawan, W. and Suthiwartnarueput, K. (2018). Identifying factors affecting the success of rail infrastructure development projects contributing to a logistics platform: A Thailand case study. *Kasetsart Journal of Social Sciences*, Vol. 39, Issue 2, pp. 320–327. DOI: 10.1016/j.kjss.2018.05.002.

Saaty, T. L. (1980). *The Analytic Hierarchy Process*. New York: McGraw-Hill, 287 p.

Saaty, T. L. (2010). Decision making with the analytic hierarchy process. *International Journal of Services Sciences*, Vol. 1, No. 1, pp. 83–98. DOI: 10.1504/IJSSCI.2008.017590.

Saaty, T. L. and Vargas, L. G. (2012). *Models, methods, concepts & applications of the Analytic Hierarchy Process.* 2nd edition. London : Springer, 346 p.

Tzeng, G.-H. and Huang, J.-J. (2011). *Multiple attribute decision making. Methods and applications*. New York: CRC Press, 352 p.

Van Laarhoven, P.J.M. and Pedrycz, W. (1983). A fuzzy extension of Saaty's priority theory. *Fuzzy Sets snd Systems*, Vol. 11, Issues 1–3, pp. 229–241. DOI: 10.1016/S0165–0114(83)80082–7.

Yang, J. and Kuang, X. (2019). Social risk assessment of engineering project based on ordered voting model. *IOP Conference Series: Materials Science and Engineering*, Vol. 688, Issue 5, article 055033. DOI: 10.1088/1757–899X/688/5/055033.

Yu, J. and Liu, Y. (2012). Prioritizing highway safety improvement projects: A multi-criteria model and case study with SafetyAnalyst. *Safety Science*, Vol. 50, Issue 4, pp. 1085–1092. DOI: 10.1016/j.ssci.2011.11.018.

Zhang, X. and Liu, P. (2010). Method for aggregating triangular fuzzy intuitionistic fuzzy information and its application to decision making. *Technological and Economic Development of Economy*, Vol. 16, Issue 2, pp. 280–290. DOI: 10.3846/tede.2010.18.

DOI: 10.23968/2500-0055-2021-6-2-70-76

STRUCTURAL CHANGES IN STRUCTURAL STEELS DURING THERMAL CYCLING

Valeriy Gordienko[1]*, Sergey Repin[1], Alexander Vorobiev[2], Angelica Abrosimova[1]

[1]Saint Petersburg State University of Architecture and Civil Engineering
Vtoraja Krasnoarmeyskaya st., 4, Saint Petersburg, Russia
[2]Emperor Alexander I St. Petersburg State Transport University
Moskovsky pr., 9, Saint Petersburg, Russia

*Corresponding author: val-gor@yandex.ru

Abstract

Introduction: During experimental studies of structural steels responsible for the reliability of metal structures used, for example, in hoisting and transporting machinery, we established a correlation between the magnetic parameter *Hp* and characteristic changes in the metal microstructure during thermal cycling. It is shown that the *Hp* parameter depends on the initial structural state of steel, the amount and mass fraction of alloying elements, and the number of heating/cooling cycles. **Methods:** We found that an increase in the number of heating/cooling cycles and the amount of alloying elements, as well as preliminary cold plastic deformation with stage-by-stage control of structural changes using passive magnetic flux leakage testing results in a finer-grained structure, which was confirmed by metallographic analysis. **Results:** The paper considers specifics of structural changes in steels with different initial structures during thermal cycling. It is shown that the final grain size depends on the number of treatment cycles, the amount of alloying elements, and the initial microstructure. It is the fine-grain structure that improves the most important performance characteristics of steels: strength, cyclic strength, and cold brittleness.

Keywords

Welded metal structures, structural steels, transport and special purpose vehicles, handling machinery, thermal cycling, structural changes, fine-grain structure, metallographic analysis, passive magnetic flux leakage testing, magnetic parameter *Hp*.

Introduction

Long-term use of a vast amount of welded metal structures, an increasing number of steel grades used to manufacture various structures of hoisting and transporting machinery, numerous studies to develop and improve new process solutions so as to guarantee the required behavior of metals — all of these are not sufficient to obtain valid data on the identification of reliable relations between the microstructure and the magnetic parameters of structural steels. To manufacture more reliable and safe welded metal structures used in various constructions and machinery, we need not only to use the existing ones properly but also to develop new, more accurate instruments and equipment as well as methods for monitoring and restoring their performance (Belyaev et al., 2020). It should be noted that in order to optimize material and labor input, reduce the cost of welded metal structures and products, it is necessary to perform non-destructive testing, including magnetic testing, at all stages of their manufacture, installation, operation and repair (Hetherington et al. 1987; Ranjan et al., 1987; Rautioaho et al., 1987; Tanner et al., 1988; Thompson and Tanner, 1993).

It becomes possible with passive magnetic flux leakage testing (Gordienko, 2020; Gordienko and Bardyšev, 2013; Gordienko et al., 2020). We used this method in our study to ensure stage-by-stage control of structural changes in structural steels having different initial microstructures during thermal cycling. Thermal cycling is one of the basic effective ways to obtain ultrafine-grain structures in metals and alloys with various degrees of dispersion, which is essential in civil and mechanical engineering since steels with a fine-grain structure are characterized by higher strength properties.

Heating/cooling cycles in thermal cycling treatment have the following effects on metal: significant rapid changes in temperature during heating/cooling, phase and structure transformations, interfacial and thermal stresses (Fedyukin and Smagorinsky, 1989; Maslakova, 1978; Porter and Dabkowski, 1973; Savitsky, 1971a, 1971b). However, different types of steel have different optimal thermal cycling conditions, which cannot be extended to other types of steel.

Methods

Taking the above into consideration, it was important to assess the capabilities of passive

magnetic flux leakage testing when monitoring the structural state of 08ps, 09G2S and 10KhSND structural steels during thermal cycling and attempt to establish a relationship between the magnetic properties and the structural state of the studied steels with different amounts of alloying elements during multiple thermal cycling. To study 08ps, 09G2S and 10KhSND structural steels having different initial structural states (as-received, as-received + high-temperature annealing at 900°C, and as-received + preliminary cold plastic deformation to a degree of 50%), laboratory samples were cut out, which subsequently were subjected to thermal cycling.

The changes in the initial structure of structural steels during thermal cycling were monitored using passive magnetic flux leakage testing. Magnetic measurements in terms of the strength of leakage magnetic field *Hp* were carried out with an IKNM 2-FP magnetometric stress concentration meter before the first and subsequent heating/cooling cycles of thermal cycling, and then diagrams of changes in the *Hp* parameter vs. the number of cycles were plotted.

To perform metallographic analysis, we used the following: a Brilliant 220 precision cutting machine to cut sections; an Opal 460 automatic press for hot pressing of the samples; a Saphir 560 grinding and polishing machine with a Rubin 520 programmable head to ensure automatic dosing of diamond suspensions and grinding to a pre-set depth. When polishing was completed, the samples were subjected to chemical etching before subsequent metallographic analysis.

We also used Carl Zeiss Axio Observer and Leica DMI 5000 metallographic microscopes to study the microstructure of the samples, displaying it on a screen.

The purpose of the study was to develop a method to obtain such a fine-grain structure of steels that would improve their most important performance characteristics: strength, cyclic strength, and cold brittleness.

Results

All steels under consideration had a common characteristic: during the first two heating/cooling cycles, the most noticeable changes in the magnetic parameter *Hp* occurred. During subsequent cycles, the magnetic amplitude decreased, and the *Hp* values tended to be minimum and close to each other, regardless of the initial state.

Figs. 1–3 show the behavior of the magnetic parameter *Hp* in the studied steels having different initial structural states: in a coarse-grain state — after annealing at 900°C, in a finer-grain (as-received) state, and with the deformed microstructure — after cold plastic deformation, depending on the number of heating/cooling cycles during thermal cycling.

The chemical composition of steels has a significant effect on the *Hp* parameter. The most noticeable changes in *Hp* are observed in 08ps steel, less significant changes — in 09G2S steel, and the least significant — in 10KhSND low-alloy steel. The initial structure of structural steels also affects the *Hp* magnetic parameter. For instance, after high-temperature annealing, all steels characterized by a coarse-grain structure — in contrast to steels characterized by a finer-grain structure (as-received state) — experience smaller changes in the *Hp* parameter, starting from the first cycle (Figs. 4, 5). Steels that have undergone preliminary cold plastic deformation (Fig. 6) are characterized by more noticeable changes in the magnetic parameter *Hp*, especially after the second and third cycles. It should be noted that regardless of the steel grade and the initial structural state, after the fifth cycle of thermal cycling, the difference between the maximum and minimum *Hp* values is no more than 4 A/m (Figs. 1–3), which indicates that the studied steels have approximately similar structural states after thermal cycling.

Figs. 7–9 show typical microstructures of 08ps, 09G2S and 10KhSND structural steels in different initial states after thermal cycling. It can be seen that, regardless of the initial structural state, a fine-grain structure is formed with a particular degree of dispersion in all steels after the first three heating/cooling cycles. An increase in the number of cycles to five promotes further grain refinement, however with a lower intensity, which correlates well with the magnetic measurements (Figs. 1–6). Similar results were obtained by Fedyukin and Smagorinsky (1989). Using C30, C40, and C60 carbon steels, they showed that five to six cycles are required to obtain the optimal structure and mechanical properties of steels during thermal cycling.

Grain refinement during the first heating/cooling cycle of thermal cycling is characterized by the following: it starts throughout the entire volume of metal simultaneously, however, in some areas, its intensity varies. This tendency persists until the third cycle, while steels show non-homogeneity in grain size. An increase in the number of heating/cooling cycles to five reduces non-homogeneity and increases the degree of dispersion, but with a lower intensity.

Such a tendency in the formation of a fine-grain structure during five cycles of thermal cycling and correlated changes in the magnetic properties make it possible to detect different stages of structural changes in structural steels and control the initial and subsequent stages of fine-grain structure formation.

The final structure of steels in thermal cycling depends on their chemical composition (Figs. 7–9). For instance, in the case of 08ps steel, grain size non-homogeneity decreases significantly after the second heating/cooling cycle, in the case of 09G2S steel, which contains silicon and manganese, it decreases after the third cycle, and in the case of

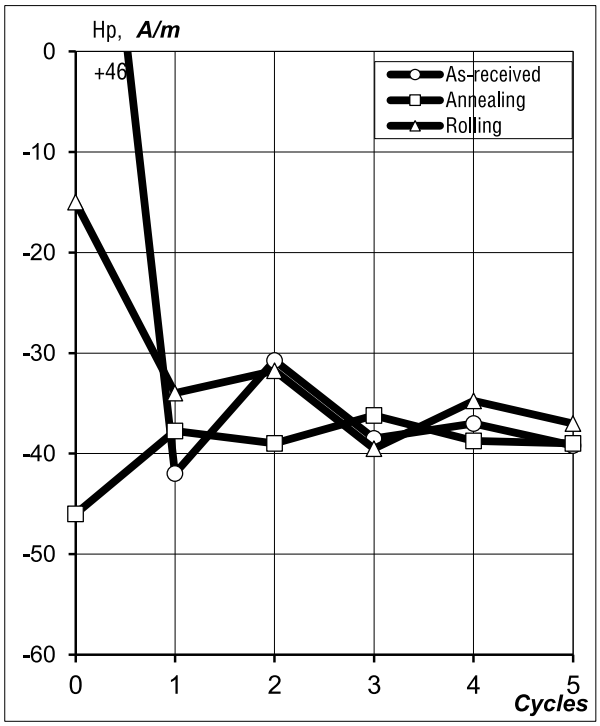

Figure 1. Effect of the number of heating/cooling cycles during thermal cycling on the magnetic parameter *Hp* of 08ps steel in different initial structural states

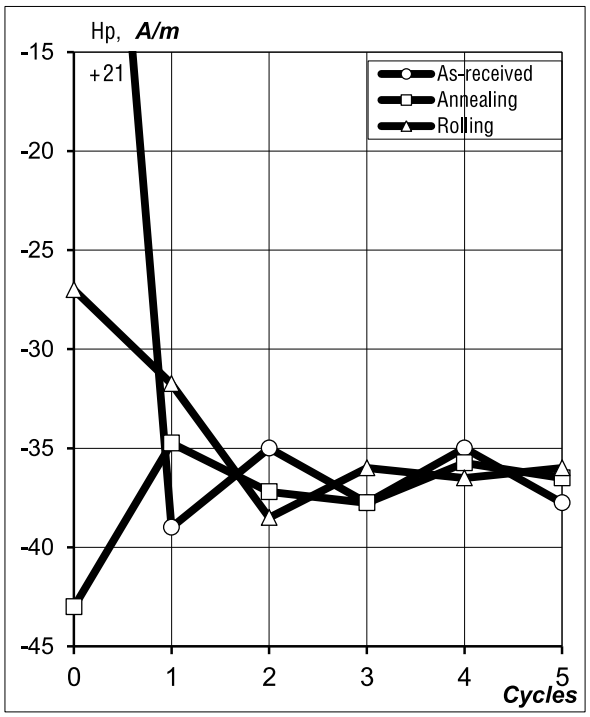

Figure 2. Effect of the number of heating/cooling cycles during thermal cycling on the magnetic parameter *Hp* of 09G2S steel in different initial structural states

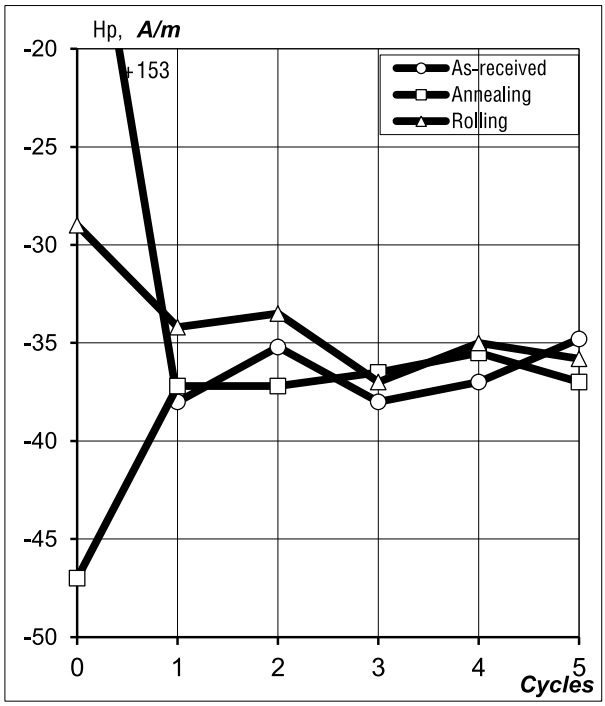

Figure 3. Effect of the number of heating/cooling cycles during thermal cycling on the magnetic parameter *Hp* of 10KhSND steel in different initial structural states

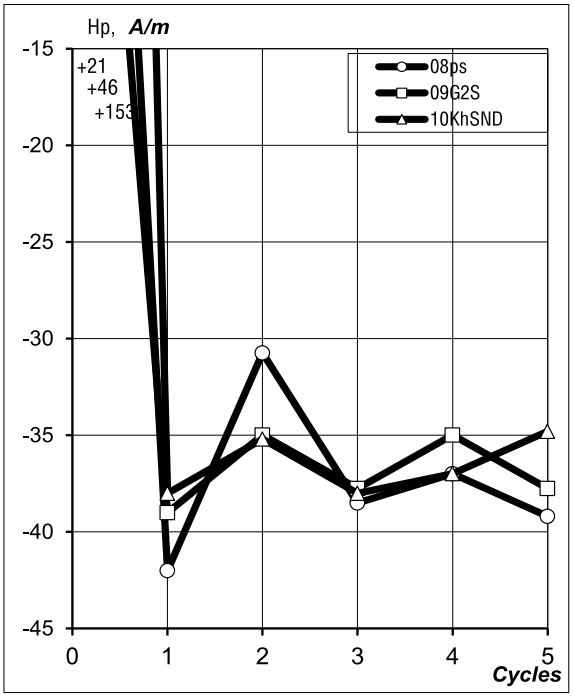

Figure 4. Effect of the number of heating/cooling cycles during thermal cycling on the magnetic parameter *Hp* of 08ps, 09G2S and 10KhSND steels in the as-received state

10KhSND steel containing an even greater amount of alloying elements — only after the fourth cycle. Such behavior during thermal cycling is probably due to the different amounts and mass fractions of alloying elements in steels. It should be noted that after the fifth cycle 10KhSND low-alloy steel has the smallest grain size in comparison with 08ps and 09G2S steels, presented initially in the same structural state.

The same pattern of change in the degree of dispersion of the initial structure in some areas compared with others was noted by Porter and

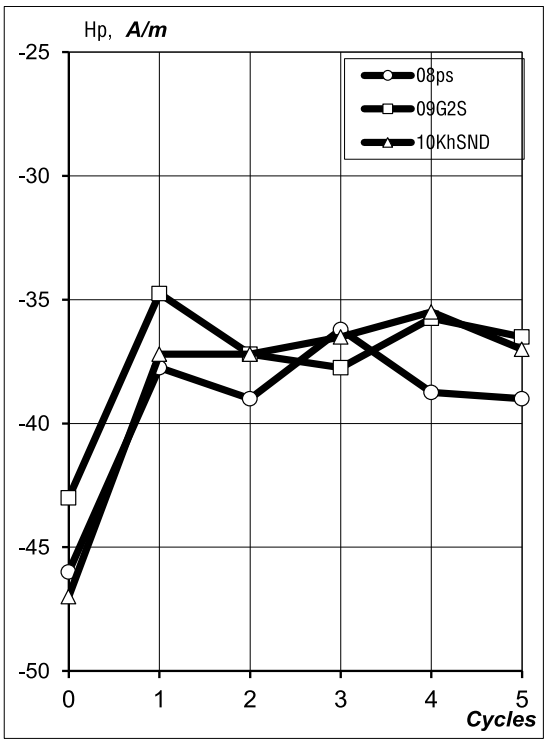

Figure 5. Effect of the number of heating/cooling cycles during thermal cycling on the magnetic parameter *Hp* of 08ps, 09G2S and 10KhSND steels in the state after annealing at 900°C

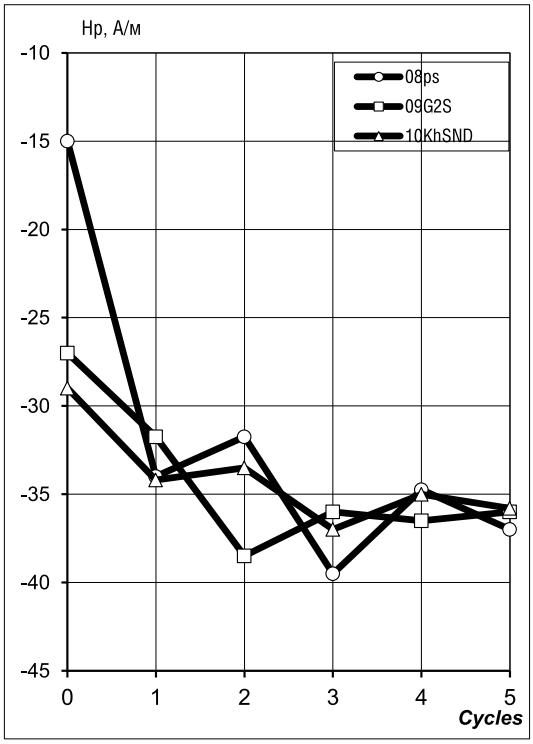

Figure 6. Effect of the number of heating/cooling cycles during thermal cycling on the magnetic parameter *Hp* of 08ps, 09G2S and 10KhSND steels in the state after deformation to ε = 50%

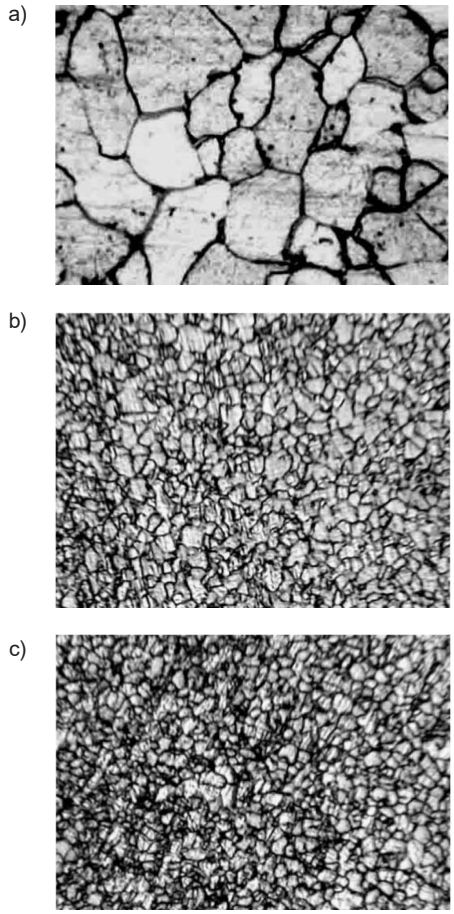

Figure 7. Changes in the structure of 08ps steel during thermal cycling, x650:
a — as-received, b, c — after the third and fifth heating/cooling cycles

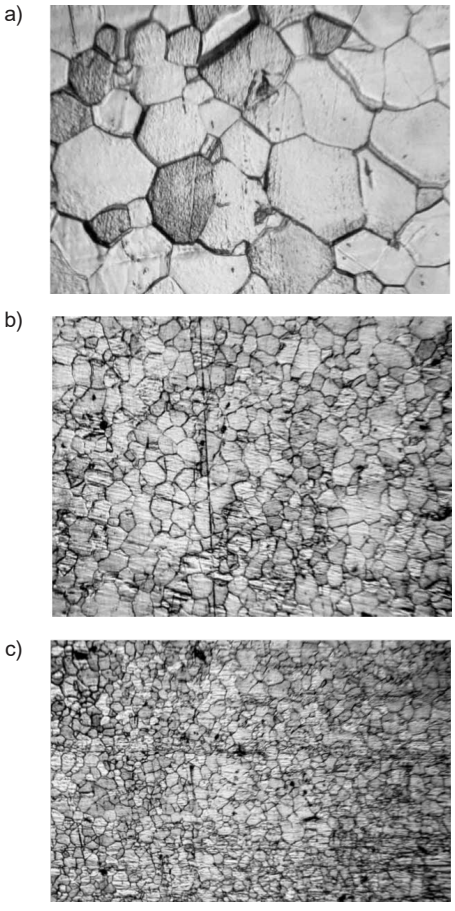

Figure 8. Changes in the structure of 09G2S steel during thermal cycling, x650:
a — as-received + annealing at 900°C,
b, c — after the third and fifth heating/cooling cycles

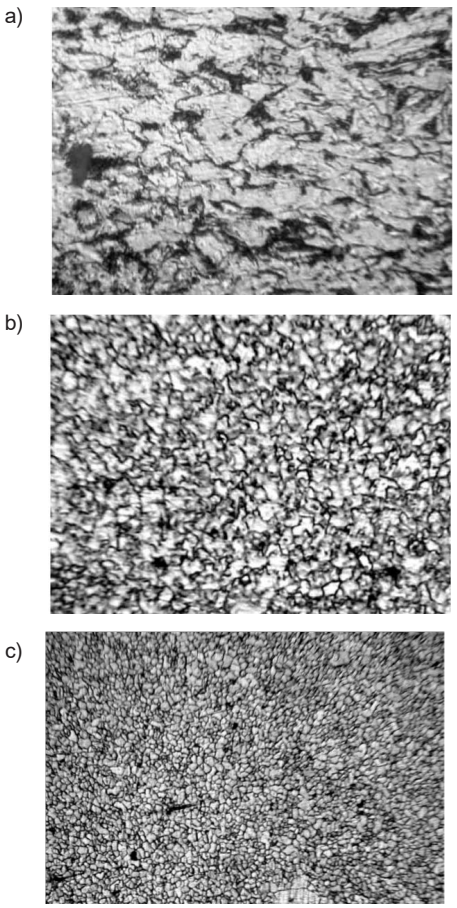

Figure 9. Changes in the structure of 10KhSND steel during thermal cycling, x650:
a — as-received + deformation to a degree of 50%, b, c — after the third and fifth heating/cooling cycles

Dabkowski (1973). A further increase in the number of heating/cooling cycles promoted structure refinement in all areas.

We should highlight that the presence of certain alloying elements in steels significantly reduces carbon mobility and activity, and this is the reason why changes in the structure of steels during cyclic heating and cooling occur more slowly. Thus, obtaining the final microstructure with the smallest possible grain size in alloy steels requires an increase in the number of cycles as compared with carbon steels. To accelerate structural transformations in steels with alloying elements during thermal cycling, the maximum heating temperature shall be increased by 50...70°C above the Ac_1 point. The initial microstructure of structural steels (coarse-grain, fine-grain, deformed) has a very significant effect on the formation of the final structure during multiple thermal cycling. In the case of a coarse-grain initial structure (after annealing at 900°C, Fig. 8) — in comparison with a finer-grain structure (as-received, Fig. 7) — a coarse-grain structure is formed after the third and fifth cycles of thermal cycling.

In the case of a deformed initial structure, the finest-grain structure is formed (Fig. 9) during thermal cycling as compared with other types of treatment. This is probably due to greater activation of structural transformations occurring during cyclic heating and subsequent cooling of steels. Significant structural changes in cold-deformed steels lead to changes in the *Hp* parameter during cyclic heating and cooling. Fig. 6 shows that the *Hp* values after the fourth and fifth cycles are almost equal, which indicates that intensive grain refinement is completed and an ultrafine-grain structure is formed.

Discussion

The developed modes of thermal cycling for structural steels in different initial structural states (as-received, after high-temperature annealing, after plastic deformation) with stage-by-stage control of structural transformations using passive magnetic flux leakage testing make it possible to obtain final fine-grain structures in steels.

Extra-strong structural steels having such a fine-grain structure can be used in critical components of metal structures and machine parts, exposed to high loads. Thermal cycling can be used to enhance the strength properties of metal in dangerous local stress concentration areas according to the results of diagnostics regarding the technical condition of constructions and machinery characterized by long-term operation.

Conclusion

1. We found the relationship between the magnetic parameter *Hp* and changes in the initial structure of 08ps, 09G2S and 10KhSND structural steels during thermal cycling. We also established that the *Hp* value depends on the degree of alloying, the initial structural state, and the number of heating/cooling cycles.

2. An increase in the number of cycles to three significantly increases the degree of refinement of the initial microstructure. An increase in the number of cycles to five reduces the grain size with a lower intensity but more significantly reduces grain size non-homogeneity.

3. With an increased amount of alloying elements, it is possible to form a finer-grain structure. Preliminary cold plastic deformation allows us to obtain the most dispersed microstructure.

4. The developed method of thermal cycling treatment for 08ps, 09G2S and 10KhSND structural steels makes it possible to obtain fine-grain structures with specified grain size (which enhances the strength properties of metal), which can be used to manufacture welded metal structures, bearing elements and operating parts of transport and special purpose vehicles as well as handling machinery. Thermal cycling with stage-by-stage magnetic control of structural transformations can be used to strengthen metal in dangerous local areas and closed contours in order to extend service life, improve reliability and operating safety, and reduce the risk of failures and accidents.

References

Belyaev, A., Gordienko, V., Druzhinin, P. and Evtukov, S. (2020). Mathematical model for selecting the best technology for restoring road construction machines. *E3S Web of Conferences*, Vol. 164, Article 03044. DOI: 10.1051/e3sconf/202016403044.

Fedyukin, V. K. and Smagorinsky, M. Ye. (1989). *Thermal cycling treatment of metals and vehicle components*. Leningrad: Mashinostroyeniye, Leningrad Department, 255 p.

Gordienko, V. (2020). Magnetic control of structural changes in structural steels during plastic deformation. *E3S Web of Conferences*, Vol. 164, Article 08023. DOI: 10.1051/e3sconf/202016408023.

Gordienko, V. and Bardyšev, O. (2013). Investigation of influence by the cold plastic deformation of metals on magnetic intensity of scattering. *World Applied Sciences Journal 23 (Problems of Architecture and Construction)*, pp. 74–79. DOI: 10.5829/idosi.wasj.2013.23.pac.90016.

Gordienko, V., Chernykh, A. and Repin, S. (2020). Influence of recrystallization annealing regime on the formation of a fine-grained structure in structural steels. *E3S Web of Conferences*, Vol. 164, Article 08021. DOI: 10.1051/e3sconf/202016408021.

Hetherington, M. G., Jakubovics, J. P., Szpunar, J. F. and Tanner, B. K. (1987). High-voltage Lorentz electron microscopy studies of domain structures and magnetization processes in pearlitic steels. *Philosophical Magazine B*, Vol. 56, Issue 5, pp. 561–577. DOI: 10.1080/13642818708220163.

Maslakova, T. M. (1978). Effect of thermal cycling (γ⇄α) on the properties of maraging steel. *Metal Science and Heat Treatment*, No. 20, pp. 991–995. DOI: 10.1007/BF00703274.

Porter, L. F. and Dabkowski, D. S. (1973). Grain-size control by thermal cycling. In: Gordienko, L. K. (ed.) *Ultra-fine grain metals*. Moscow: Metallurgiya, pp. 135–163.

Ranjan, R., Jiles, D. C. and Rastogi, P. K. (1987). Magnetic properties of decarburized steels: An investigation of the effects of grain size and carbon content. *IEEE Transactions on Magnetics*, Vol. 23, No. 3, pp. 1869–1876. DOI: 10.1109/TMAG.1987.1065175.

Rautioaho, R., Karjalainen, P. and Moilanen, M. (1987). Stress response of Barkhausen noise and coercive force in 9Ni steels. *Journal of Magnetism and Magnetic Materials*, Vol. 68, pp. 321–327. DOI: 10.1016/0304–8853(87)90008–4.

Savitsky, Ye. M. (1971a). Effect of thermal cycling on the fine structure and properties of molybdenum single crystals. In: Savitsky, Ye. M. (ed.) *Single crystals of refractory and rare metals*. Moscow: Nauka, pp. 119–124.

Savitsky, Ye. M. (1971b). Effects of thermal cycling on the single crystals of tungsten and molybdenum alloys. *Proceedings of the Academy of Sciences*, Vol. 198, No. 2, pp. 373–376.

Tanner, B. K., Szpunar, J. A., Willcock, S. N. M., Morgan, L. L. and Mundell, P. A. (1988). Magnetic and metallurgical properties of high-tensile steels. *Journal of Materials Science*, Vol. 23, pp. 4534–4540. DOI: 10.1007/BF00551956.

Thompson, S. M. and Tanner, B. K. (1993). The magnetic properties of pearlitic steels as a function of carbon content. *Journal of Magnetism and Magnetic Materials*, Vol. 123, Issue 3, pp. 283–298. DOI: 0.1016/0304–8853(93)90454-A.

СТРУКТУРНЫЕ ИЗМЕНЕНИЯ В КОНСТРУКЦИОННЫХ СТАЛЯХ ЭЛЕМЕНТОВ ТРАНСПОРТНО-ТЕХНОЛОГИЧЕСКИХ МАШИН ПРИ ТЕРМОЦИКЛИЧЕСКОЙ ОБРАБОТКЕ

Валерий Евгеньевич Гордиенко[1]*, Сергей Васильевич Репин[1], Александр Алфеевич Воробьев[2], Анжелика Анатольевна Абросимова[1]

[1]Санкт-Петербургский государственный архитектурно-строительный университет
2-ая Красноармейская ул., 4, Санкт-Петербург, Россия
[2]Петербургский государственный университет путей сообщения Императора Александра I
Московский пр., 9, Санкт-Петербург, Россия

*E-mail: val-gor@yandex.ru

Аннотация
В процессе экспериментальных исследований на конструкционных сталях, определяющих надежность металлоконструкций, например, таких транспортно-технологических машин, как грузоподъемные и транспортирующие, установлена корреляционная связь магнитного параметра *Hp* с характерным изменением микроструктуры при термоциклической обработке. Показано, что определяющее влияние на параметр *Hp* оказывает начальное структурное состояние стали, число и массовая доля легирующих элементов, число проведенных циклов нагрев–охлаждение при обработке. **Методы:** Установлено, что повышение количества циклов нагрев–охлаждение, количества легирующих элементов, а также проведение предварительной холодной пластической деформации при поэтапном контроле структуры сталей пассивным феррозондовым методом приводит к получению более мелкозернистой структуры в сталях, что было подтверждено методом металлографического анализа. **Результаты:** Рассмотрены некоторые особенности структурных изменений в сталях с разной начальной структурой при термоциклической обработке. Показано, что конечный размер зерен зависит как от числа циклов обработки, количества легирующих элементов, так и от начальной микроструктуры сталей. Именно мелкозернистая структура сталей обеспечивает повышение важнейших эксплуатационных характеристик: прочности, циклической прочности, хладноломкости.

Ключевые слова
Сварные металлические конструкции, конструкционные стали, транспортно-технологические машины, термоциклическая обработка, структурные изменения, мелкозернистая структура, металлографический анализ, пассивный феррозондовый метод контроля, магнитный параметр *Hp*.

Guide for Authors
for submitting a manuscript for publication in the «Architecture and Engineering»

The journal is an electronic media and accepts the manuscripts via the online submission. Please register on the website of the journal http://aej.spbgasu.ru/, log in and press “Submit article” button or send it via email aejeditorialoffice@gmail.com.

Please ensure that the submitted work has neither been previously published nor has been currently submitted for publication in another journal.

Main topics of the journal:

1. Architecture
2. Civil Engineering
3. Geotechnical Engineering and Engineering Geology
4. Urban Planning
5. Technique and Technology of Land Transport in Construction

Title page

The title page should include:

The title of the article in bold (max. 90 characters with spaces, only conventional abbreviations should be used); The name(s) of the author(s); Author’s(s’) affiliation(s); The name of the corresponding author.

Abstract and keywords

Please provide an abstract of 100 to 250 words. The abstract should not contain any undefined abbreviations or unspecified references. Use the IMRAD structure in the abstract (introduction, methods, results, discussion).

Please provide 4 to 6 keywords which can be used for indexing purposes. The keywords should be mentioned in order of relevance.

Main text

It should have the following structure:

1) Introduction,
2) Scope, Objectives and Methodology (with subparagraphs),
3) Results and Discussion (may also include subparagraphs, but should not repeat the previous section or numerical data already presented),
4) Conclusions,
5) Acknowledgements (the section is not obligatory, but should be included in case of participation of people, grants, funds, etc. in preparation of the article. The names of funding organizations should be written in full).

General comments on formatting:

- Subtitles should be printed in Bold,
- Use MathType for equations,
- Tables should be inserted in separate paragraphs. The consecutive number and title of the table should be placed before it in separate paragraphs. The references to the tables should be placed in parentheses (Table 1),
- Use “Top and Bottom” wrapping for figures. Figure captions should be placed in the main text after the image. Figures should be referred to as (Fig. 1) in the text.

References

The journal uses Harvard (author, date) style for references:
- The recent research (Kent and Park, 1990)...

- V. Zhukov (1999) stated that…

Reference list

The list of references should only include works that are cited in the text and that have been published or accepted for publication. Personal communications and unpublished works should only be mentioned in the text. Do not use footnotes or endnotes as a substitute for a proper reference list. All references must be listed in full at the end of the paper in alphabetical order, irrespective of where they are cited in the text. Reference made to sources published in languages other than English or Russian should contain English translation of the original title together with a note of the used language.

Peer Review Process

Articles submitted to the journal undergo a double blind peer-review procedure, which means that the reviewer is not informed about the identity of the author of the article, and the author is not given information about the reviewer.
On average, the review process takes from one to three months.